POLITECNICO
MILANO 1863

SCUOLA DI INGEGNERIA INDUSTRIALE
E DELL'INFORMAZIONE

Atmospheric box model simulation and assessment of the impact of increasing hydrogen concentrations.

TESI DI LAUREA MAGISTRALE IN
CHEMICAL ENGINEERING
INGEGNERIA CHIMICA

Author: **Silvio Abbate**

Student ID: 10658208
Advisor: Carlo Cavallotti
Co-advisor: Matteo Primi
Academic Year: 2024-25

Abstract

It is no exaggeration to state that combating climate change is the main challenge of the 21st century, and the efforts made by the scientific community over the past 60 years are a testament to the centrality of this issue. Over the years, numerous solutions have been proposed to mitigate climate change, particularly through the replacement of fossil fuels as energy sources. Among the many alternatives, hydrogen has gained considerable interest, leading to a large number of studies on its potential benefits in reducing greenhouse gas emissions, such as CO_2 and methane. However, hydrogen also presents several challenges, not only related to its large-scale use, but also concerning its effects on the atmosphere, thus requiring in-depth studies on its possible applications.

This thesis follows this path. In order to understand hydrogen's impact on the atmosphere, a detailed knowledge of atmospheric composition is essential. The study therefore begins with an analysis of atmospheric compounds and their reactions, using a box model described in detail, which examined the results of simulations involving increasing hydrogen concentrations in different environments, such as marine, urban, and stratospheric, evaluating the effects and estimating its GWP (Global Warming Potential).

The results were compared with those found in the literature, confirming that in nearly all environments, and especially in those that are significant in terms of mass, an increase in atmospheric hydrogen due to inevitable leaks during storage and transport leads to a non-negligible reduction in key molecules responsible for the removal of greenhouse gases. This confirms hydrogen's role as a co-greenhouse gas.

Key-words: Climate change, greenhouse effect, tropospheric simulations, stratospheric simulations, hydrogen economy, Global Warming Potential of hydrogen.

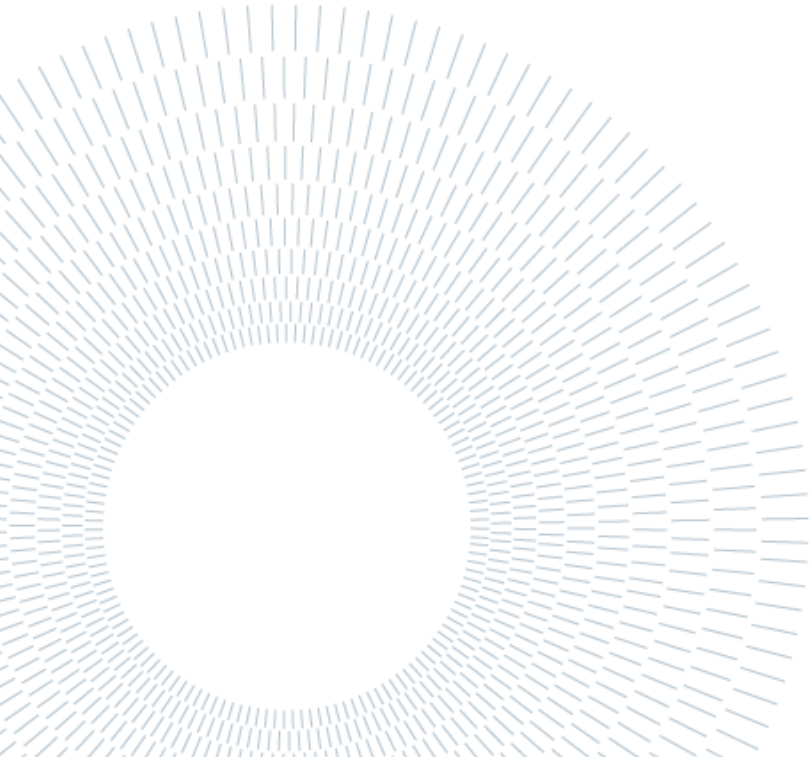

Abstract in italiano

Non è una esagerazione sostenere che il contrasto al cambiamento climatico sia la sfida principale del XXI secolo, e gli sforzi che la comunità scientifica ha impiegato in tal senso negli ultimi 60 anni sono una testimonianza della centralità del problema. Nel corso degli anni sono state proposte numerose soluzioni nella mitigazione del cambiamento climatico, specialmente nella sostituzione dei combustibili fossili come carburante. Tra le molte alternative anche l'idrogeno ha suscitato un discreto interesse, e perciò sono stati effettuati numerosi studi sui suoi possibili vantaggi nelle riduzioni delle emissioni di gas serra come la CO_2 e il metano. L'idrogeno, tuttavia, porta con sé numerose problematiche non solo legate al suo eventuale impiego su larga scala, ma anche ai suoi effetti in atmosfera, richiedendo perciò studi approfonditi sui suoi possibili impieghi.

Questa tesi si muove in tal senso. Per comprendere gli effetti dell'idrogeno sull'atmosfera, è necessario prima di tutto una dettagliata conoscenza della composizione della stessa.

Lo studio quindi si concentra in primo luogo sull'analisi dei composti presenti in atmosfera e delle loro reazioni tramite l'utilizzo di un box model descritto nel dettaglio, in seguito commenta i dati ottenuti simulando concentrazioni di idrogeno crescenti in ambienti diversi, quali quello marino, quello urbano e quello stratosferico, verificandone gli effetti e valutando il suo GWP (Global Warming Potential).

I risultati ottenuti sono stati confrontati con quelli proposti in letteratura, confermando che nella quasi totalità degli ambienti, e in tutti quelli rilevanti in termini di massa, l'incremento di idrogeno in atmosfera dovuto a perdite inevitabili in fase stoccaggio e nel trasporto di H_2 comporta una diminuzione non trascurabile di molecole in atmosfera fondamentali per l'eliminazione di gas serra, confermando il ruolo di idrogeno come co-gas serra.

Parole chiave: Cambiamento climatico, gas serra, simulazioni troposferiche, simulazioni stratosferiche, economia all'idrogeno, potenziale di riscaldamento globale dell'idrogeno.

Contents

Abstract ..... **i**

Abstract in italiano **3**

Contents ..... **v**

1 Introduction **1**

1.1. Atmospheric composition and reactivity at different altitudes 2

1.1.1. Greenhouse effect and greenhouse gases 2

1.1.2. Atmospheric structure and composition in marine and urban environments. 4

1.1.2.1. Tropospheric and stratospheric layer 4

1.1.2.2. Marine and urban environnement 6

1.1.3. Effect of the OH and HO_2 in atmosphere 7

1.2. Presence of hydrogen in the atmosphere and studies on its increase .. 11

1.2.1. Reactions of atmospheric hydrogen 12

1.2.2. Assessment of hydrogen accumulation in atmosphere. 13

1.2.3. GWP of the hydrogen 14

1.3. Conclusion, aim of the thesis and approach 17

2 Methodology **19**

2.1. Model description 19

2.1.1. GFDL kinetic mechanism 19

2.1.2. LMDz kinetic mechanism 21

2.1.3. Balancing of the reactions and notes. 21

2.1.4. Reaction with specific rate expressions 21

2.1.5. Additional Reactions 24

2.1.5.1. Added marine and extra reactions 26

2.1.5.2. Photochemical reactions 28

2.2. Operative conditions of the simulations 29

2.2.1. Initial conditions and constraints 30

2.3. Box Model 32

A Box Model Equations **37**

3 Results and discussions. 40
3.1. Tropospheric Marine environment 40
3.1.1 GFDL chemical scheme 41
3.1.1.1. Photochemical data from IUPAC 41
3.1.1.2. Photochemical data from MCM 44
3.1.1.3. Photochemical data from MCM and added reactions 47
3.1.1.4. Brute force analysis in marine environment with the GFDL mechanism. 50
3.1.1.5. Impact of H_2 increase on atmospheric reactivity 51
3.1.2. LMDz chemical scheme 53
3.1.2.1. Photochemical data from IUPAC 53
3.1.2.2. Photochemical data from MCM 56
3.1.2.3. Photochemical data from MCM with added reactions 59
3.1.2.4. Brute force analysis in marine environment with the LMDZ mechanism. 61
3.1.2.5. Impact of H_2 increase on atmospheric reactivity 62
3.2. Tropospheric Urban environment 64
3.2.1. GFDL chemical scheme 64
3.2.1.1. Photochemical data from IUPAC 65
3.2.1.2. Photochemical data from MCM 68
3.2.1.3. Photochemical data from MCM with added reactions 70
3.2.1.4. Simulation with different values of NOx with GFDL mechanism 72
3.2.1.5. Impact of H_2 increase on atmospheric reactivity 73
3.2.2. LMDz chemical scheme 74
3.2.2.1. Photochemical from IUPAC 75
3.2.2.2. Photochemical data from MCM 77
3.2.2.3. Photochemical data from MCM with added reactions 80
3.2.2.4. Simulation with different values of NOx with LMDz mechanism 82
3.2.2.5. Impact of H_2 increase on atmospheric reactivity 83
3.3. Stratospheric Environment 84
3.3.1. Stratospheric atmosphere at 15 Kilometres. 84

3.3.1.1. Impact of H_2 increase on atmospheric reactivity at 15 Km 87
3.3.2. Stratospheric atmosphere at 25 Km. 88
3.3.2.1. Impact of H_2 increase on atmospheric reactivity at 25 Km 90
3.3.3. Stratospheric atmosphere at 40 Km. 91
3.3.3.1. Impact of H_2 increase on atmospheric reactivity at 40 Km 94
4 Conclusions 97
Bibliography 99
B Equations for the evaluation of the SZA 103
List of Figures 107
List if Tables 113
List of symbols 115
Acknowledgments 119

1 Introduction

The detailed comprehension of the reactive chemistry that is active in the atmosphere is fundamental in order to contrast the climatic change and in its effects in both short and long periods.

The centrality of the problem clashes, however, with the difficulty of the simulation of complex systems such as the atmospheric one, which can account for more than a hundred components.

Each atmospheric species can have a specific influence on others, either by enhancing or suppressing their presence. This interplay becomes particularly significant when the species in question are directly or indirectly linked to human activities, such as carbon dioxide (CO_2) and methane (CH_4). Several of these gases have experienced a marked increase in atmospheric concentration over the past two centuries. For example, the CO_2 concentration in the pre-industrial era was approximately 280 ppm; due to anthropogenic emissions, this value has risen by about 50%, reaching approximately 430 ppm today (NASA, Carbon Dioxide, n.d.).

Some species can have a direct impact as greenhouse gases, while others exert an indirect influence by interacting with atmospheric components and altering the concentration of other greenhouse gases. A notable example is hydrogen, which, although not a greenhouse gas itself, can affect the atmospheric lifetime and levels of gases such as methane and ozone. This aspect should be carefully considered when planning to increase the use of hydrogen as an energy source.

Although the transition to hydrogen-based fuel from the traditional carbon one presents other major critical points, such as those related to hydrogen production and storage, the increase of this gas in the atmosphere due to an inevitable loss could partially offset the benefits of a carbon-free economy, due to hydrogen's indirect effects on the concentration of other greenhouse gases.

This chapter is organized as follows. It begins with an explanation of the greenhouse effect and the gases responsible for it, followed by a description of the atmospheric structure at different altitudes, along with a comparison of its characteristics in two different environments: marine and urban. The second part focuses on the role of hydrogen in the atmosphere and its related chemical reactions. An estimation based on the literature (Warwick & Griffiths, 2022) is then presented, evaluating the potential

increase of hydrogen in the atmosphere in a hydrogen-centred economy. Finally, the approach used to assess the Global Warming Potential (GWP) is outlined.

1.1. Atmospheric composition and reactivity at different altitudes

This paragraph illustrates the structure and composition of the atmosphere in which the simulations will be carried out. It also explains the theoretical background necessary to understand the motivations behind the entire thesis.

1.1.1. Greenhouse effect and greenhouse gases

The greenhouse effect is a phenomenon in which heat from the Sun is trapped within a planet's or satellite's atmosphere, leading to a warming of its surface. This effect is primarily caused by greenhouse gases. The main greenhouse gases in Earth's atmosphere include water vapor (H_2O), carbon dioxide (CO_2), methane (CH_4), nitrous oxide (N_2O), and ozone (O_3). As illustrated in figure 1.1.1.1, each gas can have a different impact on the planet's temperature, based on its chemical properties and its quantity.

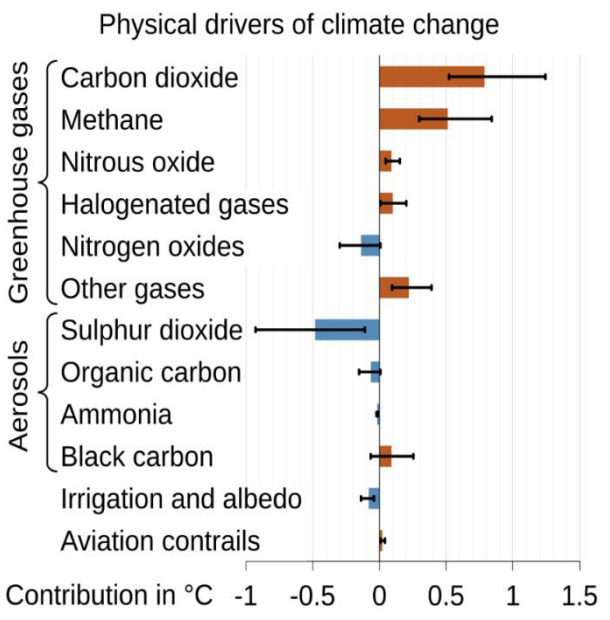

Figure 1.1.1.1: Impact of different molecules on the greenhouse effect. (IPCC, 2021)

All the greenhouse gases are infrared active, which means that they absorb and emit energy at the same wavelength of the earth. When this radiation reaches the molecules in the atmosphere, they scatter the energy in all directions; part of it returns to Earth's surface, further warming the planet.

This effect is fundamental for life on the earth, without it the temperature on the surface would decrease to -18°C (NASA, Earth observatory, n.d.).

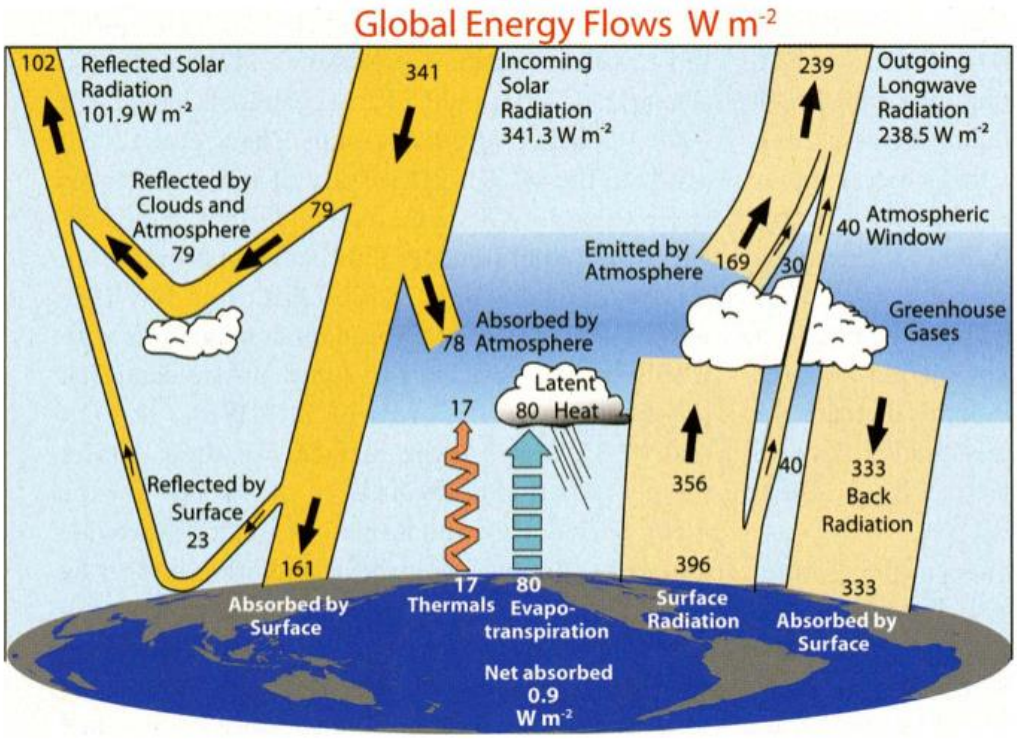

Figure 1.1.1.2: greenhouse effect with each effect displayed as Wm^{-2}. (TRENBERTH, FASULLO, & L, 2009)

1.1.2. Atmospheric structure and composition in marine and urban environments.

The simulations presented in this thesis are performed in two different sections of the atmosphere: the troposphere and the stratosphere, and in two different environments of the planet: the marine and the urban environment. Temperature and composition change drastically between the atmospheric layers and the environment, with a huge impact on the reactions that occur and their kinetic velocity.

1.1.2.1. Tropospheric and stratospheric layer

The first section considered is the tropospheric one, which is the lowest layer of the planet earth and the first in terms of mass of gases (more than 80%) and contains 99% of all the water in the atmosphere. Its thickness depends on the latitude: in the tropics reach 18 kilometres, 17 kilometres in the middle latitude and down to 6 in the polar regions; so, the average altitude of the troposphere reported and used is 15 kilometres (Reichle, 2023).

The main components of the troposphere are: N_2 (78.08%), O_2 (20.95%) and Argon (0.93%). The total amount of water depends by the location and the atmospheric conditions: is much more present in marine environment or in rainforest air, and is less present in the urban atmosphere.

The temperature can range from an average of 15°C on sea level, and down to -55°C at the tropopause (an atmospheric layer that separate troposphere and stratosphere) in which the temperature ceases to decrease and remain stable before increasing in the next section as shown in figure 1.1.2.2.

The second layer of the atmosphere is the stratosphere, which starts at around 15 kilometres and reaches an altitude of 50 kilometres. The temperature profile is the inverse of the troposphere: the temperature starts from -55°C and reach -15°C near the mesosphere. This profile is the results of the absorption of the UV light in the sunlight by the molecules.

The oxygen in the stratosphere can absorb the energy radiation from the sun in the UV-C region and generate two oxygen radical (Solomon, 1999):

$$O_2 + hv\ (< 240nm) \rightarrow\ O +\ O$$

The two radicals are in the ground level triplet state (O^3P) and with their two unpaired electrons are extremely reactive

$$O^3P + O_2 + M \rightarrow O_3 + M$$

M is the third body. Since the bond in the O_3 are much less energetic then the bonds in the O_2, the photodissociation can happen at a lower energy.

$$O_3 + hv\ (< 320\ \text{nm}) \rightarrow O_2 + O^1D$$

O^1D is an oxygen atom in an exited single state, stabilized by reaction with other molecules such as N_2 and O_2. This cycle creates a shield towards the high energy ultraviolet radiation that surpass the upper layers of the atmosphere

The ozone layer is not uniform at different altitudes: its concentration is higher in the middle and upper zone of the stratosphere (from 25 to 40 kilometres), in which the amount of oxygen is sufficiently high, and the solar radiation have enough energy to break it efficiently.

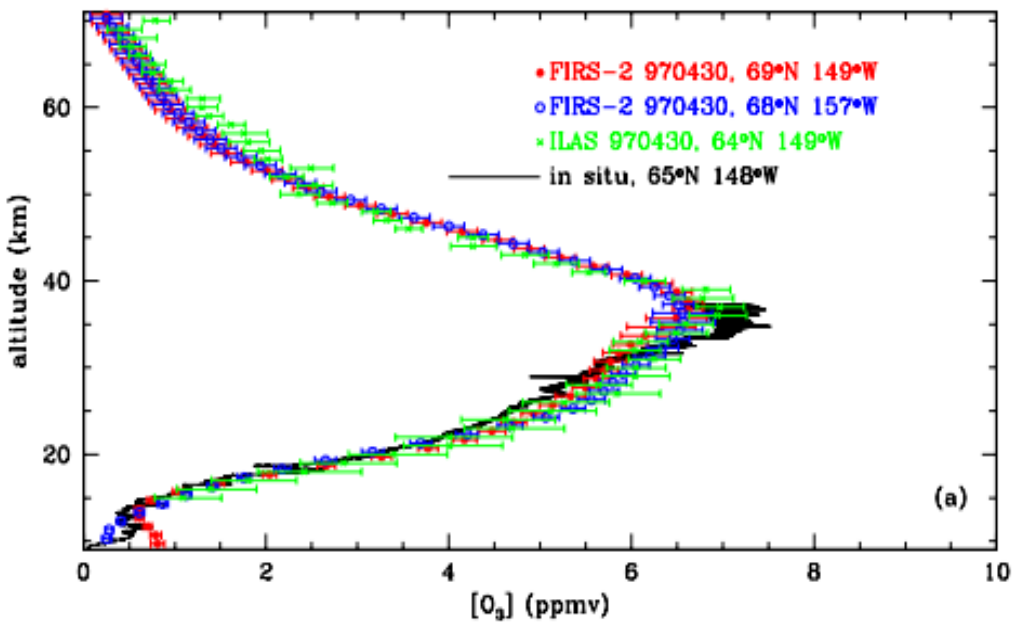

Figure 1.1.2.1: Ozone layer profile in the troposphere and the stratosphere (Jucks, Margitan, & Sasano, 1998)

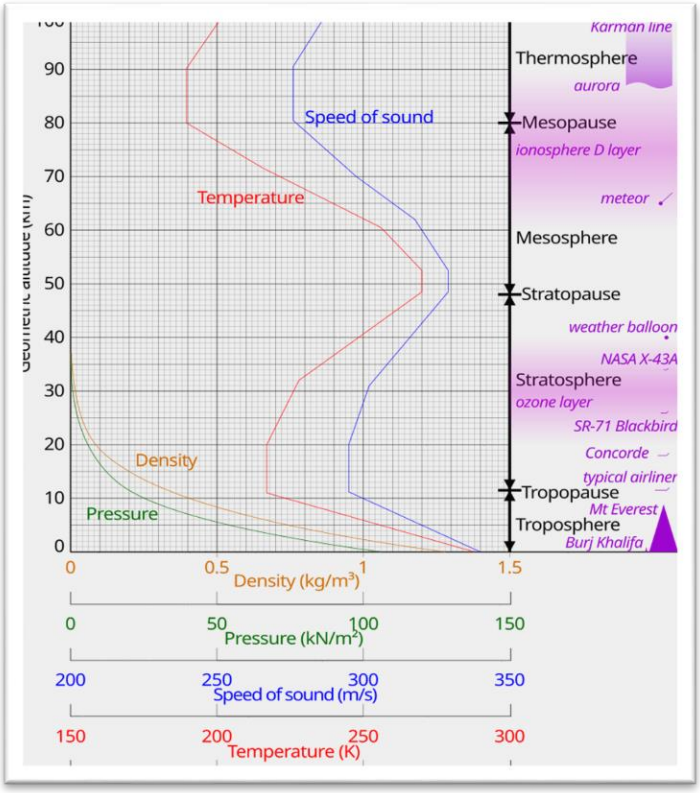

Figure 1.1.2.2: Temperature, pressure, speed of sound and density in different layers of the atmosphere (NASA, U.S. standard atmosphere , 1962)

1.1.2.2. Marine and urban environnement.

This research will analyse the impact of H_2 release in two different environments: marine and urban. The atmospheric composition differs significantly for some key molecules, and the water vapor content can vary with the seasons and geographical location. The higher concentration in the marine environment is due to exchange with the ocean surface. Chlorinated and brominated compounds are also more abundant in the marine atmosphere, due to the high levels of salt dissolved in seawater.

In the urban environment instead are much more present molecules produced by anthropogenic sources, as show in figure 1.1.2.3: Volatile organic compounds (VOCs) and tropospheric ozone are far more present, alongside CO and SOx. Most of these molecules are generated by reactions with the NOx; highly abundant in the urban atmosphere and generated by the transport sector, particularly road traffic and inland shipping. For example the tropospheric level of ozone is generated with the reactions displayed below: (Nguyen, Lin, & Vu, 2022):

$$NO_2 + hv\ (< 430\ nm) \rightarrow NO + O_2$$

$$O + O_2 + M \rightarrow O_3 + M$$

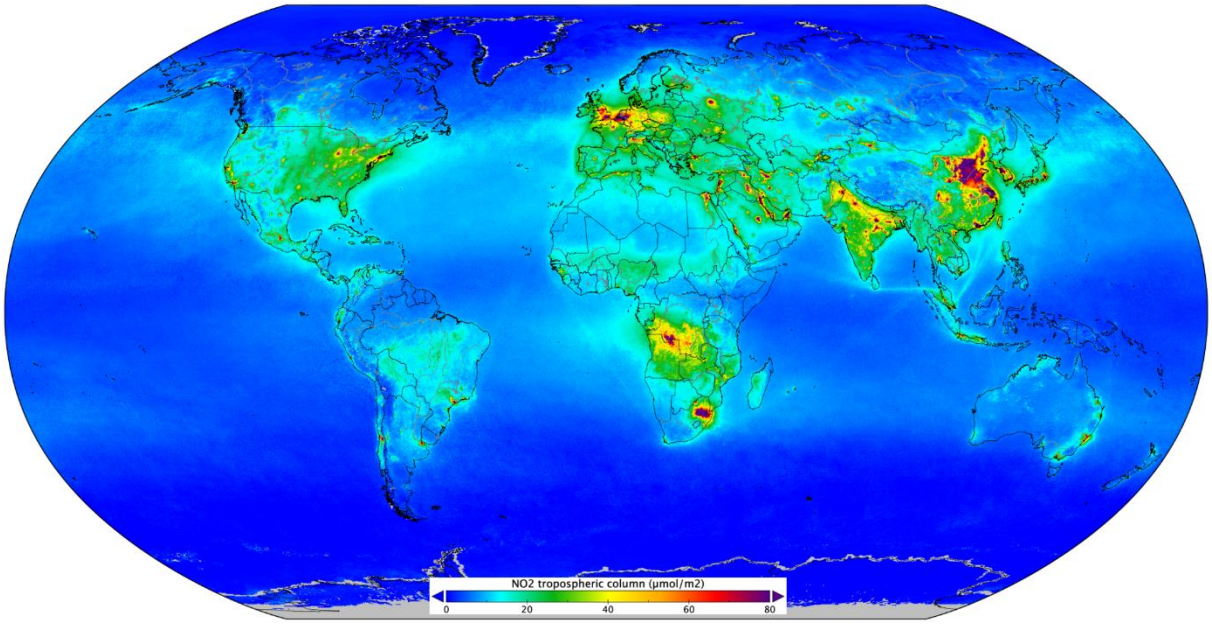

Figure 1.1.2.3: Nitrogen dioxide worldwide. Is easy to see that the NO_2 is high in concentration in the urban environment, and decrease in the see, especially in the artic and Antarctic regions (ESA, 2019)

1.1.3. Effect of the OH and HO_2 in atmosphere

OH is a strong oxidant in atmosphere that control the lifetime of some short-lived species, for example of methane (CH_4), which has a lifetime equal to 10 years and an impact equal to 27 to 30 GWP (Global Warming Potential) over 100 years (EPA, 2025).

The main source of OH in troposphere is by far the reaction between the O^1D and water in the reaction:

$$O^1D + H_2O \rightarrow 2OH$$

This is a second order reaction with a rate constant equal to:

$$1.62 * 10^{-10} * e^{\frac{0.54}{RT}} \frac{cm^3}{molecole * s}$$

The specie O^1D came from the photodissociation of O_3 with sunlight in the reaction:

$$O_3 + hv \rightarrow O_2 + O^1D$$

The reaction happens with a wavelength of $\lambda \leq$ 340 nm. The species O^1D is a high energy reactant that can easily break the water molecules in atmosphere and generate double the molecules of OH, which can break other molecules such as methane.

$$CH_4 + OH \rightarrow CH_3O_2 + H_2O$$

From the formation of CH_3O_2 there are various mechanism that ultimate lead to CO_2, with a GWP equal to 1. For example the methane cycle in the GFDL chemical scheme (Horowitz, Naik, & Paulot, 2020) continues as:

- Transformation of CH_3O_2 into CH_2O (formaldehyde)

$$CH_3O_2 + NO \rightarrow CH_2O + NO_2 + HO_2$$
$$CH_3O_2 + CH_3O_2 \rightarrow 2CH_2O + 2HO_2$$
$$CH_3O_2 + CH_3O_2 \rightarrow CH_2O + CH_3OH$$
$$CH_3O_2 + HO_2 \rightarrow CH_3OOH + O_2$$

- Transformation of CH_2O into CO

$$CH_2O + NO_3 \rightarrow CO + HO_2 + HNO_3$$
$$CH_2O + OH \rightarrow CO + HO_2 + H_2O$$

- Last, the CO became CO_2

$$CO + OH + M \rightarrow CO_2 + HO_2$$

The impact of OH (He, Naik, & Horowitz, 2021) is fundamental for the elimination of CH_4, that can remove up to 90 percent of it, as shown in table 1-1.

The major reactions that consume OH in atmosphere are the two reactions with CO and CH_4, that together remove up to 40-50 % of the total amount of OH in the marine environment.

GAS	Global emission rate (Tg $Year^{-1}$)	Removal by OH (%)
CO	2800	85
CH_4	530	90
C_2H_6	20	90
Isoprene	570	90
Terpenes	140	50
NO_2	150	50
SO_2	300	30
$(CH_3)_2S$	30	90

Table 1-1: Emission of greenhouse gases in a year and percentage removed by OH oxidation (Wang, Ming, & Li, 2022)

HO_2 plays a critical role as a radical in the atmosphere. The main source of the hydroperoxyl radical is the reaction of CO with OH:

$$CO + OH \rightarrow CO_2 + H$$

The radical of hydrogen that is produced from the rection is highly reactive, and react with one of the most present components in the atmosphere, the O_2:

$$H + O_2 + M \rightarrow HO_2 + M$$

Another important source of HO_2 is the reaction between H_2 and OH, discussed in more detail in the next paragraph.

$$H_2 + OH + O_2 \rightarrow H_2O + HO_2$$

HO_2 plays a critical role in the formation of H_2O_2, and most important in the removal of RO_2 (peroxyl radical) from the atmosphere, for example the CH_3O_2, and the destruction of ozone (O_3).

$$CH_3O_2 + HO_2 \rightarrow CH_3OOH + O_2$$

$$O_3 + HO_2 \rightarrow 2O_2 + OH$$

Knowing the cycles of OH e HO_2 displayed above is the key to a better understanding of the removal of greenhouse gases from the atmosphere. Those reactions are mainly relevant in the marine environment, which is the most important from a massive point of view, instead in the urban environment NO and NO_x are playing a much more critical role in the formation and destruction of the OH and HO_2, as showed in figure 1.1.3.1. The different impact of the NOx in the marine and urban environment is described in detailed in next paragraphs.

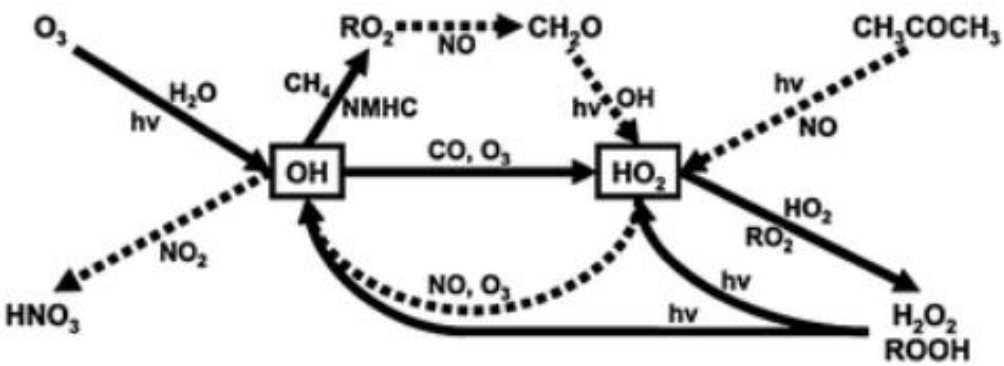

Figure 1.1.3.1: The image shows the HO_2 cycle in the atmosphere. The solid lines represent reactions relevant in the marine environment, where human pollution is low, while the dashed lines indicate reactions occurring at high NO_x levels, which are much more common in urban environments

1.2. Presence of hydrogen in the atmosphere and studies on its increase

In the context of climate change mitigation, several alternatives to traditional carbon-based fossil fuel have been proposed, among which molecular hydrogen has emerged as a promising candidate. The main reason is the total carbon removal from the combustion process: the only product of the reaction with air is the water and the NO_x as a byproduct from the atmospheric N_2.

The main drawbacks of the hydrogen as fuel lie in its production, storage and transportation (Sobrino, Monroy, & Pérez, 2010); The production of hydrogen is now mostly made by steam reforming for natural gas like methane, which creates CO_2 as byproduct. Another method is the electrolysis of water; however, this process entails a significant energy cost that cannot be overlooked. Hydrogen storage can be achieved through physical methods, such as compression or liquefaction in pressurized tanks, or via material-based approaches involving physisorption or chemisorption. However, storing a light and small molecule like H_2 leads to significant challenges, primarily due to its tendency to permeate through many materials, as show in figure 1.1.3.1. Reported hydrogen leakage rates vary considerably, ranging from 0.2% to as high as 20%, highlighting the uncertainty and complexity of reliable containment.

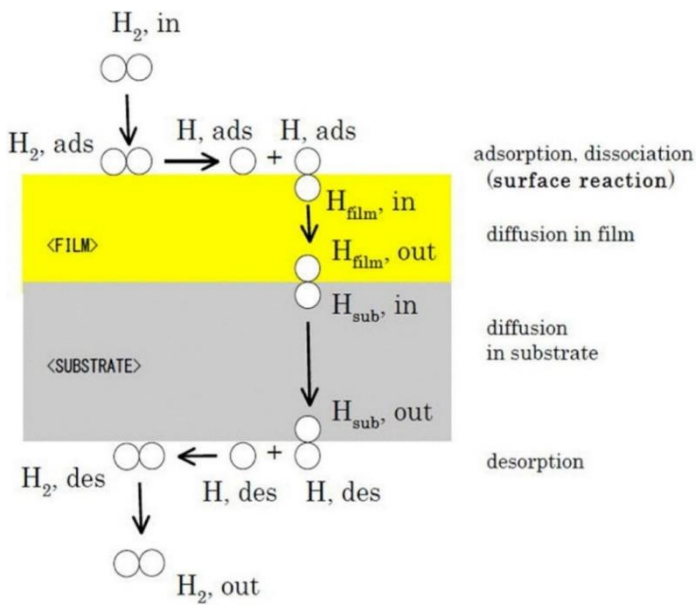

Figure 1.1.3.1: Hydrogen permeation in film and substrate mechanism (Meda, Bhat, & Pandey, 2023)

Any leakage of hydrogen can affect the atmospheric composition, react with its components and have an indirect effect as a greenhouse gas, as a warming agent and can partially neglect some of the benefits of the removal of fossil fuels.

1.2.1. Reactions of atmospheric hydrogen

H_2 is removed from the atmosphere primarily by soil uptake and from the reaction with OH, the main oxidant in atmosphere.

$$H_2 + OH + O_2 \rightarrow H_2O + HO_2$$

This reaction plays a significant role in the depletion of hydroxyl radicals (OH); at current atmospheric H_2 levels, it accounts for approximately 6% of OH removal. Its increment can lead to a reduction of OH in atmosphere, that implies a longer atmospheric lifetime for other compounds oxidized by OH, such as methane (CH_4).

$$CH_4 + OH \rightarrow CH_3 + H_2O$$

Tropospheric ozone (O_3) is another important greenhouse gas generated by a complex set of reactions involving NOx, VOCs, CO and CH_4. The controlling reaction is the one between the NO and the peroxide radicals.

$$NO + RO_2 \rightarrow NO_2 + RO$$

$$NO_2 + hv \rightarrow NO + O$$

$$O + O_2 + M \rightarrow O_3$$

HO_2 is the main RO_2, but also the one derived from carbon component (from C_1 to C_4) and VOCs can play a huge role in the ozone formation. In an environment rich in NOx, like the urban one, the O_3 level in troposphere is significantly higher. The elimination of ozone is also carried out by OH, and its reduction via H_2 can lead to an increase in tropospheric O_3.

Higher levels of H_2 can also increase the concentration of H_2O in atmosphere. The humidity level in the troposphere is controlled by the water that evaporate from the oceans, and hydrogen cannot significantly increase the total amount, but can affect the stratospheric amount of water, especially when emitted at high altitudes (from planes and other air transport).

1.2.2. Assessment of hydrogen accumulation in atmosphere.

The difficulty in predicting hydrogen storage losses also complicates the assessment of its potential accumulation in the atmosphere. From the actual level of hydrogen, which is 0.5 ppm, the increase can be estimated from a range of 50% (0.75 ppm) up to 300% (1.5 ppm); moreover, the amount of hydrogen absorbed by the soil remains very difficult to quantify, despite being the primary sink responsible for the removal of hydrogen from the troposphere.

With appropriate assumptions, it is possible to estimate the increase in atmospheric hydrogen resulting from a transition toward decarbonization. The first assumption is the percentage of leakage: more than 10% will be far too dangerous for safety reasons and too expensive, however, values that are too low would be overly optimistic, given the technical challenges associated with storage and transportation. Another important aspect is the H_2 currently emitted by the burning of fossil fuels, estimated around 20Tg per year, circa 20-25% of the global source of hydrogen.

The transition to a hydrogen-based economy is proposed sector by sector (Warwick & Griffiths, 2022), as illustrated in table 1-2; the different conversion percentages reflect the diverse availability of low-environmental-impact alternatives across different sectors.

	Final fossil fuel energy consumption (Million toe)	Percentage switch of final fossil fuel energy consumption to H_2 (%)	H_2 required to supply required energy consumption (Tg)	H_2 leakage at 1% (Tg yr^{-1})	H_2 leakage at 10% (Tg yr^{-1})
Buildings	1298	100	453	4.6	50.4
Transport	2768	50	284	2.9	31.5
Power	3500	10	122	1.2	13.6
Total	7566	40	859	8.7	95.5

Table 1-2: percentage of H_2 leaking in a global hydrogen economy (Warwick & Griffiths, 2022).

Knowing that 1 Ton of oil equivalent (toe) is 11630 KWh and 1Kg of H_2 is 33.3KWh, it is now possible to estimate the total amount of hydrogen needed for the proposed conversions, which corresponds to a 23% of the global energy consumption.

Under this assumption is now possible the estimation of the atmospheric level of H_2. The only remaining issue is the soil sink contribution for the depletion of hydrogen. Two scenarios are proposed: the first one where the soil sink is a constant flux and doesn't change with the H_2 fraction, and the second one with a constant deposition velocity and a flux than increase with the mixing ratio. The two scenarios lead to different final value of H_2, as illustrated in figure 1.2.2.1.

The H_2 concentrations used in the simulations range from a baseline value of 0.5 ppm up to 2 ppm, covering both scenarios and different percentage of leakage.

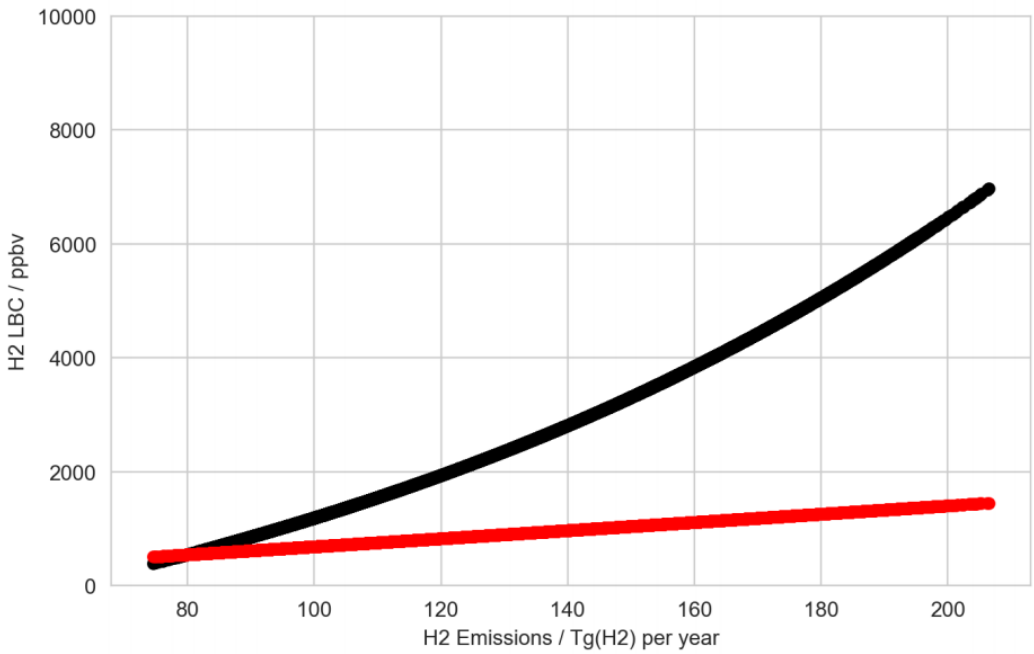

Figure 1.2.2.1: H_2 concentration in the atmosphere as a function of emissions: the black line corresponds to a fixed soil sink flux; the red one represents a flux that increases with the H_2 level (Warwick & Griffiths, 2022)

1.2.3. GWP of the hydrogen

The Global Warming Potential (GWP) is defined as the cumulative radiative forcing over a 100-year time horizon resulting from the emission of a given gas, relative to that of carbon dioxide (CO_2). The GWP of hydrogen is derived from three major contributions: the perturbation of methane (CH_4), the increase of the tropospheric ozone (O_3), and the increase of the stratospheric water.

Previous studies (Warwick et al. 2022) suggest a new method for the calculation of the GWP for gas with an intermediate lifetime like H_2, estimated as:

$$\frac{1}{\alpha_{H_2}} = \frac{1}{\tau_{H_{2+OH}}} + \frac{1}{\tau_{H_2SOIL}}$$

Is assumed that the lifetime in atmosphere depends on the soil uptake (difficult to evaluate) for about 75%, and the reaction with OH. Due to the uncertainties, the α_{H2} ranges from 1.4 to 2.2 years; the mid-range value is 1.9 years

The new equation for the evaluation of the GWP accounts for the radiative force generated by perturbation on the emission (AGWP1), the decay of the chemical perturbation (AGWP3), and the perturbation of the species that remain after the emission step (AGWP2).

$$AGWP1 = R\ a\ \alpha_R\ \alpha_H\ C \left(tp - \alpha_R \left(1 - e^{-\frac{tp}{\alpha_R}}\right)\right) - \left(\frac{\alpha_H}{\alpha_H - \alpha_R}\right)\left(\alpha_H\left(1 - e^{\left(-\frac{tp}{\alpha_H}\right)} - \alpha_M\left(1 - e^{\left(-\frac{tp}{\alpha_R}\right)}\right)\right)\right)$$

$$AGWP2 = \frac{R\ a\ \alpha_R\ \alpha_H^2\ C\left(1 - e^{\left(-\frac{tp}{\alpha_H}\right)}\right)}{\alpha_H - \alpha_R}\left(\alpha_H\left(e^{\left(-\frac{tp}{\alpha_H}\right)} - e^{\left(-\frac{H}{\alpha_H}\right)}\right) - \alpha_M\left(e^{\left(-\frac{tp}{\alpha_R}\right)} - e^{\left(-\frac{H}{\alpha_R}\right)}\right)\right)$$

$$AGWP3 = R\ a\ \alpha_R^2\ \alpha_H\ C\left(\left(1 - e^{-\frac{tp}{\alpha_R}}\right) - \left(\frac{\alpha_H}{\alpha_H - \alpha_R}\right)\left(e^{\left(-\frac{tp}{\alpha_H}\right)} - e^{\left(-\frac{tp}{\alpha_R}\right)}\right)\right)\left(e^{\left(-\frac{tp}{\alpha_R}\right)} - e^{\left(-\frac{H}{\alpha_R}\right)}\right)$$

AGWP = absolute global warming potential (W yr m^{-2} kg^{-1})

a = radiation rate of the species for indirect forcing per ppb H_2 change at steady state

R = radiating forcing scaling factor

α_R = lifetime of perturbation to species casing radiative forcing

α_H = H_2 lifetime

H = time horizon considered (100 years)

C = conversion factor from H_2 ppb into H_2 mass (kg)

tp = length of step emission (yr)

The a value is obtained by the following equation:

$$a = CH_4 * k(CH_4 + OH) * \frac{dOH}{dH_2}$$

The (Warwick & Griffiths, 2022) publication propose this set of values:

Value in UKESM1	
CH_4 LBC	1835 ppb
$k(CH_4+OH)$	2.8e-15 cm^3 molecule s^{-1}
dOH/dH_2	3.68e-9 (dimensionless)
A	1.46e-2 ppb(CH_4) yr^{-1} ppb(H_2)$^{-1}$

Table 1-3: values for the evaluation of a obtained by the literature (Warwick & Griffiths, 2022)

Based on the new equations proposed, the new GWP is derived:

$$GWP_{H2} = \frac{AGWP_{H2}}{AGWP_{CO2}}$$

The GWP obtained with this new approach than consider both the stratospheric and the tropospheric influence of H_2 is show in table 1-4, and its equal to 11 ± 5, a higher value respect to the previous data presented in the literature.

Radiatively active species	H_2 GWP(100) IPCC AR5	H_2 GWP(100) IPCC AR6	H_2 GWP(20) IPCC AR5	H_2, GWP(20) IPCC AR6
Methane	4.7	5.2	13.3	14.6
Tropospheric ozone (methane and non-methane induced)	3.2	2.7	9.6	8.4
Total Troposphere	**7.9**	**7.9**	**22.9**	**23.0**
Stratospheric water vapour (methane and non-methane induced)	3.0	2.9	9.6	9.2
Total	**10.9 (6.4 – 15.3)**	**10.8**	**32.6 (19.7 – 44.1)**	**32.2**

Table 1-4: GWP of H_2 of different contributions using both the data from IPCC AR5 and AR6 in 20 and 100 years (Warwick & Griffiths, 2022).

1.3. Conclusion, aim of the thesis and approach

The aim of the project is the simulation of atmospheric composition both in urban environment and in the marine one, and in the latter, we want to simulate the tropospheric and the stratospheric compositions, using two different types of models proposed by the literature: the GFDL model (Geophysical Fluid Dynamics Laboratory) and the LMDz model (Laboratoire de Metéorologié Dynamique, zoom). The different models considered in this work are selected from (Sand, Skeie, & Sandstad, 2023). Only two were chosen, based on their ability to describe both tropospheric and stratospheric environments (e.g., GFDL) and the inclusion of specific rate constant formulations (e.g., LMDz).

Once the atmospheric composition is determined, it becomes possible to evaluate the impact of each species. In particular, it is evaluated how bimolecular hydrogen can influence the concentration of other key compounds, such as hydroxyl radicals (OH) and hydroperoxyl radicals (HO_2), which play a crucial role in atmospheric chemistry and the lifetime of greenhouse gases.

The final step is the assessment of the effect of the H_2 on those two gases, the new level of methane in an atmosphere enriched with it, and the evaluation of the hydrogen GWP based on equation described in the literature.

2 Methodology

As previously mentioned, the aim of this project is to simulate atmospheric composition using two different models applied to two distinct atmospheric layers, with the final goal of evaluating the impact of hydrogen accumulation in the atmosphere.

The first section describes the structure and differences between the two models, the reaction balancing process, and includes notes on reactions with specific kinetic formulations, as well as the photochemical, marine, and other additional reactions included.

The second section outlines the operating conditions of the simulations, such as coordinates, temperature, and pressure, as well as the constraints applied.

Finally, the third section focuses on the box model, detailing its structure and the implementation of the Solar zenith angle evaluation.

2.1. Model description

The two models used for the atmospheric simulation are presented in the following paragraphs, including the reaction balancing process, details on the specific rate constants adopted (in comparison with those reported in the literature), and the additional reactions considered. All aerosol-phase reactions have been excluded from both models, as their contribution cannot be adequately represented in the current box model framework. The VOCs (Volatile Organic Compounds) contribution is also eliminated from the models.

2.1.1. GFDL kinetic mechanism

The Geophysical Fluid Dynamic Laboratory (GFDL) represent an Earth System Model (ESMs) that include aerosol (both natural and anthropogenic), cloud physics and precipitation. There are different versions of the chemical scheme, the most recent one is the AM4.1 (Atmospheric Model 4.1), that includes revision of atmospheric dynamics, physics, and chemistry interactions with land and ocean ecosystem.

AM4.1 provides multiple improvements over AM3 and AM4.0:

- A better understanding of the stratosphere
- Possibility to simulate interactive chemistry including ozone and methane
- Fidelity of aerosol over India, China and the Southern Ocean
- Representation of sudden warming stratospheric events.

With its higher resolution, as shown in the figure 2.1.1.1, the new version is much more computationally expensive than the previous generation of the GFDL.

The GFDL chemical scheme and the species are taken from (Horowitz, Naik, & Paulot, 2020), that describes all the rate constants of the model. Some reactions are removed from the scheme, such as the aerosol, the in-cloud reactions and the reactions in the heterogeneous phases.

From the standard chemical scheme, we introduced some other reaction that are illustrated in paragraph 2.1.5.

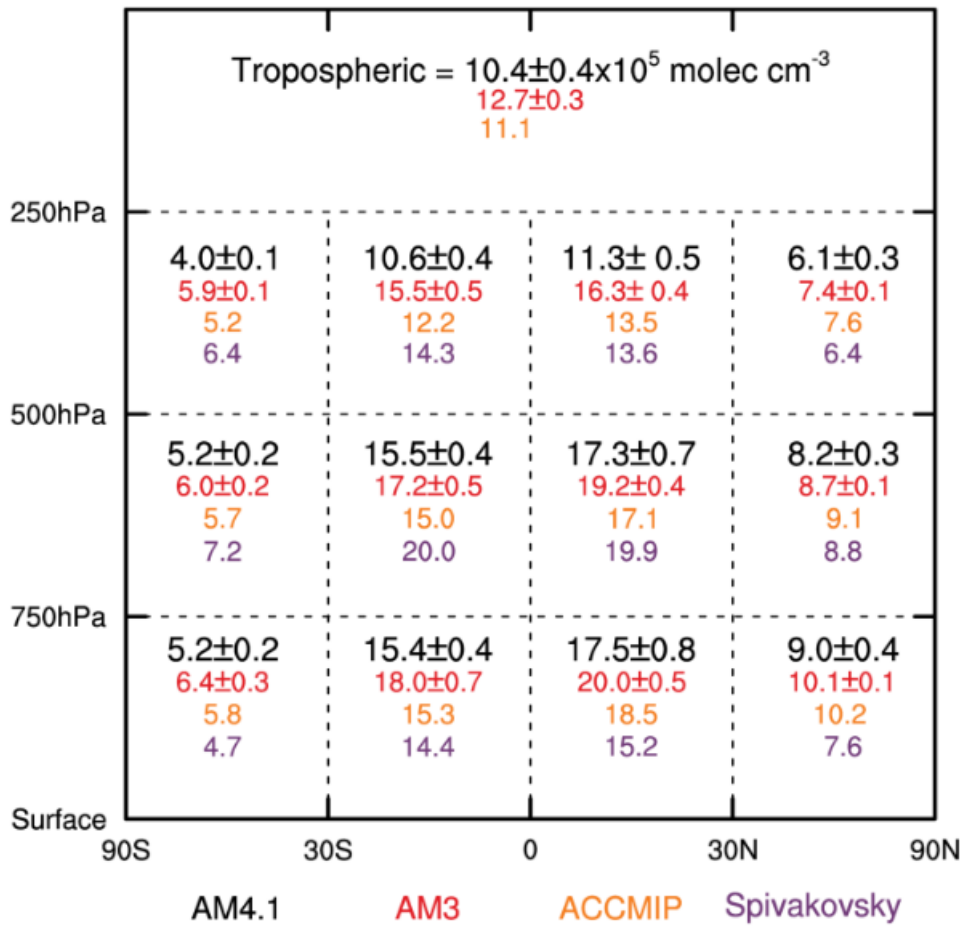

Figure 2.1.1.1: Climatological annual means tropospheric OH average globally and regionally compared with other chemical schemes (Horowitz, Naik, & Paulot, 2020).

2.1.2. LMDz kinetic mechanism

The LMDz (Laboratoire de Mètèorologie Dynamique, zoom) is a grid point general model (GCM) developed since the 1970s. The chemical scheme adopted is taken from (Folberth, Hauglustaine, Lathière, & Brocheton, 2006) which includes 83 species; the alkane species up to C3 (methane, ethane and propane) are treated especially, the species with 4 or more carbon atoms are lamped into artificial molecules. The alkenes follow the same methods. The isoprene oxidation pathway is represented in detail; only two alcohols are represented (methanol and all the C^{2}+ molecules are lumped together). The lamping is based on the reactivity with the OH. No bromine or chlorine species are considered.

2.1.3. Balancing of the reactions and notes.

The reactions included in the two kinetic schemes were not originally chemically balanced; however, our box model requires mass balance between reactants and products. The balancing process was performed by keeping the original reactants and products unchanged, while modifying or adding, if absent, only those species that are highly abundant in the atmosphere to avoid significant alterations to its overall composition. The species adjusted during the balancing process include O_2, H_2O, N_2, and, when necessary, CO_2. A simulation in which all reactions are balanced can improve the accuracy of atmospheric descriptions, especially when the target molecules are present in small quantities.

2.1.4. Reaction with specific rate expressions

The expression of the rate constant is not consistently structured across all reactions. Some reactions include specific formulations to better represent the pathways of certain molecules, while in certain equilibrium reactions, either the equilibrium constants (K_{eq}) or the reverse rate constants (k_{-1}) are reported instead. In all cases where the reaction rate is influenced by factors beyond temperature and M alone, the final value of the rate constant (K) is evaluated at the temperature and pressure specific to the environment, while other parameters (like water and O_2) are kept constant.

- $2HO_2 \rightarrow H_2O_2 + O_2$

  The rate constant of this reaction, in both the GFDL and the LMDz mechanism, is presented with a structure that include the concentration of water and the molecular density:

$$GFDL \qquad K = (K1 + K2 * [M]) * (1 + K3 * [H_2O])$$

$$LMDz \qquad K = (K0 + Ki) * fc \qquad fc = 1.0 + 1.4 * 10^{-21} * [H_2O] \exp\left(\frac{2200}{T}\right)$$

The contribution of water vapor has a significantly greater influence in the lower layers of the atmosphere. This effect is show in the figure 2.1.4.1. As suggested by (Zhang, Wang, & Wang, 2014), the formation of $H_2O\cdots HO_2$ and $HO_2\cdots H_2O$ complexes may involve hydrogen bonding, which reduces the negative charge on the oxygen atom in HO_2 and facilitates hydrogen abstraction.

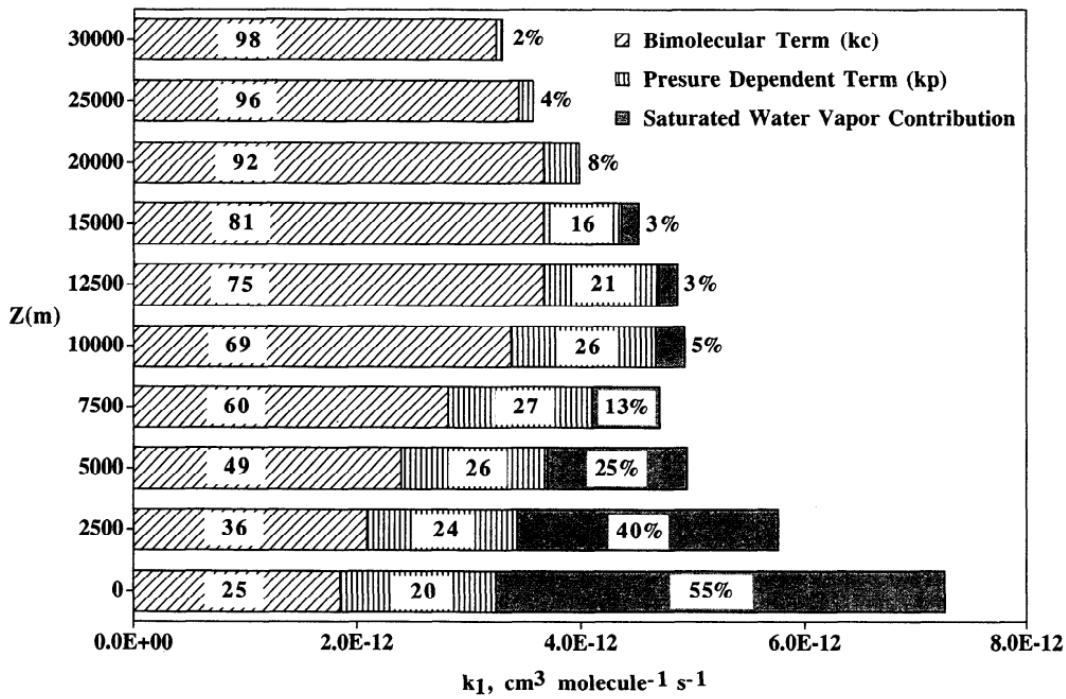

Figure 2.1.4.1: rate constant for the $2HO_2 \rightarrow H_2O_2 + O_2$. The water in the lower layers of the atmosphere impact for more than 50% (stockwell, 1995).

- $HNO_3 + OH \rightarrow NO_3 + H_2O$

  The rate constant both in GFDL and in LMDz includes a contribution to the reactivity of a third body [M]:

$$K = K1 + \frac{K3 * [M]}{1 + \frac{K3 * [M]}{K2}} \qquad GFDL$$

The influence of [M] though is minor since the rate constant depends almost completely on K1.

- $DMS + OH \rightarrow 0.75SO_2 + CH_2O$

  The DMS (dimethyl sulfide) reaction with OH is present only in the GFDL chemical scheme with a structure that includes [M] and [O_2]:

$$K = \frac{K1 * [O_2]}{1 + \frac{K2 * [O_2]}{[M]}}$$

  However, the reaction is presented alongside another identical one, which features a more straightforward rate constant expression that contributes more than twice as much; as a result, the influence of both O_2 and M is minor.

- $CO + OH \rightarrow CO_2 + H$

  The reaction between OH and CO is one of the major channels for the elimination of OH in the atmosphere. In the LMDz chemical scheme the expression of the rate constant is influenced by [M] (in the GFDL the reaction has a more straightforward rate constant expression).

$$K = 1.57 * 10^{-13} + 3.54 * 10^{-33} * [M]$$

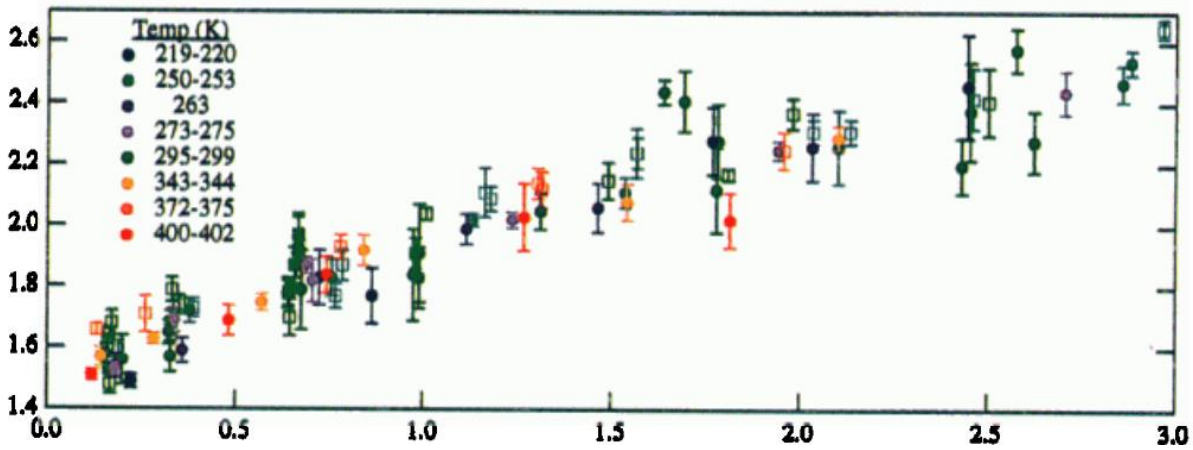

Figure 2.1.4.2: Plot of the rate constant K (in units of 10^{-13} cm^3 $molecule^{-1}$ s^{-1}) as a function of M (in units of 10^{-19} cm^{-3}) at different atmospheric temperatures (McCabe, TomaszGierczak, Talukdar, & Ravishank, 2001).

(McCabe, TomaszGierczak, Talukdar, & Ravishank, 2001) suggest this structure, in which the reaction occurs via two channels: the first one is pressure dependent and forms CO_2 and H, the second one is pressure dependent, and forms HCHO adduct. The two terms of the K represent those two different routes of formation with an uncertainty equal to 15%. The K value obtained in this method is higher than the one reported in the literature (and the one used in GFDL) by more than 60%, since they do not include the pressure dependent channel.

- Equilibrium reactions

  The kinetic schemes proposed by the two models also include equilibrium reactions (five in the case of GFDL and two for LMDz). All of these are termolecular reactions and are therefore characterized by both a low-pressure limit rate constant (K_0) and a high-pressure limit rate constant (Ki). The rate constants were obtained by calculating the equilibrium constant (Keq) and dividing the pre-exponential factors of the two K values by Keq, thus yielding a trimolecular expression in all cases.

2.1.5. Additional Reactions

In the two chemical models proposed above, some reactions are integrated to simulate different environments. These reactions fall into three different categories: marine, photochemical and the reactions of HCO, a species that can play a role in the elimination of important species such as CO, H_2, OH and CH_4.

All the rate constants of the bimolecular reactions are expressed as $cm^3/mol/s$:

$$K = A * T^n * \exp\left(-\frac{Eatt}{T * R}\right)$$

A is the pre-exponential factor, R is the gas constant equal to 1.987 Cal/K/mol. The rate constants of the trimolecular reactions are expressed in $cm^6/mol^2/s$:

$$k = \left(\frac{k0 * [M]}{1 + \frac{k0 * [M]}{ki}}\right) * f^{\frac{1}{a}}$$

$$a = 1 + \left(log_{10}\left(\frac{ko * [M]}{ki}\right)\right)^2$$

M is the gas concentration express in mol/cm^3. The photochemical reactions are used with two different sources for their values: the IUPAC (International Union of Pure and Applied Chemistry) and the MCM (master Chemical Mechanism). The photolysis rate is in s^{-1}:

$$J = l * \cos^m(X) * \exp\left(-n * sec(X)\right)$$

l is a pre-exponential factor that represent the value of J at noon, $\cos^m(X)$ represent the intensity of the solar energy and -n*sec(X) describe the amount of the solar energy that is absorbed by other molecules in atmosphere.

X represents the solar zenith angle, which is the angle between the Sun's rays and the vertical direction. The J value depends on the time of day, as it accounts for the day/night cycle; therefore, evaluating the solar zenith angle is essential for accurately simulating atmospheric conditions at any given moment. The set of equations used to calculate the solar zenith angle is provided in the Appendix

2.1.5.1. Added marine and extra reactions

The reactions specific for a marine environment are taken from (Whalley & Furneaux, 2010), the reactions considered are reported in the 2-1 and 2-2 tables.

Reaction	A	n	Eatt
$IO+HO_2=>HO_I+O_2$	8.43E+12	0.00	-1072.98
$I+HO_2=>HI+O_2$	9.03E+12	0.00	2165.83
$OH+HI=>I+H_2O$	1.81E+13	0.00	0.00
$IO+NO=>I+NO_2$	5.48E+12	0.00	-476.88
$I+O_3=>IO+O_2$	1.39E+13	0.00	1728.69
$HOI+OH=>IO+H_2O$	1.20E+11	0.00	0.00
$2IO=>I+OIO$	1.24E+13	0.00	-357.66
$2IO=>I_2O_2$	2.02E+13	0.00	-357.66
$I+NO_3=>IO+NO_2$	2.71E+14	0.00	0.00
$I_2+NO_3=I+IONO_2$	9.03E+11	0.00	0.00
$IO+OIO=>I_2O_3$	1.20E+14	0.00	0.00
$2OIO=>I_2O_4$	3.01E+13	0.00	0.00
$OIO+OH=>HOIO_2$	1.32E+14	0.00	-482.84
$OIO+NO=>NO_2+IO$	6.62E+11	0.00	-1076.95
$BrO+HO_2=>HOBr+O_2$	2.71E+12	0.00	-914.02
$Br+O_3=>BrO+O_2$	1.02E+13	0.00	1589.6
$Br+HCHO=>HBr+HCO$	4.64E+11	0.00	1152.46
$Br+CH_3CHO=>HBr+CH_3CO$	1.08E+12	0.00	914.02
$BrO+OH=>HO_2+Br$	1.02E+13	0.00	-496.75
$2BrO=>2Br+O_2$	1.45E+12	0.00	-79.48
$2BrO=>Br2+O_2$	1.69E+10	0.00	-1708.82
$BrO+NO=>NO_2+Br$	5.30E+12	0.00	-516.62
$HBr+OH=>H_2O+Br$	3.31E+12	0.00	-397.4
$BrO+IO=>Br+I+O_2$	4.52E+12	0.00	-516.62
$BrO+IO=>Br+OIO$	1.05E+13	0.00	-516.62
$BrO+O^3P=>Br+O_2$	1.14E+13	0.00	-457.01
$HOBr+O^3P=>OH+BrO$	7.23E+13	0.00	854.41
$BrONO_2+Br=>Br_2+NO_3$	2.95E+13	0.00	0.00
$BrONO_2+NO=>BrNO+NO_3$	1.81E+05	0.00	0.00
$BrONO_2+BrNO=>Br_2+2NO_2$	6.02E+07	0.00	0.00
$Br+NO_2(+M)=>BrNO_2(+M)$ Ki	1.08E+13	0.00	0.00
$Br+NO_2(+M)=>BrNO_2(+M)$ K0	1.34E+23	-2.40	0.00
$Br+NO_2(+M)=>BrNO_2(+M)$ f	0.4		
$Br+NO_2(+M)=>BrNO_2(+M)$ Ki	1.08E+13	0.00	0.00
$Br+NO_2(+M)=>BrNO_2(+M)$ K0	1.34E+23	-2.40	0.00

$Br+NO_2(+M)=>BrNO_2(+M)$ f	0.4		
$I+NO_2(+M)=>INO_2(+M)$ Ki	3.97E+13	0.00	0.00.
$I+NO_2(+M)=>INO_2(+M)$ K0	3.26E+19	-1.00	0.00
$I+NO_2(+M)=>INO_2(+M)$ f	0.6		
I+NO(+M)=>INO(+M) Ki	1.02E+13	0.00	0.00
I+NO(+M)=>INO(+M) K0	1.96E+18	-1.00	0.00
I+NO(+M)=>INO(+M) f	6.00E-01		
$IO+NO_2(+M)=>IONO_2(+M)$ Ki	9.64E+12	0.00	0.00
$IO+NO_2(+M)=>IONO_2(+M)$ K0	6.79E+29	-5.00	0.00
$IO+NO_2(+M)=>IONO_2(+M)$ f	4.00E-01		
$IONO_2=>IO+NO_2$	2.71E+19	0.00	23963.22
$BrONO_2=>BrO+NO_2$	6.89E+17	0.00	24559.32

Table 2-1: Marine reactions added to both GFDL and LMDz (Whalley & Furneaux, 2010)

Reaction	l	m	n
$BrO=>Br+O^3P$	3.80E-02	1.18E+00	2.43E-02
HOBr=>Br+OH	2.54E-03	8.09E-01	6.62E-02
$BrNO_2=>Br+NO_2$	5.39E-03	7.65E-01	7.08E-02
HOI=>OH+I	1.07E-02	7.48E-01	7.32E-02
$IO=>I+O^3P$	1.99E-01	6.38E-01	8.71E-02
$OIO=>I+O_2$	1.02E+00	3.67E-01	1.33E-01
$BrONO_2=>BrO+NO_2$	1.216E-04	8.197E-01	6.464E-02
$BrONO_2=>Br+NO_3$	1.502E-03	8.766E-01	5.838E-02

Table 2-2: Photochemical marine reactions added to both GFDL and LMDz (Whalley & Furneaux, 2010)

The extra reactions of HCO are taken by (NIST, 2025). All the selected reactions are reported in the 2-3 table.

Reaction	A	n	Eatt
$HCO+O^1D=>CO+OH$	3.01E+13	0.00	0.00
$HCO+O^1D=>CO_2+H$	3.01E+13	0.00	0.00
$HCO+H=>CO+H_2$	1.10E+14	0.00	0.00
$HCO+O_2=>CO+HO_2$	3.13E+12	0.00	0.00
$HCO+OH=>CO+H_2O$	1.02E+14	0.00	0.00
2HCO=>CHOCHO	3.01E+13	0.00	0.00
$2HCO=>2CO+H_2$	2.19E+13	0.00	0.00
2HCO=>HCHO+CO	2.70E+13	0.00	0.00
$HCO+CH_3=>CH_3CHO$	2.66E+13	0.00	0.00
$HCO+CH_3=>CH_4+CO$	2.65E+13	0.00	0.00

$HCO+C_2H_5=>C_2H_5CHO$	1.81E+13	0.00	0.00

Table 2-3: Added reactions for the simulation of HCO behavior in atmosphere

2.1.5.2. Photochemical reactions

The photochemical reactions presented in tables 2-4 and 2-5 include kinetic parameters from both the IUPAC (IPCC, 2021) and the MCM databased (MCM, s.d.). Are also reported the kinetic parameters for the O^1D formation taken by (Whalley & Furneaux, 2010).

In a photolytic reaction, one or more photons with sufficient energy break a molecule into multiple parts. The energy intensity of a photon is determined by its wavelength. The reaction rate can be calculated using the parameters listed in Tables 2-4 and 2-5, along with the SZA.

The detailed structure of the photolysis rate is reported in paragraph 2.1.5.

Reaction	l		m		n	
	MCM	IUPAC	MCM	IUPAC	MCM	IUPAC
$O_3=>O_2+O^3P$	4.78E-04	5.57E-04	2.98E-01	4.70E-01	8.00E-02	1.18E-01
$O_3=>O_2+O^1D$	6.07E-05	4.94E-05	1.74E+00	2.69E+00	4.74E-01	-8.19E-02
$NO_2=>NO+O^3P$	1.17E-02	1.18E-02	2.44E-01	8.17E-01	2.67E-01	6.38E-02
$BrONO_2=>Br+NO_3$	1.50E-03	1.50E-03	8.77E-01	8.77E-01	5.84E-02	5.84E-02
$BrONO_2=>BrO+NO_2$	1.22E-04	1.22E-04	8.20E-01	8.20E-01	6.46E-02	6.46E-02
$HCHO=>H+HCO$	4.64E-05	3.81E-05	7.62E-01	1.56E+00	3.53E-01	2.64E-03
$HCHO=>CO+H_2$	6.85E-05	5.11E-05	4.77E-01	1.25E+00	3.23E-01	1.77E-02
$HOCl=>OH+Cl$	3.03E-04	3.03E-04	1.13E+00	1.13E+00	2.95E-02	2.95E-02
$ClONO_2=>ClO+NO_2$	8.91E-06	8.91E-06	1.58E+00	1.58E+00	-9.72E-03	-9.72E-03
$ClONO_2=>Cl+NO_3$	4.57E-05	4.57E-05	1.07E+00	1.07E+00	3.59E-02	3.59E-02
$Cl_2O_2=>2ClO$	2.03E-04	2.03E-04	1.10E+00	1.10E+00	3.37E-02	3.37E-02
$Cl_2O_2=>Cl+OClO$	1.82E-03	1.82E-03	1.10E+00	1.10E+00	3.37E-02	3.37E-02
$N_2O_5=>NO_3+NO_2$	5.15E-05	5.15E-05	1.35E+00	1.35E+00	8.71E-03	8.71E-03
$HO_2NO_2=>HO_2+NO_2$	3.57E-06	3.57E-06	1.83E+00	1.83E+00	-1.31E-02	-1.31E-02
$HO_2NO_2=>OH+NO_3$	2.48E-06	2.48E-06	1.83E+00	1.83E+00	-1.29E-02	-1.29E-02
$H_2O_2=>2OH$	1.04E-05	7.82E-06	7.23E-01	1.47E+00	2.79E-01	-1.74E-04
$CH_3OOH=>CH_3O+OH$	7.65E-06	5.57E-06	6.82E-01	1.39E+00	2.79E-01	5.22E-03
$HONO_2=>OH+NO_2$	9.31E-07	6.78E-07	1.23E+00	1.99E+00	3.07E-01	-3.44E-02
$HONO_2=>HONO+O^3P$	1.89E-08	1.89E-08	1.99E+00	1.99E+00	-3.46E-02	-3.46E-02
$HONO_2=>HONO+O^1D$	2.10E-09	2.10E-09	1.99E+00	1.99E+00	-3.45E-02	-3.45E-02
$HONO_2=>H+NO_3$	6.99E-09	6.99E-09	1.99E+00	1.99E+00	-3.45E-02	-3.45E-02
$HONO=>NO+OH$	2.66E-03	1.82E-03	2.61E-01	9.34E-01	2.88E-01	4.85E-02

NO_3=>$NO+O_2$	2.49E-02	-	1.68E-01	-	1.08E-01	-
NO_3=>NO_2+O^3P	1.75E-01	-	1.55E-01	-	1.25E-01	-
CHOCHO=>$2CO+H_2$	6.85E-05	-	1.30E-01	-	2.01E-01	-
CHOCHO=>HCHO+CO	1.03E-05	-	1.30E-01	-	2.01E-01	-
CHOCHO=>2HCO	3.80E-05	-	6.44E-01	-	3.12E-01	-
mgly=>CH_3CO+HCO	1.54E-04	-	1.70E-01	-	2.08E-01	-
CH_3CHO=>CH_3+HCO	7.34E-06	-	1.20E+00	-	4.17E-01	-
C_2H_5CHO=>C_2H_5+HCO	2.88E-05	-	1.07E-01	-	3.58E-01	-
CH_3COCH_3=>CH_3CO+CH_3	7.99E-07	-	1.59E-01	-	2.71E-01	-
mek=>$CH_3CO+C_2H_5$	5.80E-06	-	1.09E+00	-	3.77E-01	-

Table 2-4: photochemical reactions added from IUPAC and MCM database

Reaction	l	m	n
O_3=>O_2+O^1D	5.48E-5	1.74E+00	4.74E-01

Table 2-5: kinetic parameter reported by (Whalley & Furneaux, 2010) for the photolysis of ozone

2.2. Operative conditions of the simulations

The values of temperature, pressure and density used during the simulations are obtained by (U.S. Standard Atmosphere, 1976) and are reported in table 2-6. The tropospheric simulation is performed at 1atm and 25°C, the stratospheric is performed at three different altitudes: 15km, 25 and 40km; the temperature and pressure used in these altitudes are also reported in table 2-6.

The marine simulations are performed on data 22 May near Capo Verde, coordinates: 17 for latitude and -25 for longitude. The urban simulations are performed on data 21 March in Mexico City, coordinates: -19.48872 for latitude and -99.14729 for longitude. These two locations were selected because detailed information on their atmospheric composition is already available in the literature; specifically, (Whalley & Furneaux, 2010) for Capo Verde and (Dusanter, Vimal, & Stevens, 2010) and (Sheehy, Volkamer, Molina, & Molina, 2010) for Mexico City.

Height (Km)	Pressure (hPa)	Temperature (K)	Density (g m^{-3})	H_2O Moist (g m^{-3})	H_2O Dry (g m^{-3})	M (molecule cm^{-3})
0	$1.013*10^3$	288	$1.225*10^3$	5.9	5.9	$2.46*10^{19}$
15	$1.221*10^2$	217	$1.948*10^2$	$7.2*10^{-4}$	$7.2*10^{-4}$	$3.99*10^{18}$
25	$2.549*10^1$	222	$4.008*10^1$	$6.1*10^{-4}$	$5.0*10^5$	$8.21*10^{17}$
40	2.871	253	3.996	$4.8*10^{-5}$	$7.9*10^{-6}$	$8.11*10^{16}$

Table 2-6: Operative conditions at different altitudes (U.S. Standard Atmosphere, 1976)

2.2.1. Initial conditions and constraints.

Initial conditions and constraints are applied in order to perform the simulation and are reported in tables 2-6 and 2-7. The initial conditions change with the location and the altitude of the simulation; for the marine tropospheric atmosphere the data are taken from (Whalley & Furneaux, 2010), the initial conditions for the urban troposphere are taken from (Dusanter, Vimal, & Stevens, 2010), and for the stratosphere the data are taken from climatological simulation from the Eschimo (Earth System Chemistry integrated Modelling) system. The O_2 and N_2 are around 0.2089 and 0.784 and are adjust to make the sum of all the species equal to 1.

The constrains maintain fixed the concentrations of the species to better perform the simulations. The species constrained are chosen with theoretical hypothesis and trial and error procedure.

Specie	Marine		Urban	
	ppb	fixed	ppb	Fixed
O_3	35	YES	56.2	YES
NO	0.0023	YES	16.4	YES
NO_2	0.011	YES	28.4	YES
H_2	500	NO	679	YES
H_2O	$2.38*10^7$	YES	$6.60*10^6$	YES
BrO	0.0029	NO	0.0029	NO

HONO	-	NO	0.43	YES
CH_4	1821	YES	2300	YES
C_2H_6	0.845	YES	6.2	YES
C_3H_8	0.05	YES	7.81	YES
ISOP	0.01	YES	0.32	YES
CO_2	390000	NO	390000	YES
CO	104	YES	765	YES
DMS	-	NO	0.396	YES
C_2H_5CHO	-	NO	0.5	YES
HCHO	0.328	YES	0.328	YES
CH_3COCH_3	0.487	YES	10.2	YES
CH_3CHO	0.826	YES	2.25	YES
CH_3OH	0.749	YES	7.81	YES
$C_{10}H_{16}$	-	NO	0.14	YES
SO_2	-	NO	3.4	YES
C_2H_4	-	NO	6.9	NO
C_2H_5OH	-	NO	7.81	NO
C_3H_6	-	NO	2.76	NO
C_4H_{10}	-	NO	7.81	NO
CHOCHO	-	NO	0.42	YES
C_3H_7OH	-	NO	0.445	NO
IO	0.0013	YES	-	NO
BrO	-	YES	-	

Table 2-7 : initial conditions in the tropospheric environment

Specie	Stratosphere			
	15 Km (ppb)	25 Km (ppb)	40 Km (ppb)	fixed
O^3P	0	0.0095	7	NO
O_3	77.4	5700	5690	YES
NO	0.204	0.377	7.72	YES
NO_2	0.198	1.1	8.19	YES
NO_3	0	0.004	0.115	NO
N_2O	313	254	46.5	NO
N_2O_5	0.0023	0.285	0.514	NO
H_2	554	572	538	NO
OH	0.0005	0.0015	0.123	NO
H_2O	4900	3830	5460	YES
HO_2	0.0021	0.0112	0.0823	NO
H_2O_2	0.166	0.603	0.0451	NO
Cl	0	0	0.0024	NO
ClO	0	0.0479	0.263	NO
HCl	0.0121	1.02	2.5	NO

HO_2NO_2	0.0077	0.131	0.0071	NO
HOCl	0	0.0386	0.0886	NO
$HONO_2$	0.0931	2.75	0.164	NO
OClO	0	0.0008	0.0085	NO
CH_4	1720	1470	771	YES
CO_2	363703	363703	363703	NO
CO	82	15.5	57.2	YES
HCHO	0.0536	0.0039	0.209	YES
CH_3OH	0.834	0.0002	0.0001	YES
CH_3O_2	0.0002	0.0004	0.0042	NO
CH_3OOH	0.0378	0.006	0.0035	NO
NH_3	0.0172	0.0041	0	YES

Table 2-8: Initial concentrations in stratospheric environment

2.3. Box Model

A box model for the atmospheric simulation represents the air as a simple box that contains perfectly mixed air with all the species chosen from a chemical model at a given temperature and pressure, where all the reactions occur simultaneously. The box model approach assumes that all molecules are perfectly mixed in a volume. Critical aspects for the use of the box model include the selection of the time period and the dimensions of the air box.

The code used for the box model simulation is written in Fortran, a programming language particularly well suited for numerical computations in engineering, due to its robustness and efficiency.

In our box model the material balances are written on mass basis and the equation in dimensionless form. Three different kinds of species are considered:

1. Gas phase species
2. Adsorbed species
3. Solid species

The air box is represented as a reactor with in and out fluxes.

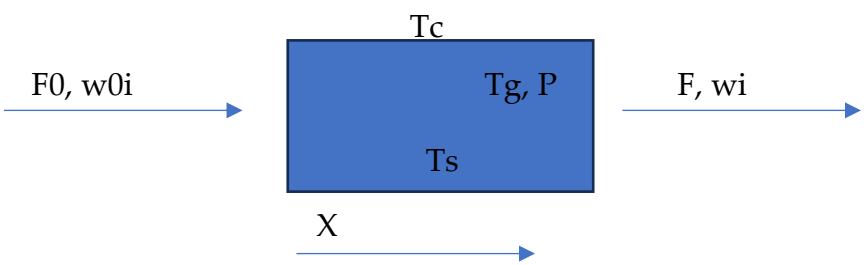

Figure 2.2.1.1: air box represented as a reactor

For the solid and adsorbed species, the gas phase concentrations are assumed equal to zero, the same goes for the surface gas phase concentration. The system can simulate up to three types of surface sites, and the free surface is considered as an absorbed species.

The unknowns of the system are:

- wi; the unknowns are equal to the gas species
- wi,s; the unknowns are equal to the adsorbed species
- th1i; the unknowns are equal to the species adsorbed on the first type sites
- th2i; the unknowns are equal to the species adsorbed on the second type sites
- th3i; the unknowns are equal to the species adsorbed on the third type sites
- X ; a single unknown
- Tg; a single unknown

The total amount of the unknowns is: 2NCG + Nsite x NCA +2.

The corresponding equations for the solution of the system are (the detailed equations are reported in the Appendix):

- Material balance; NCG – 1 equations.
- Gas phase stoichiometric equation; 1 equation.
- Flux balance; NCG – 1 equations.
- Surface stoichiometric equation; 1 equation.
- Overall gas phase material balance; 1 equation.
- Surface material balance; Nsite * NCA – Nsite.
- Nsite surface equations; Nsite.
- Overall energy balance; 1 equation.

The set of equations, given by NCG – 1 + 1 + NCG – 1 + 1 + 1 + Nsite x NCA – Nsite + Nsite + 1, results in a total of 2NCG + Nsite x NCA + 2 equations, which are sufficient to fully define the mathematical problem. In our, only species in the gas phase are presented.

The solver used for this problem is the DASPK (Differential-Algebraic equations Solver with Preconditioned Krylov methods); it is often used for the resolution of stiff and large problem like the description of the atmosphere composition in time.

The box model requires the following 8 input data files.

1. dtrea.dat; in the file are reported the reactor parameters and the operating conditions, like the pressure and temperature, the dimensions of the reactor that represent the atmospheric box and other values.

2. Kinet.dat; contains the kinetic data of the system, including the rate constants (but not the stoichiometric matrices). The file starts with the total number of gas species, the number of the adsorbed one and the number of solid one, followed

by the list of all of them. With the species are reported the initial conditions of them, if it is necessary, and the 'Y' if the species are considered in the simulation. Below are reported the chemical reactions, identified with G or P (if the reaction is photochemical) followed by the reaction number; the kinetic parameters for the evaluation of the rate and 'T' or 'B' (for trimolecular or bimolecular reactions) and 'F' or 'R' (for only forward or reversible).
The kinet.dat file is generated by two other files called chemkin_gas.dat and chemkin_photo.dat.

3. Stech.dat; that contains the gas matrix, both for the gas phase and the surface reactions.

4. Order.dat; the reaction order coefficients both for the gas phase and the surface reactions are contained here (not necessary for elementary reactions). Here are reported all the coefficients that are different from the one indicated in the reactions in chemkin_gas.dat

5. Chphy.dat; that contains the thermodynamic and the chemical-physical properties (like molecular weight, standard enthalpy, capacity). The heat capacity has the equation: $Cp = a + b*T + c*T^2 + d/T^2 + e*T^3 + f*T^4$.

6. Trnsp.dat; the transport properties are reported here. The reference standard temperature (300 K) and pressure (1 atm) are used to evaluate the transport properties.

7. Dassl.dat; the file contains different initialization parameters, like the relative and absolute tolerance (RETOL, ABSTOL); the tolerance, max iterations and relaxation parameter for the Newton method (TOLNEW, ITMAXN, RELNEW); IDST and INVIDEO select the amount of data that is shown and stored in other files (like iter.tst and jacm.tst) and other to select the integration step and the possibility to use negative variables.

8. Incmp.dat; the last input data contains the initial guess values for starting the numerical solving procedure. It is not necessary to give all of the first guesses; an automatic generation of the first attempt model is provided.

Accurate simulations of photochemical reactions necessitates the evaluation of the Solar Zenith Angle (SZA), defined as the angle between the sun's rays and the vertical direction. Given that the SZA varies with temporal parameters such as year, month, day, and hour, its characterization demands a comprehensive set of input informations, such as:

- Year, day and hour of the simulation given from the operator.
- The evaluation of the day and the century in the Julian calendar.
- The main obliquity ecliptic (the axial tilt) and the obliquity correction (gradual change of the axis tilt)
- The mean anomaly of the sun, its longitude and the position of its centre.
- The orbit of the earth and the true solar time

With all the aforementioned information, it is possible to achieve an accurate determination of the Solar Zenith Angle (SZA)

Once the simulation is completed, the software produces three main output files: res0.res, that contains all the results of the calculation; res1.res, with a short cut writing of the calculation (x, Ts, Tg, Tc thermal fluxes, dimensionless flow rate, growth rate and solid composition); res2.res contain a short cut writing of the dimensionless numbers (x, Re_x, Re_H, Pr, Sc, Gr, Ra, Gr/Re_2, Nu).

Based on the data contained in res0.res, different Python scripts can be used to extracts the final results. First, the script Conc_and_rate.py searches for the two species, OH and HO_2, and extract their concentration profiles over the selected time period (24 hours for the marine and stratospheric simulations, and 30 days for the urban simulation). In the marine environment, the OH and HO_2 concentration profiles are displayed in graphs alongside those reported by (Whalley & Furneaux, 2010). The Python script also identifies the most influential reactions responsible for the formation and destruction of both species and displays their impact in the form of aerograms at the time of their peak concentration (1:00 p.m.). In the marine environment the rates are reported at each hour alongside those reported by (Whalley & Furneaux, 2010).

Subsequently, an additional analysis was performed for the marine environment: the brute-force analysis. In this approach, the simulation is repeated as many times as there are reactions under consideration, and in each run, a single reaction is increased by an arbitrary value Δ, in order to assess which reaction has the greatest impact on the concentrations of OH and HO_2. The script Brute_force.py modifies the kinet.dat file before each execution of the box model, and then reads the updated res0.res file, extracting the new peak concentrations of the two species at 1:00 p.m.

In the case of the urban environment, the brute-force analysis was not performed due to its high computational cost. Instead, the impact of NO_x on the simulations was analyzed, both in terms of the HO_2/OH ratio and system stability. The Python script Nitrogen.py modifies the kinet.dat file by changing the initial concentrations of NO and NO_2 before each simulation and reports the ratio between the two species on two separate days.

For all environments, the final post-processing step focuses on assessing the increased impact of H_2 in the atmosphere. The script Hydrogen.py modifies the kinet.dat file by

changing the concentration of H_2 before running the simulation and then extracts the OH values at 1:00 p.m. on the selected days. It also evaluates the OH loss by comparing the modified configuration to the standard one, as well as the new CH_4 concentrations and other parameters required for estimating the global warming potential (GWP) of hydrogen.

The simulation results are presented in the following chapter of the present thesis, where they are discussed in detail and critically analyzed.

A Box Model Equations

Here are reported the equations for the resolutions of the simulations expressed in the paragraph number 2.3. The box model used was developed by Politecnico of Milan. The equations employed for the simulation have been modified from the standard formulation typically used for reactor modelling, with the following assumptions:

1. The Temperature in the air box is constant
2. Integration is performed in the time domain, rather than in dimensionless spatial coordinates
3. Fluxes are assumed to remain constant

Some quantity are kept equal to 0, since are not necessary for the simulation of the atmosphere:

1. th1i = th2i = th3i = 0; no adsorbed species are present
2. NRS = NCS = 0; no surface reactions occur, and no solid components are included.
3. NC = NCG; all species are considered in the gas phase.
4. N_{site} = 0; no solid catalytic sites are present.

- Material Balance (NCG – 1 equations)

$$X\frac{dw_i}{dt} = \frac{\tau}{\rho}\frac{M_i}{M_t}\sum_{j=1}^{NRG}\left(NG_{ij} * RG_j\right) - S_{ti}\left(w_i - w_{is} - \alpha_T * w_i * (1 - w_i)\ln\frac{tg}{ts}\right)$$

- Gas phase stoichiometric equation (1 equation)

$$\sum_{i=1}^{NCG} w_i = 1$$

- Flux balances (NCG – 1 equations)

$$\frac{\tau}{\rho}\frac{M_i}{M_t}Sv\sum_{j=1}^{NRG}\left(NG_{ij} * RG_j\right) = S_{ti}\left(w_i - w_{is} - \alpha_T * w_i * (1 - w_i)\ln\frac{tg}{ts}\right)$$

- Surface stoichiometric equation (1 equation)

$$\sum_{i=1}^{NCG} w_{is} = 1$$

- Overall gas phase material balance (1 equation)

$$0 = -\sum_{i=1}^{NCG} S_{ti}(w_i - w_{is} - \alpha_T * w_i * (1 - w_i) \ln \frac{tg}{ts})$$

- Surface material balance (NCA – Nsite equations)

$$\sum_{j=1}^{NRS} (NS_{ij} * RS_j) = 0$$

- Surface stoichiometry equations (Nsite equations)

$$\sum_{j=1}^{NCA} thkj = 0$$

- Overall energy balance (1 equation)

$$0 = B_{is}\left(t_s - t_g\right) - B_{ie}\left(t_g - t_c\right)$$

The reaction rates are evaluated as follows:

$$RG_j = RG_{fj}\left(1 - \exp\left(\frac{\Delta G_j}{RT}\right)\right)$$

$$RG_{fj} = K_{fj} \prod_{i=1}^{NCG} C_i \; 0_{ij} \qquad 0_{ij} = 0 \; for \; product; \quad 0_{ij} = -NG_{ij} \; for \; reactant$$

$$\Delta G_j = \Delta G_{0j} + RT + \ln \prod_{i=1}^{NCG} a_i * NG_{ij}$$

$$C_i = y_i * \rho$$

$$a_i = \frac{Py_i}{P_{rif}} \ (standard: ideal\ gas, 1\ atm) = \frac{C_i * RT}{1}$$

All the gas phase reactions are assumed reversible, unless specified otherwise, the surface reactions instead are assumed irreversible, and their rate is written as follows:

$$RS_{fj} = K_{fj} * (\prod_{i=1}^{NCG} C_{si} * 0_{sij}) * (\prod_{i=1}^{NCA} (thki * psik) * P_{ij}$$

$0ij\ and\ P_{ij} = 0\ for\ product;\qquad 0ij\ and\ P_{ij} = -NS_{ij}\ for\ reactant\qquad C_{si} = y_{si} * \rho$

3 Results and discussions.

The results and discussions of the simulations are presented below. Each simulation (marine and urban, tropospheric and stratospheric) is discussed in the following order:

1) The first results are obtained using the photochemical data reported by IUPAC (International Union of Pure and Applied Chemistry)
2) The second part shows the results obtained using the data for the photochemical reactions as reported by MCM (master chemical mechanism)
3) The third part uses the MCM values and consider the reactions of HCO and some extra photochemical reactions reported in 2.1.5.1 and 2.1.5.2 paragraphs. The photochemical data of the O_3=>O_2+O^1D reaction is corrected as reported in the 2.1.5.2 paragraph.
4) Subsequently, the results of the brute-force analysis are reported. The results are based on the third configuration and performed only in the marine environment.
5) In the urban environment, a simulation is performed to identify the influence of the nitrogen oxide on the ratio between OH and HO_2
6) The last part reports the impact of the hydrogen increase on the atmosphere in different configurations and the evaluation of the GWP of H_2 (always with the reactions explained in the 3rd point).

3.1. Tropospheric Marine environment

Here are reported the results for the marine environment in the tropospheric layer of the atmosphere for both the GFDL and the LMDz. The concentrations and the rates obtained with both chemical schemes are confronted with the data and the experimental values obtained by (Whalley & Furneaux, 2010), referred as benchmark.

3.1.1 GFDL chemical scheme

The results reported here are obtained by a simulation performed with the chemical reactions taken from (Horowitz, Naik, & Paulot, 2020). The photochemical and marine reactions are changed as described in the 2.1.5 paragraph. The only reactions eliminated are those involving aerosols, VOC-related reactions, and a few in-cloud processes; however, the effect of aerosols is still represented in the graphs.

3.1.1.1. Photochemical data from IUPAC

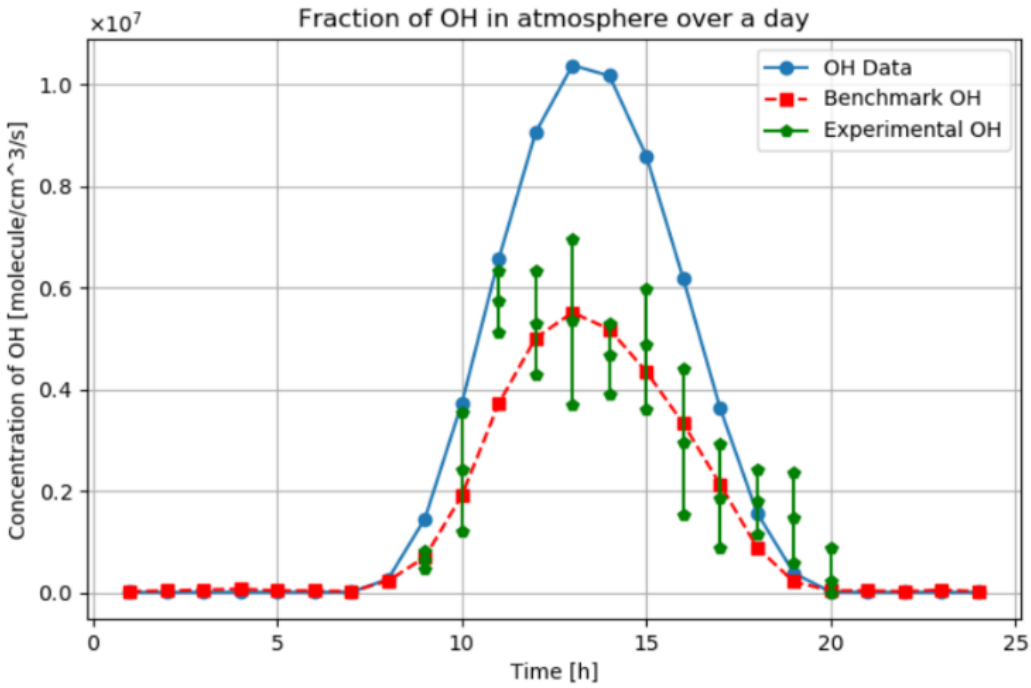

Figure 3.1.1.1: OH concentration profile obtained from GFDL chemical scheme in marine environment with IUPAC photochemical data.

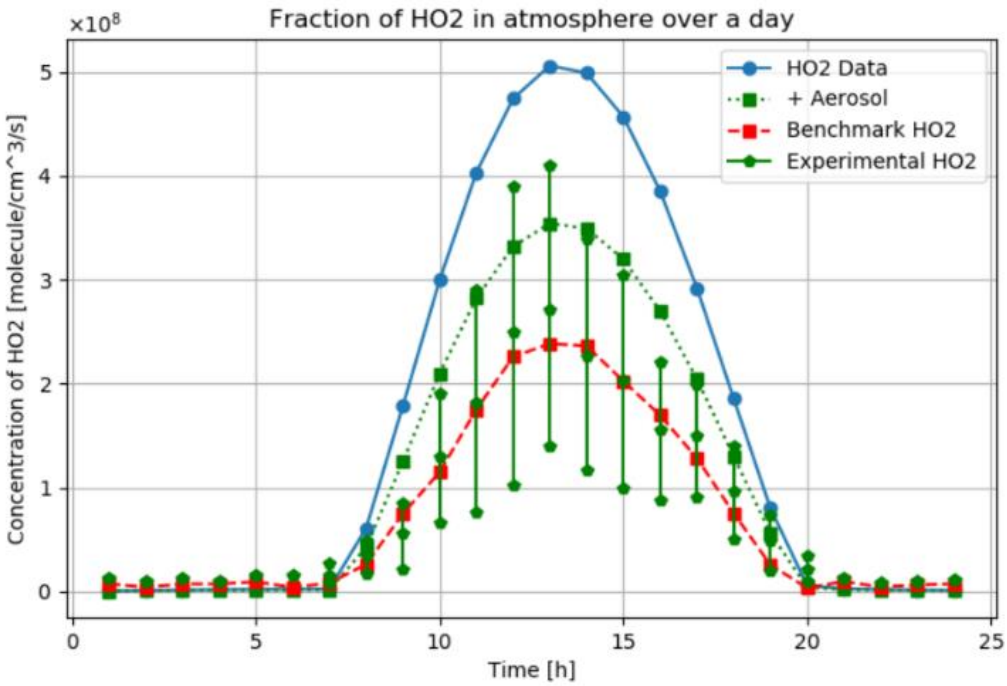

Figure 3.1.1.2: HO_2 concentration profile obtained from GFDL chemical scheme in marine environment with IUPAC photochemical data.

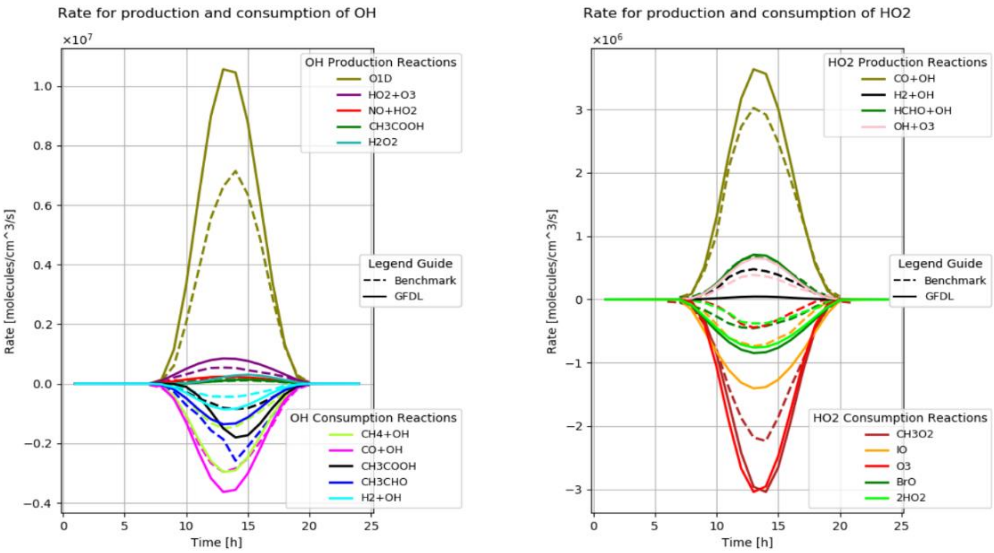

Figure 3.1.1.3: Comparison of the highest reaction rates for the formation and removal of OH and HO_2 with the benchmark from the GFDL chemical scheme, under marine conditions and based on IUPAC photochemical data.

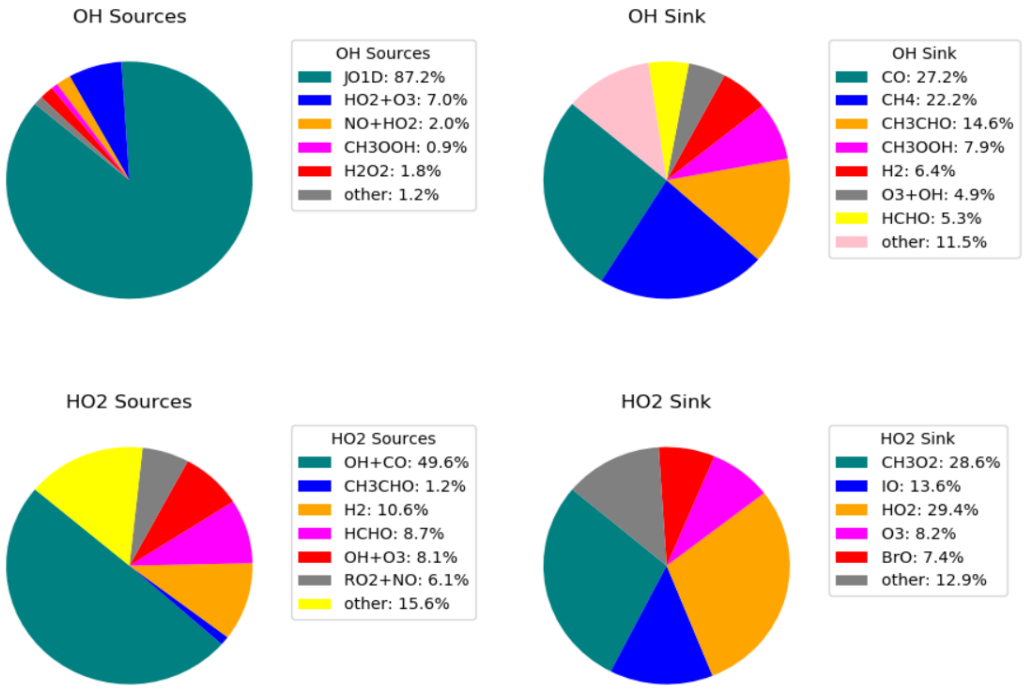

Figure 3.1.1.4: aerograms of the most important reactions contribution for the formation and destruction of OH and HO_2 at 1:00 p.m. with the GFDL chemical scheme, under marine conditions and based on IUPAC photochemical data.

The OH profile obtained shows a peak profile that start at 8:00 a.m. and reaches a maximum value at 1:00 p.m. The values of OH are higher than those reported by (Whalley & Furneaux, 2010), this is probably due to the high value of the photochemical data reported by IUPAC.

The HO_2 profile starts at 8:00 a.m. and reaches a maximum value at 1:00 p.m. The value obtained from our simulation does not account for the contribution of aerosols, which are responsible for approximately 30% of HO_2 removal in the atmosphere. An approximate profile that includes the aerosol contribution is shown as a green dotted line.

The last two figures illustrate the reaction rates of the most significant pathways contributing to the formation and destruction of OH and HO_2, along with their relative contributions as shown in the corresponding aerograms.

The primary source of OH is the reaction between the electronically excited oxygen atom O^1D and water vapor, which produces two OH radicals. The dominant OH sinks are its reactions with CO and CH_4, which together account for approximately 50% of its total removal.

For HO_2, the main formation pathway is the oxidation of CO, contributing to roughly 50% of its production, followed by the reaction between H_2 and OH. The removal of HO_2 primarily occurs via reactions with peroxyl radicals (e.g., CH_3O_2) and through self-reaction ($HO_2 + HO_2$).

The contribution of the HO_2 self-reaction appears to be overestimated compared to the benchmark. This discrepancy is attributed to the different rate constant adopted by the GFDL mechanism, particularly regarding the role of H_2O in influencing reaction rates, as discussed in Section 2.1.4.

3.1.1.2. Photochemical data from MCM

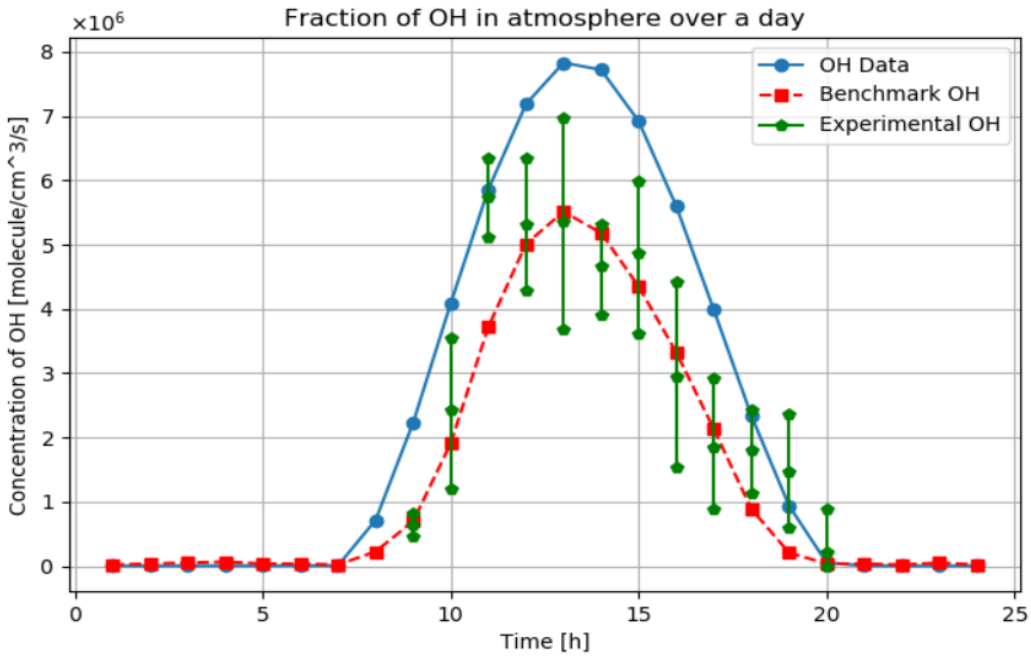

Figure 3.1.1.5: OH concentration profile obtained from GFDL chemical scheme in marine environment with MCM photochemical data

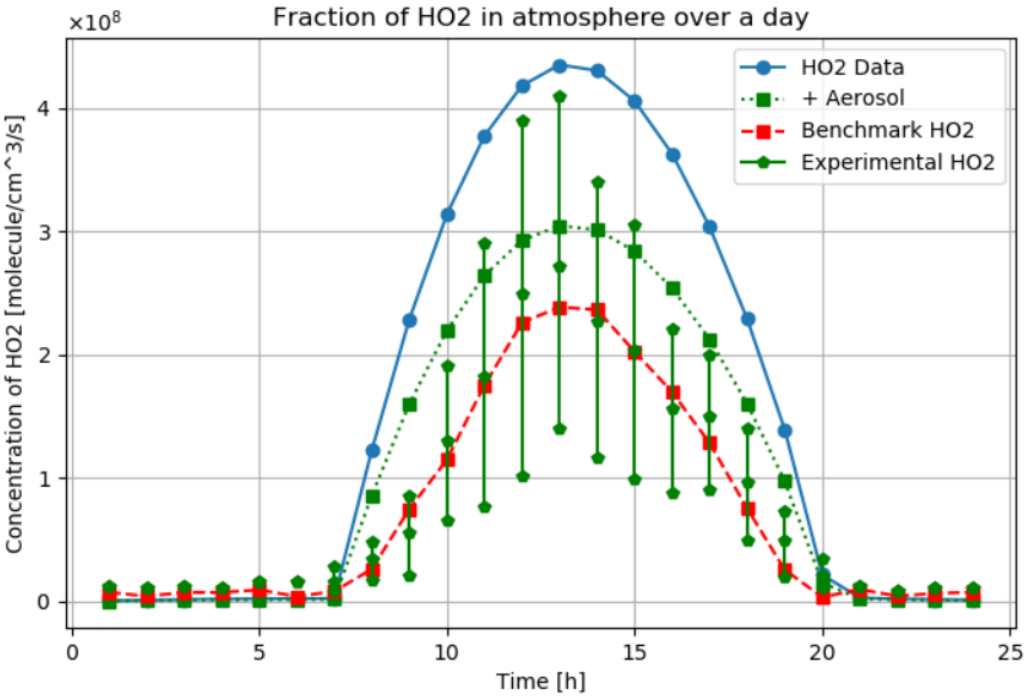

Figure 3.1.1.6: HO_2 concentration profile obtained from GFDL chemical scheme in marine environment with IUPAC photochemical data.

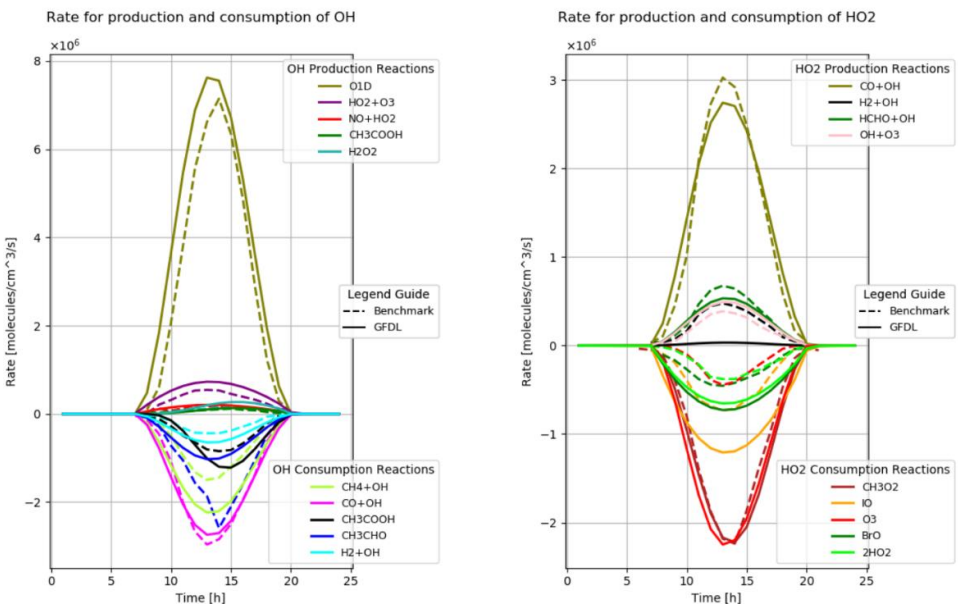

Figure 3.1.1.7: Comparison of the highest reaction rates for the formation and removal of OH and HO_2 with the benchmark from the GFDL chemical scheme, under marine conditions and based on MCM photochemical data.

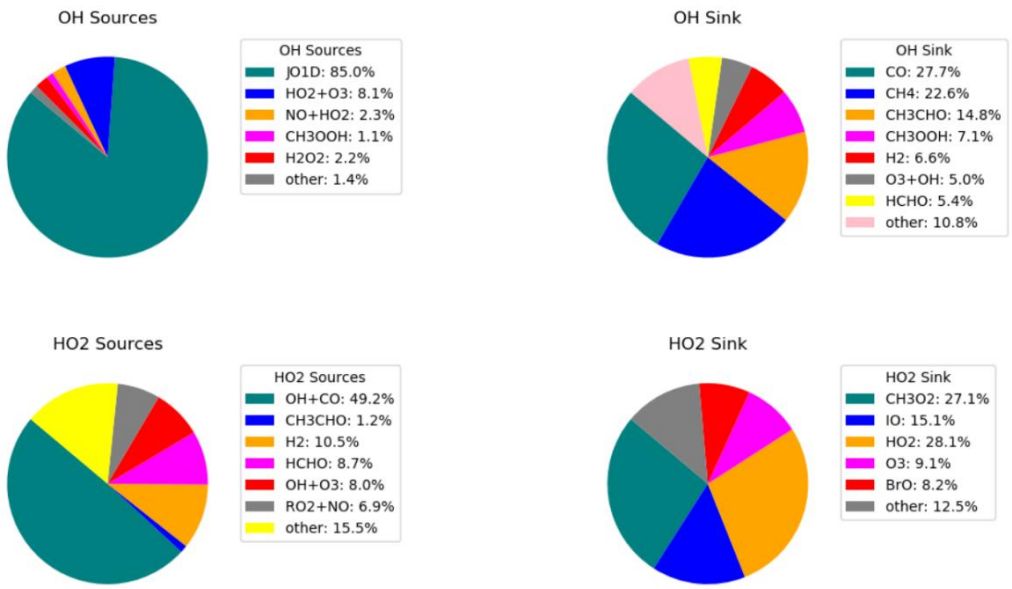

Figure 3.1.1.8: aerograms of the most important reactions contributions for the formation and destruction of OH and HO_2 at 1:00 p.m. with the GFDL chemical scheme, under marine conditions and based on MCM photochemical data.

The OH concentrations obtained using the photochemical data from the MCM database are much closer to those reported by the benchmark, particularly to the experimental values. This improvement is primarily due to the lower rate constants used for the photochemical reactions.

The HO_2 profile is also closer to the one reported by (Whalley & Furneaux, 2010), especially considering the contribution of aerosols.

The rates obtained using the second configuration align more closely with those reported by (Whalley & Furneaux, 2010). In particular, the formation rate of OH from O^1D and the formation and destruction rates of HO_2 via CO + OH and CH_3O_2, respectively, are now more consistent with the benchmark. These results indicate that the use of photochemical data from the MCM database enables simulations that better reproduce the benchmark behaviour compared to those based on IUPAC recommended data.

3.1.1.3. Photochemical data from MCM and added reactions

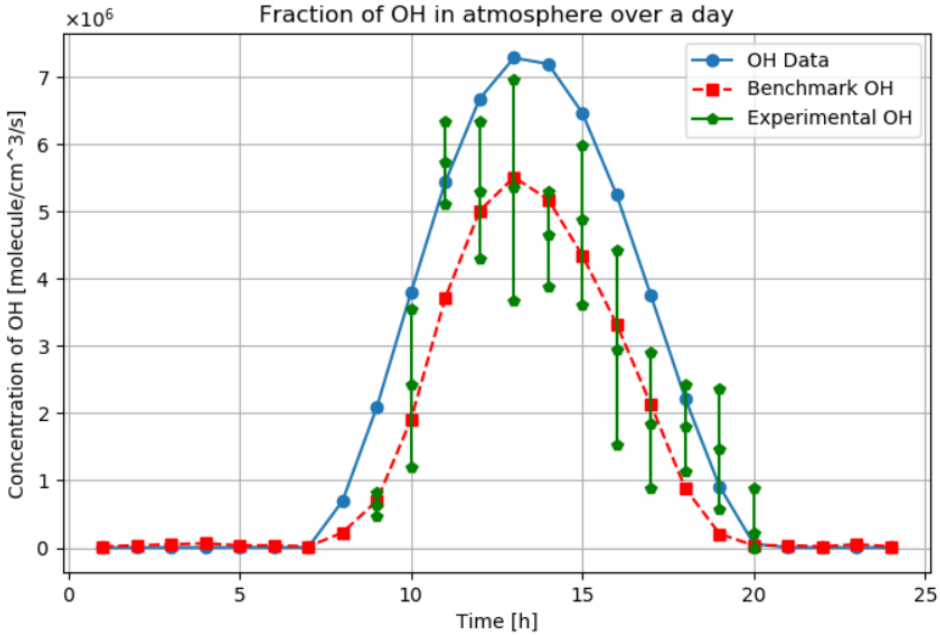

Figure 3.1.1.9: OH concentration profile obtained from GFDL chemical scheme in marine environment with MCM photochemical data and the added reactions

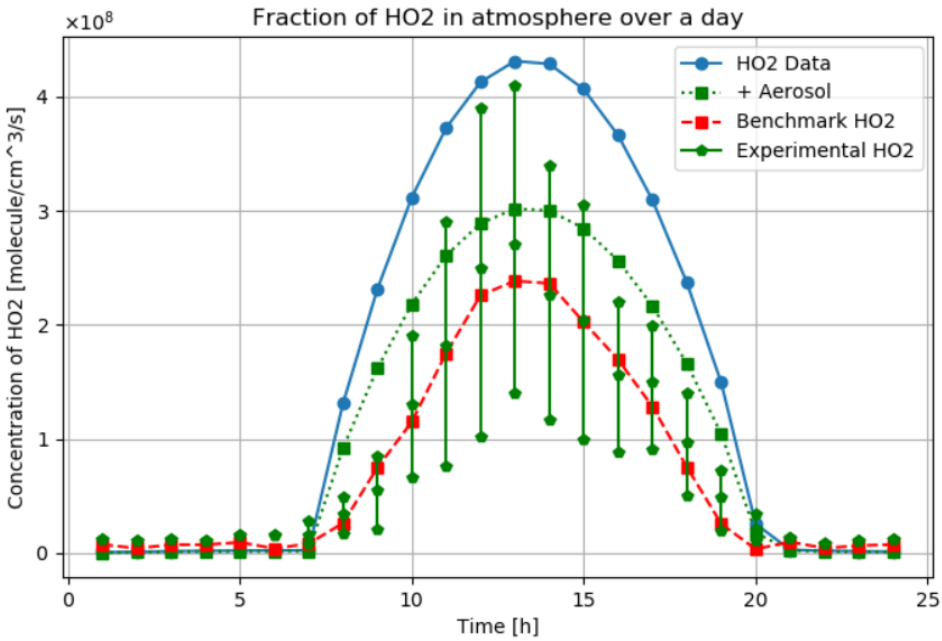

Figure 3.1.1.10: HO_2 concentration profile obtained from GFDL chemical scheme in marine environment with MCM photochemical data and the added reactions

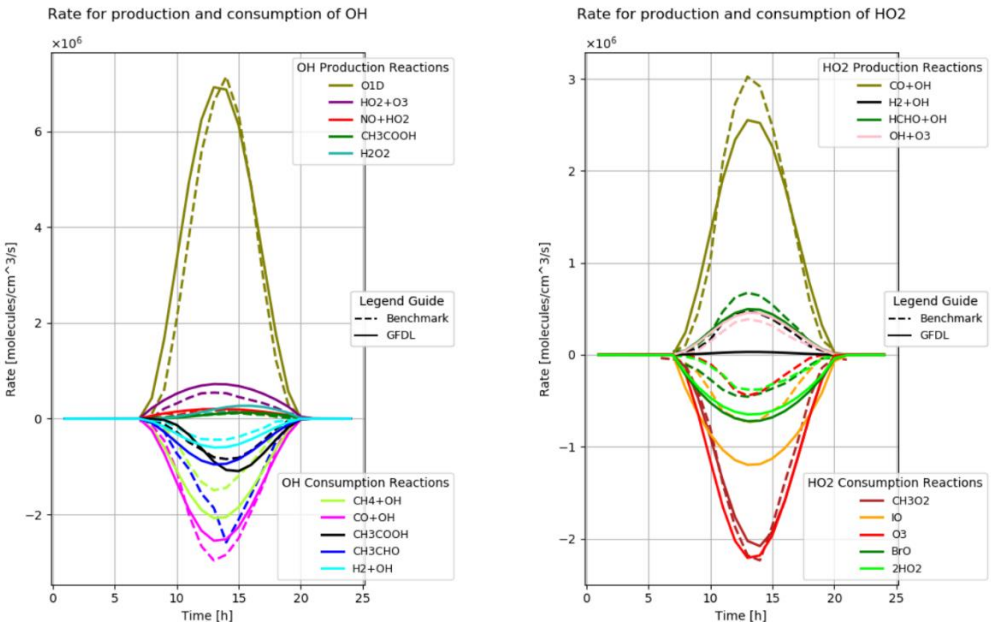

Figure 3.1.1.11: Comparison of the highest reaction rates for the formation and removal of OH and HO_2 with the benchmark from the GFDL chemical scheme, under marine conditions, based on MCM photochemical data and the added reactions

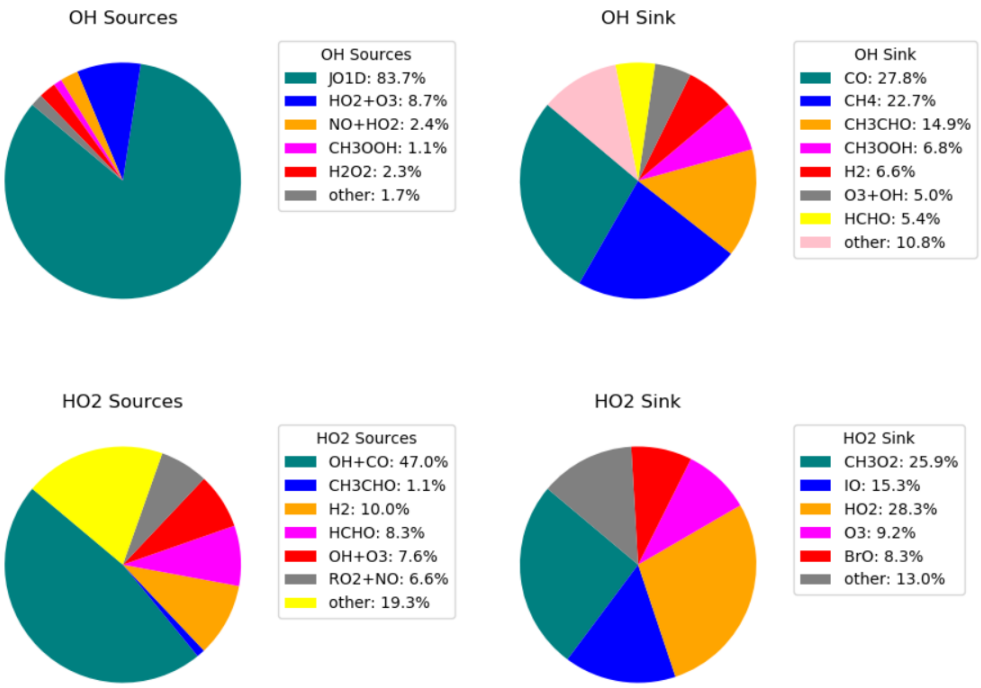

Figure 3.1.1.12: aerograms of the most important reaction contribution for the formation and destruction of OH and HO_2 at 1:00 p.m. with the GFDL chemical scheme, under marine conditions, based on MCM photochemical data and the added reactions

The difference between the second and the third simulation is smaller than the one between the first and the second. Even so, with the change in the photochemical reaction data of the reaction $O_3 \Rightarrow O_2 + O^1D$ and the reactions added for describing the HCO atmospheric contribution, the profile now fits the experimental values reported by (Whalley & Furneaux, 2010). The reason why the profile obtained follows the upper experimental values and not exactly the benchmark is probably due to lack of a description of the VOCs reactions. Nevertheless, this configuration is the best obtained to emulate the benchmark, so all the results for the GFDL chemical scheme in marine environment are reported with this set-up.

The HO_2 concentration is even more consistent with the benchmark than the OH one, likely due to the reaction mechanism employed for the $HO_2 + HO_2 \rightarrow H_2O_2 + O_2$ pathway. Although VOCs are not included, this mechanism contributes to further reducing HO_2 levels, an effect not considered in the benchmark.

The final reaction rates are presented in the figures 3.1.1.11 and 3.1.1.12. Across the three proposed simulations, the rates of the third one are more capable of reproducing the data reported in the benchmark. The main contributors to both OH and HO_2 dynamics remain consistent. Notably, the reaction between H_2 and OH, leading to the formation of HO_2, maintains a significant role in all configurations, accounting for approximately 6% of OH removal and 10% of HO_2 production. These findings highlight that the contribution of atmospheric H_2 is far from negligible when assessing the mechanisms involved in the removal of greenhouse gases.

3.1.1.4. Brute force analysis in marine environment with the GFDL mechanism.

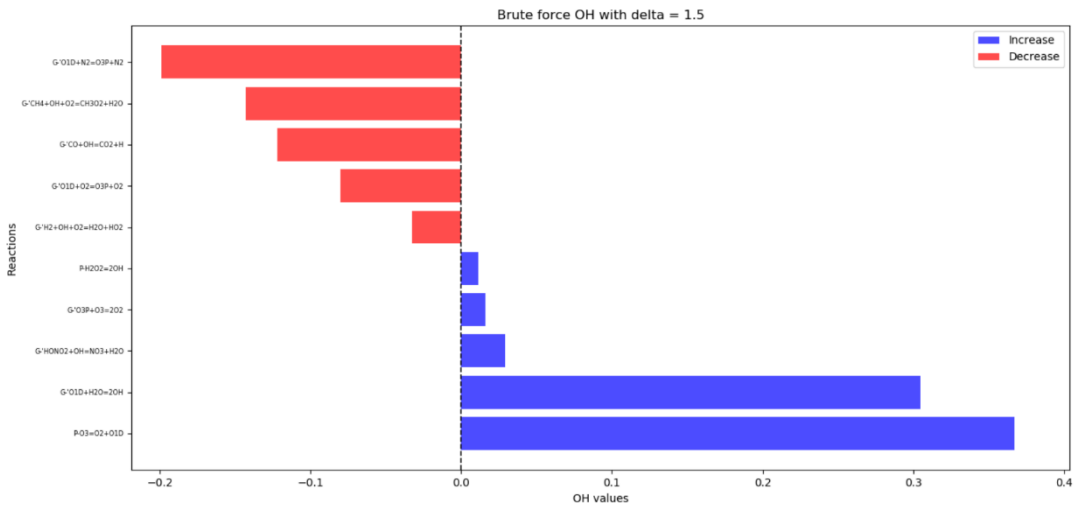

Figure 3.1.1.13: Brute force analysis of OH with GFDL chemical scheme in marine environment

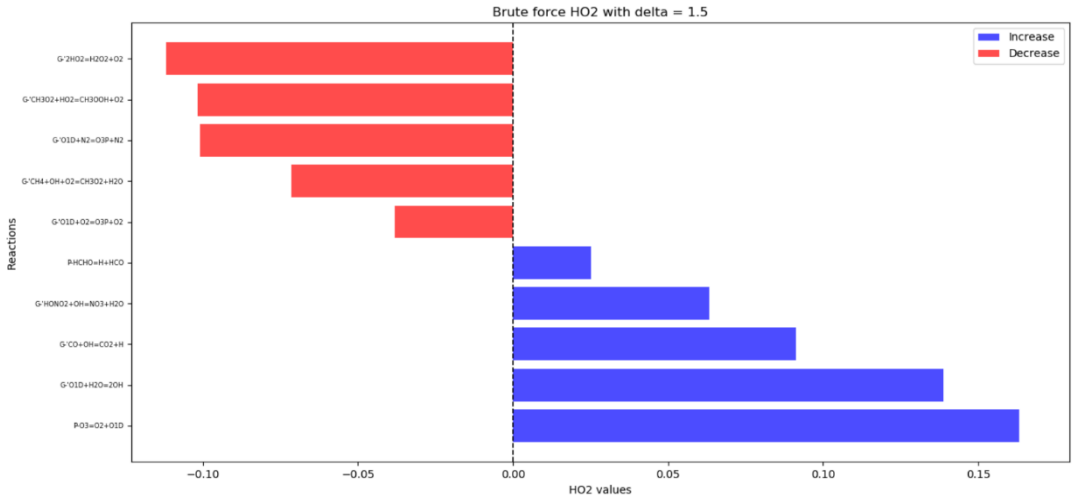

Figure 3.1.1.14: Brute force analysis of HO_2 with GFDL chemical scheme in marine environment

This brute force sensitivity analysis evaluates the impact of individual reactions on the concentrations of hydroxyl (OH) and hydroperoxyl (HO_2) radicals by increasing each reaction's rate constant by 50% ($\Delta = 1.5$).

The findings indicate that the primary contributors to the formation and depletion of OH are not the reactions directly involving OH itself but rather those affecting the concentration of excited singlet oxygen atoms, O^1D. Notably, enhancing the rate

constant of ozone photodissociation significantly increases the OH concentration. Conversely, reactions that consume O^1D, such as its quenching by N_2 and O_2, substantially reduce OH levels.

Similarly, the formation of HO_2 is strongly influenced by the production of O^1D, as O^1D reacts rapidly with H_2O to produce OH, which subsequently leads to HO_2 formation. The most sensitive pathway for HO_2 removal is its self-reaction ($HO_2 + HO_2 \Rightarrow H_2O_2 + O$).

These results show the importance of a deeper understanding of the photolysis of the oxygen species for a better understanding of the atmospheric reactivity.

3.1.1.5. Impact of H_2 increase on atmospheric reactivity

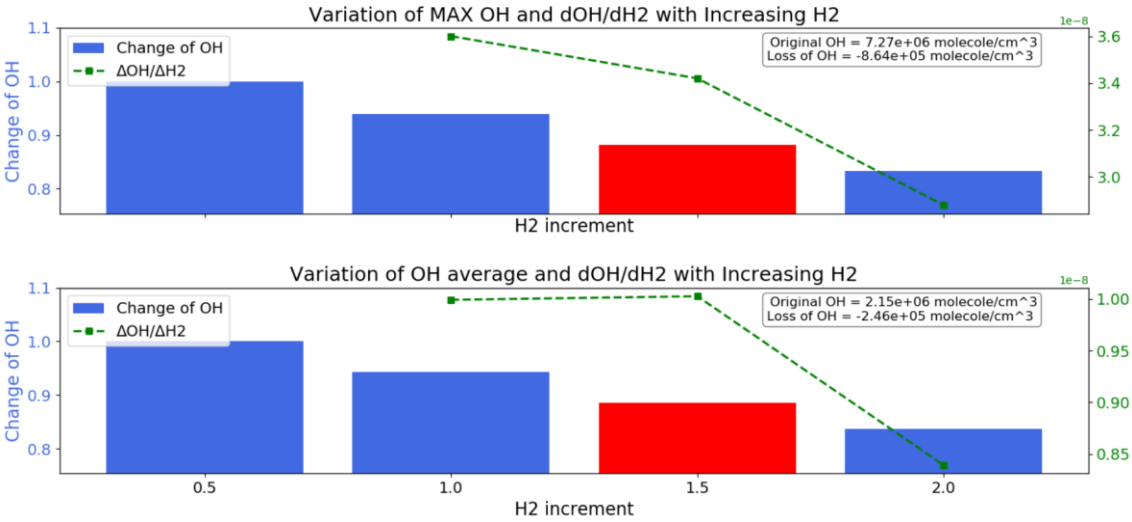

Figure 3.1.1.15: Effect of increasing H_2 on both the maximum and the average OH with GFDL chemical scheme. The total loss of OH is calculated between the initial value and the one with 1.5ppm of hydrogen in atmosphere.

Graph 3.1.1.15 illustrates the effect of increased hydrogen levels on both its peak concentration (at 1:00 p.m.) and its average value, as adopted in the study by (Warwick & Griffiths, 2022). It is evident that a rise in atmospheric H_2 concentration leads to a decrease in OH levels.

With the GFDL chemical scheme, the reduction in the daily peak OH concentration amounts to 8.64×10^5 molecules cm^{-3}. Given that the peak OH value without additional H_2 is 7.3×10^6 molecules cm^{-3}, this represents a decrease of more than 10% of the original value. A similar trend is observed for the daily mean OH concentration, which shows a reduction of 2.5×10^5 molecules cm^{-3}.

For comparison, the benchmark simulation predicts a reduction of approximately 0.9 × 10^5 molecules cm^{-3} in the daily mean value, which is less than half of the loss estimated using the GFDL mechanism. This discrepancy is due to differences in the kinetic rate constant used for the CH_4 + OH reaction. Warwick's study employs a rate constant of 2.8 × 10^{-15} cm^3/molecule/s, whereas the GFDL mechanism adopts a significantly higher value of 6.36×10^{-15} cm^3/molecule/s.

The difference between the two rates lies in the fact that (Warwick & Griffiths, 2022) use a rate averaged over the entire year and across all possible conditions. In contrast, the rate we adopted refers to a specific configuration: May 22, under perfectly mixed air conditions and clear skies. This setup considers photochemical reaction rates close to their annual maximum, along with a temperature of 25 °C, which is higher than the yearly average. As a result, this configuration leads to an overestimation of hydrogen's GWP, especially when derived from OH concentrations at 1:00 p.m.

	Loss of OH [molecules/cm^3]	new CH_4 [molecules/cm^3]	dOH/dH_2	a	GWP [100]
Max OH	8.64E+5	2183	3.51E-8	0.315	81.74
Average OH	2.46E+5	2183	1.02E-8	0.0917	23.79

Table 3-1: parameters for the evaluation of the GWP of H_2 derived from both maximum and average value of OH.

The GWP(100) values reported in the benchmark range from 2.0 to 7.0, reflecting the challenges in evaluating the soil sink of H_2. The GWP obtained using the GFDL chemical model is significantly higher, due to the considerations discussed above.

3.1.2. LMDz chemical scheme

The results reported here are obtained by a simulation performed with the chemical reactions taken form (Folberth, Hauglustaine, Lathière, & Brocheton, 2006). The photochemical reactions and the marine ones are changed as described in the 2.1.5 paragraph. The only reactions eliminated are the aerosol, the VOCs related and the few in-cloud, but the effect of the aerosol is still represented in the graphs.

3.1.2.1. Photochemical data from IUPAC

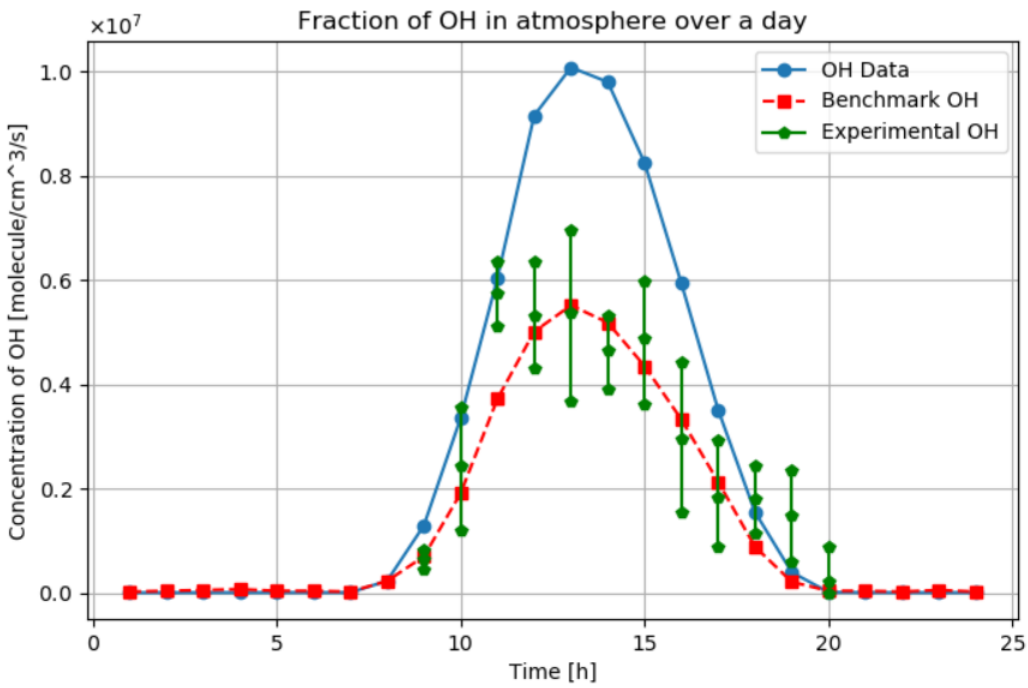

Figure 3.1.2.1: OH concentration profile obtained from LMDz chemical scheme in marine environment with IUPAC photochemical data.

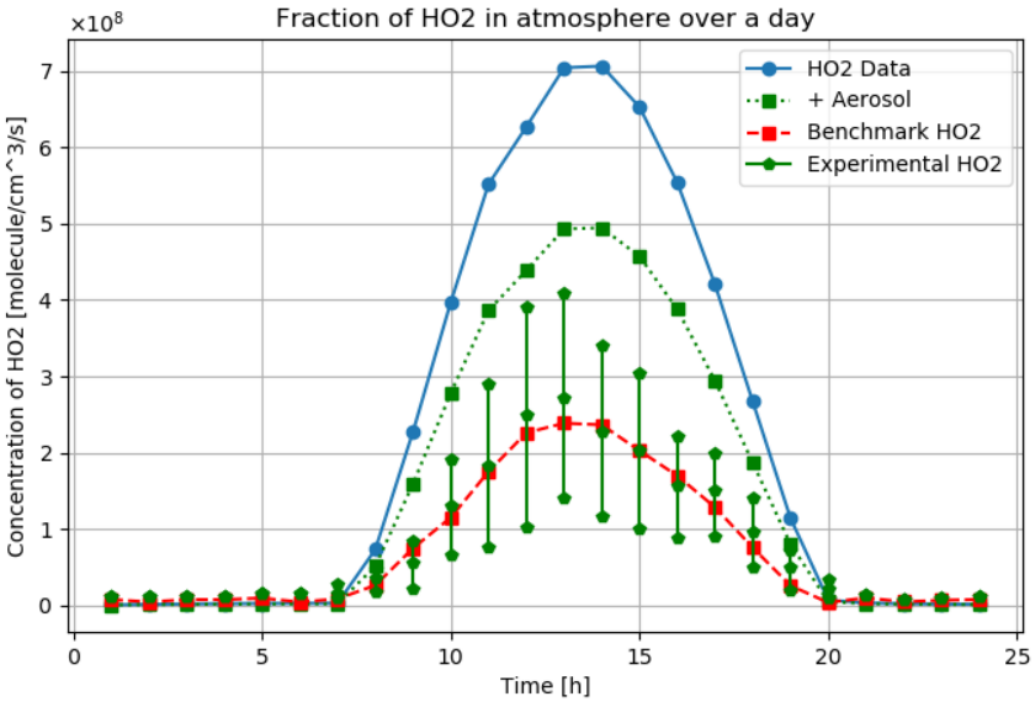

Figure 3.1.2.2: HO_2 concentration profile obtained from LMDz chemical scheme in marine environment with IUPAC photochemical data.

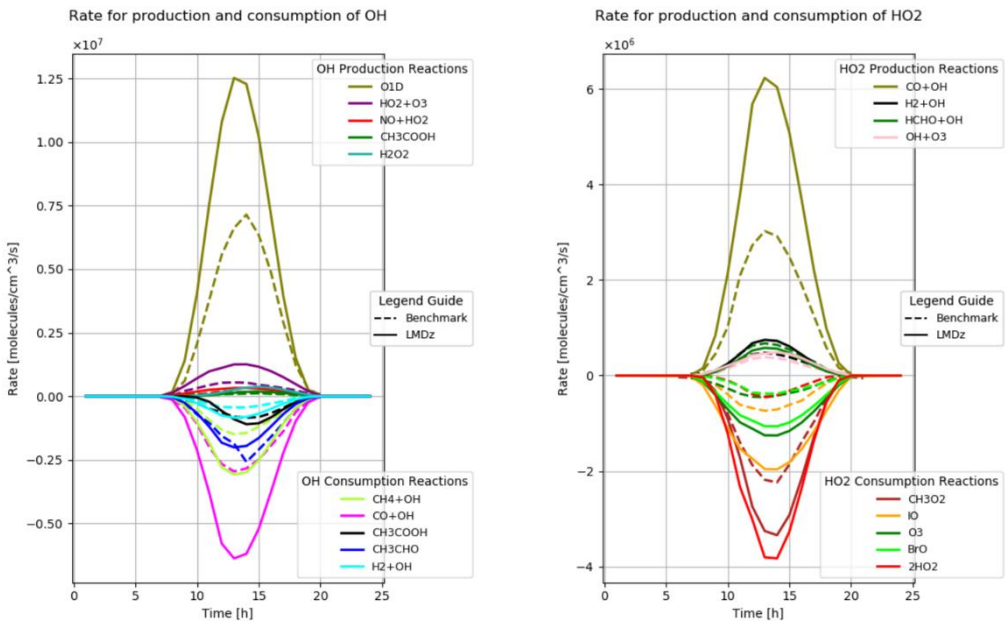

Figure 3.1.2.3: Comparison of the highest reaction rates for the formation and removal of OH and HO_2 with the benchmark from the LMDz chemical scheme, under marine conditions, based on IUPAC photochemical data.

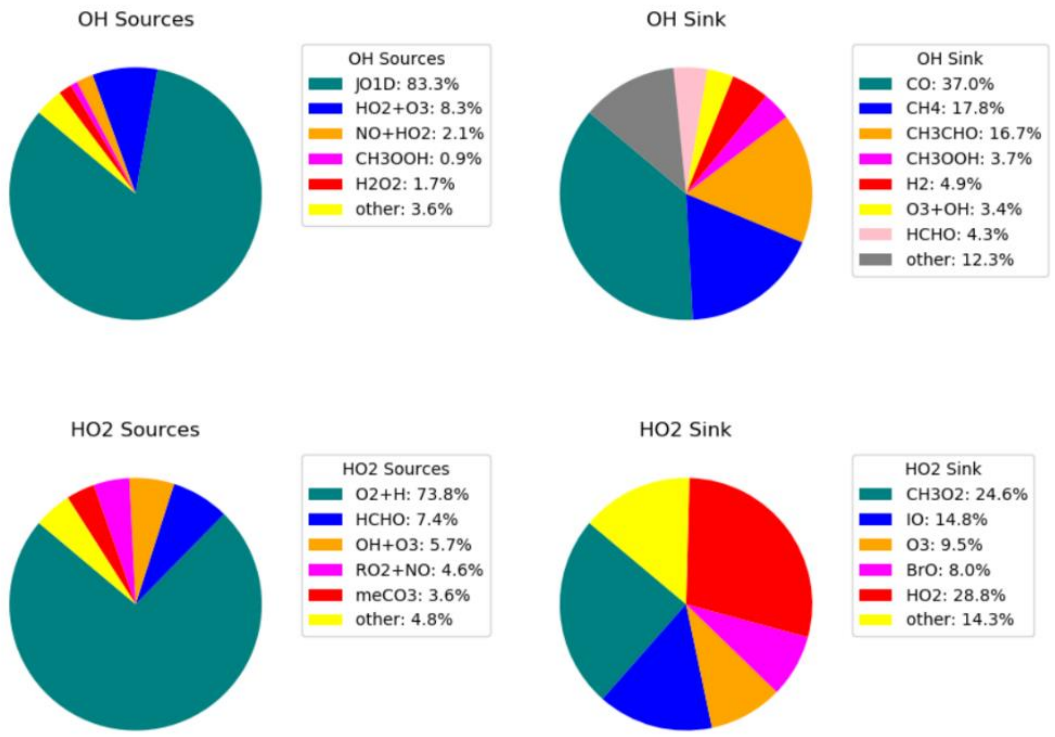

Figure 3.1.2.4: aerograms of the most important reaction contribution for the formation and destruction of OH and HO_2 at 1:00 p.m. with the LMDz chemical scheme, under marine conditions, based on IUPAC photochemical data.

The configuration shown here exhibits the same behavior as the GFDL simulation, the results obtained using the data from the IUPAC database are overestimated compered to the benchmark.

The same goes for the HO_2, where the profile is significantly higher than the benchmark.

The main contributors for the formation of OH and HO_2 are almost the same as the one obtained using the GFDL chemical scheme. The contribution of the CO + OH reaction is higher due to the different configuration of the kinetic mechanism described in the 2.1.4 paragraph.

In the LMDz chemical scheme, some reactions include an intermediate step involving the formation of the H radical, which subsequently reacts with O_2 to form HO_2. In figure 3.1.2.4, this reaction is shown as the main contributor to OH formation, although it actually represents the sum of three distinct reactions, as detailed in figure 3.1.2.5.

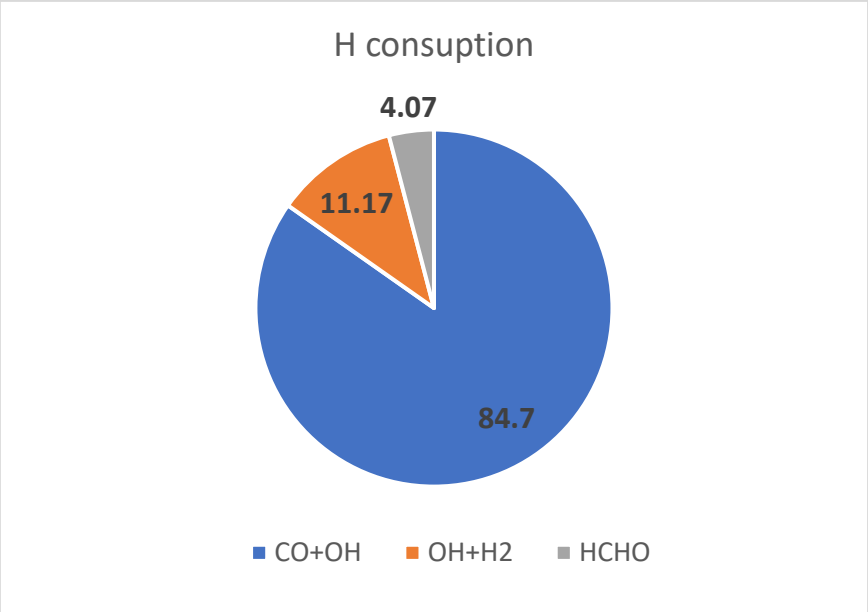

Figure 3.1.2.5: contribution in the elimination of H

3.1.2.2. Photochemical data from MCM

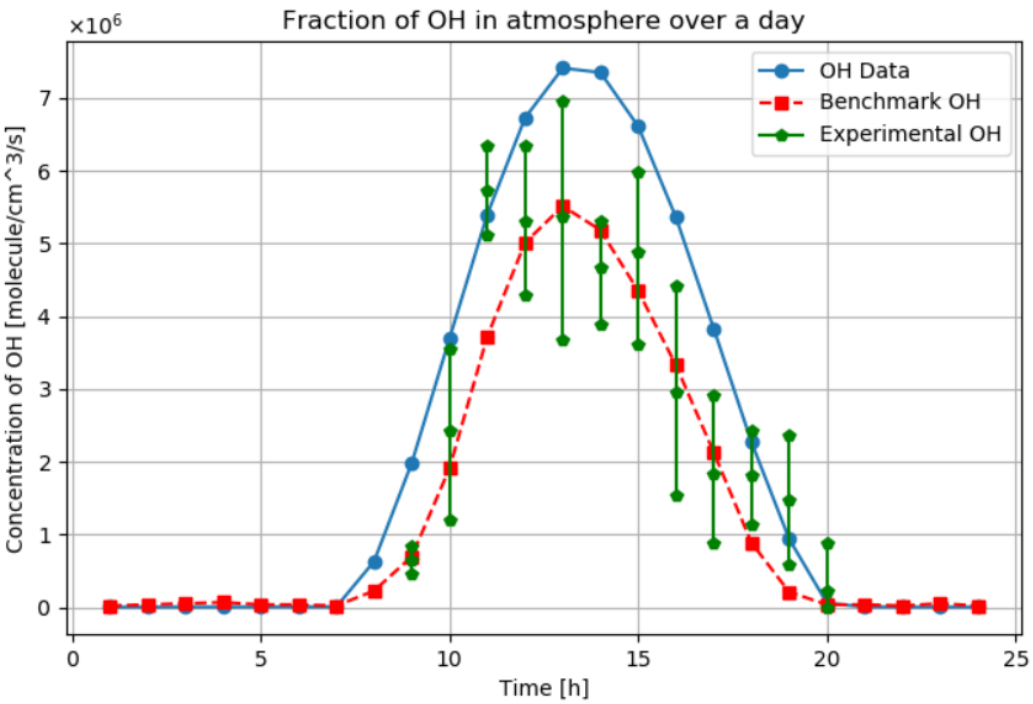

Figure 3.1.2.6: OH concentration profile obtained from LMDz chemical scheme in marine environment with MCM photochemical data.

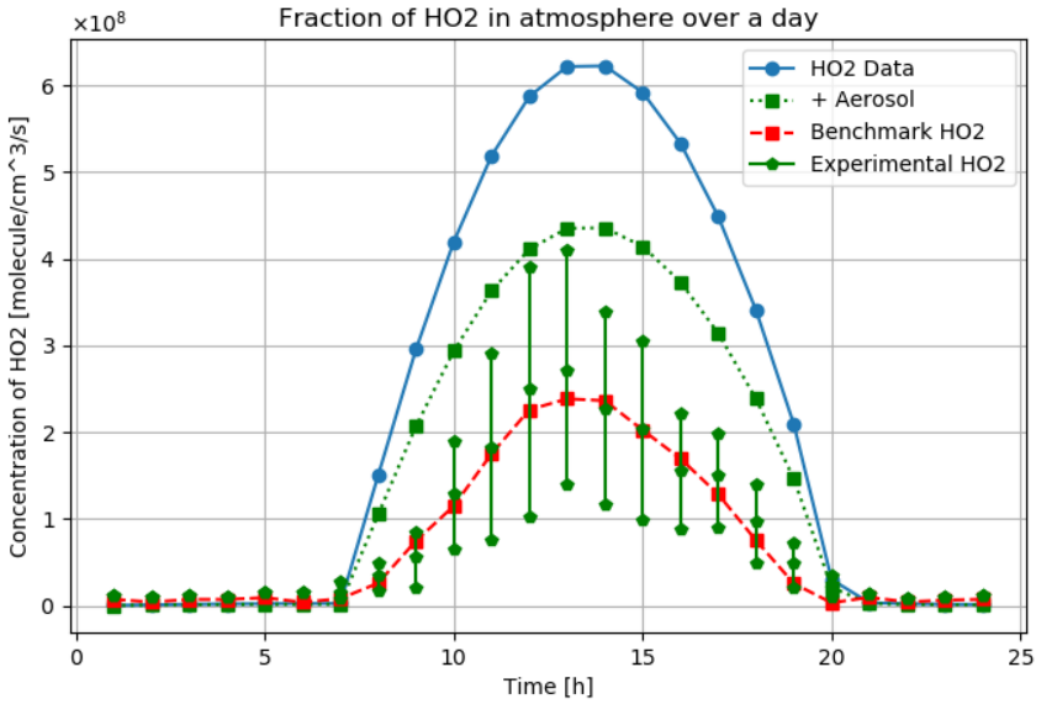

Figure 3.1.2.7: HO_2 concentration profile obtained from LMDz chemical scheme in marine environment with MCM photochemical data.

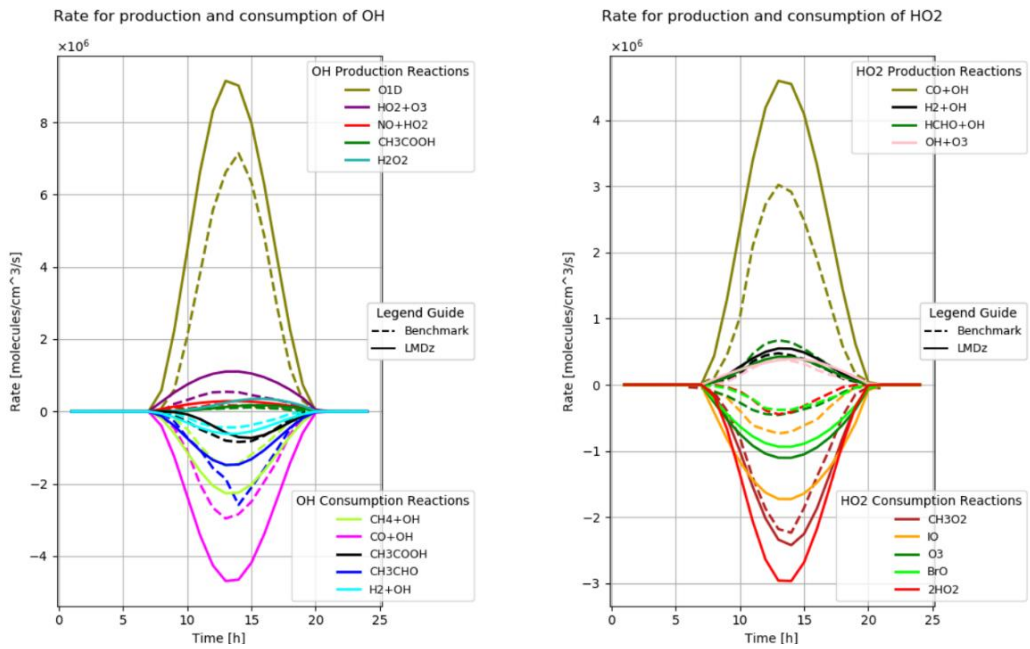

Figure 3.1.2.8: Comparison of the highest reaction rates for the formation and removal of OH and HO_2 with the benchmark from the LMDz chemical scheme, under marine conditions, based on MCM photochemical.

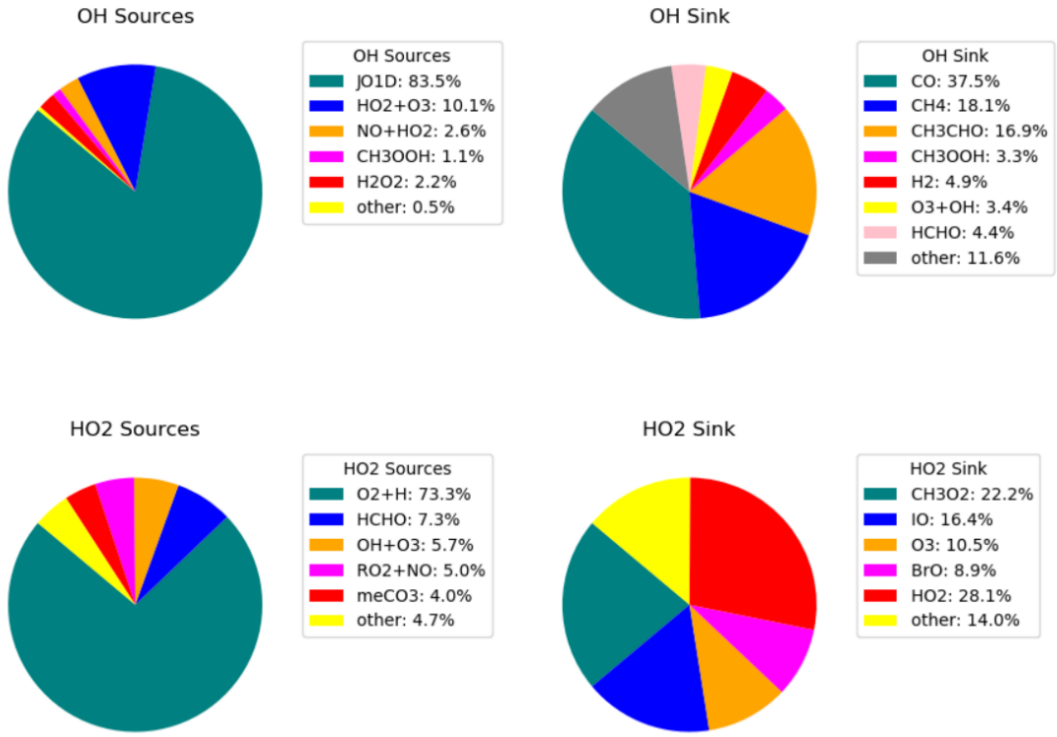

Figure 3.1.2.9: aerograms of the most important reaction contribution for the formation and destruction of OH and HO_2 at 1:00 p.m. with the LMDz chemical scheme, under marine conditions, based on MCM photochemical data.

With the photochemical data taken from the MCM the OH profile is now closely resembles the benchmark; again, this set-up is much more capable of reproducing the results proposed by the literature.

The HO_2 concentration is also closer to the benchmark, but higher than that obtained using the GFDL mechanism, due to a different structure of the CO + OH reaction, which leads to increased HO_2 levels.

The reaction rates are now again more consistent with those described in the benchmark, except for the reaction between the carbon monoxide and OH, that is significantly higher due to its different structure.

The contributions to H formation are the same as those reported in Figure 3.1.2.5.

3.1.2.3. Photochemical data from MCM with added reactions

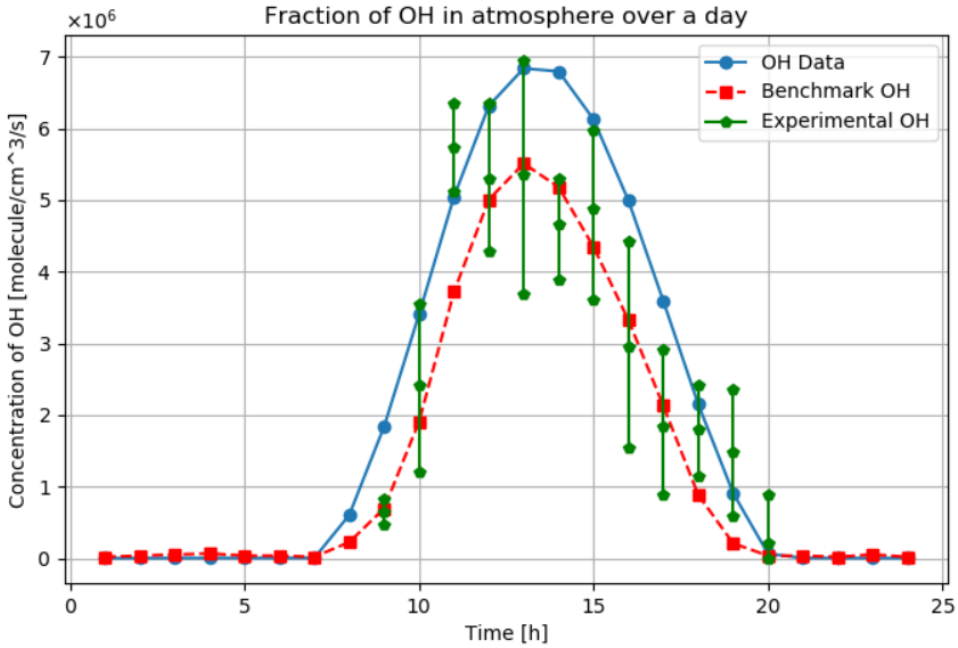

Figure 3.1.2.10: OH concentration profile obtained from LMDz chemical scheme in marine environment with MCM photochemical data and added reactions

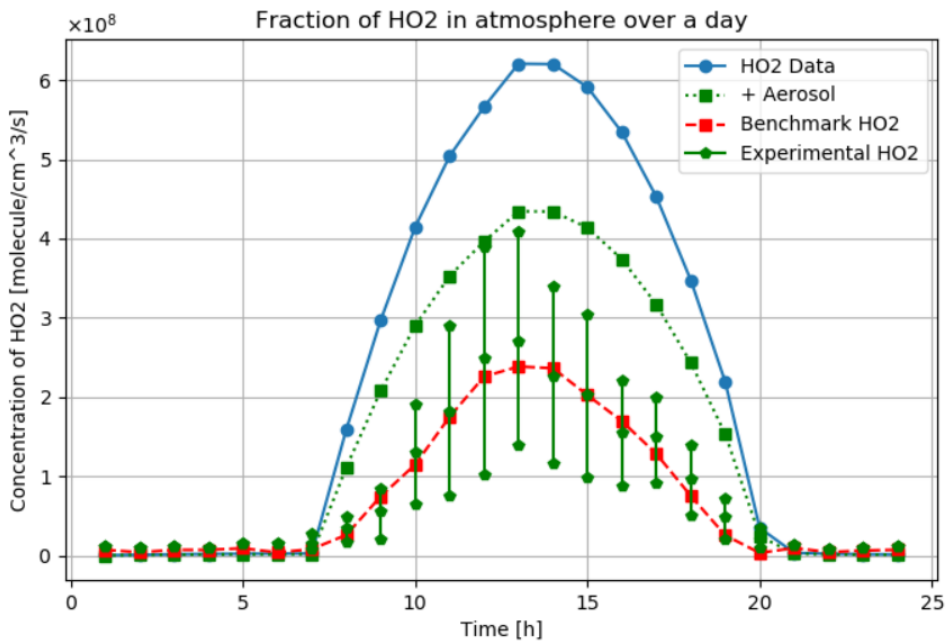

Figure 3.1.2.11: HO_2 concentration profile obtained from LMDz chemical scheme in marine environment with MCM photochemical data and added reactions

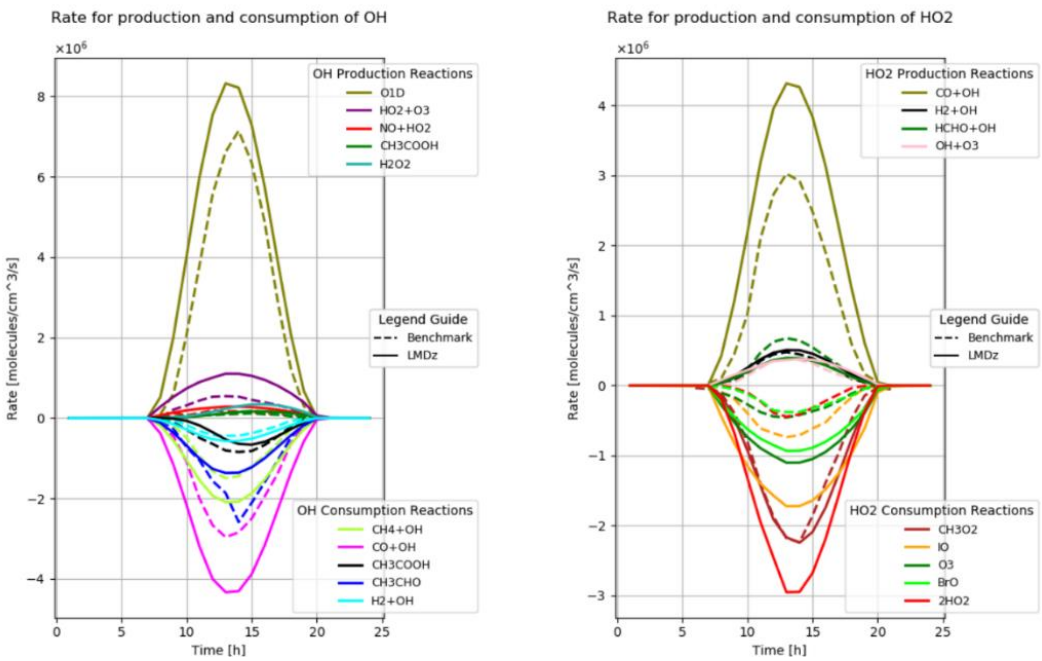

Figure 3.1.2.12: Comparison of the highest reaction rates for the formation and removal of OH and HO_2 with the benchmark from the LMDz chemical scheme, under marine conditions, based on MCM photochemical and added reactions

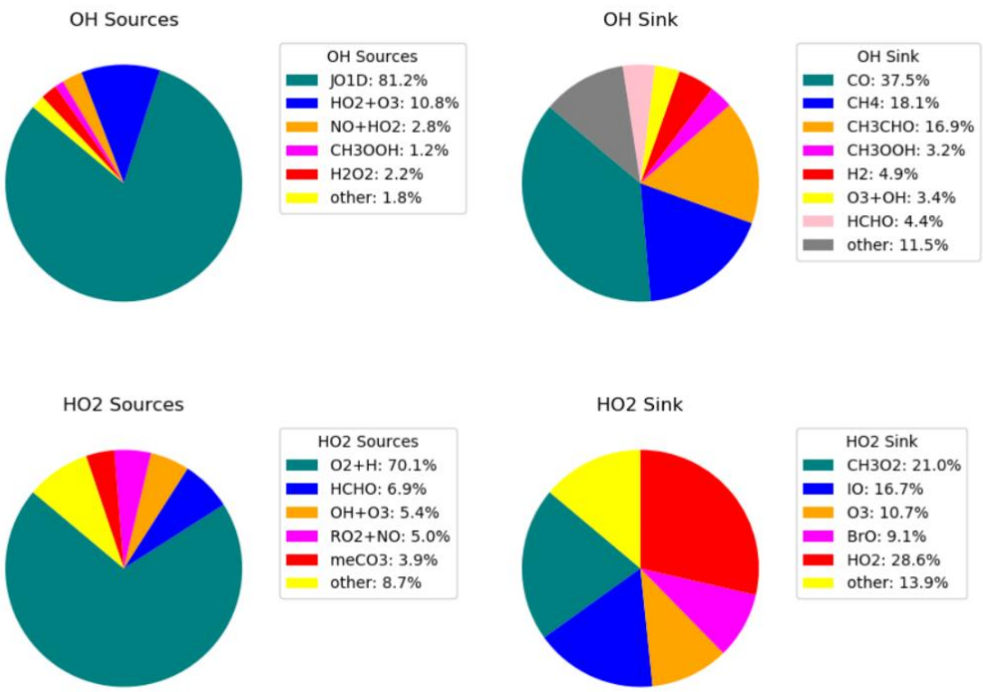

Figure 3.1.2.13: Comparison of the highest reaction rates for the formation and removal of OH and HO_2 with the benchmark from the LMDz chemical scheme, under marine conditions, based on MCM photochemical and added reactions.

As with the GFDL chemical scheme, this last configuration can replicate much better the data obtained by (Whalley & Furneaux, 2010). The OH profile is nearly identical to the one reported in figure 3.1.1.9; while the HO_2 levels are slightly higher, but nonetheless in accord with the benchmark. The rates profile and their contribution shown in the aerographs remain almost constant throughout the three different simulations, and in good agreement with the results obtained with the GFDL mechanism.

The contributions to H formation are the same as those reported in Figure 3.1.2.5.

3.1.2.4. Brute force analysis in marine environment with the LMDZ mechanism.

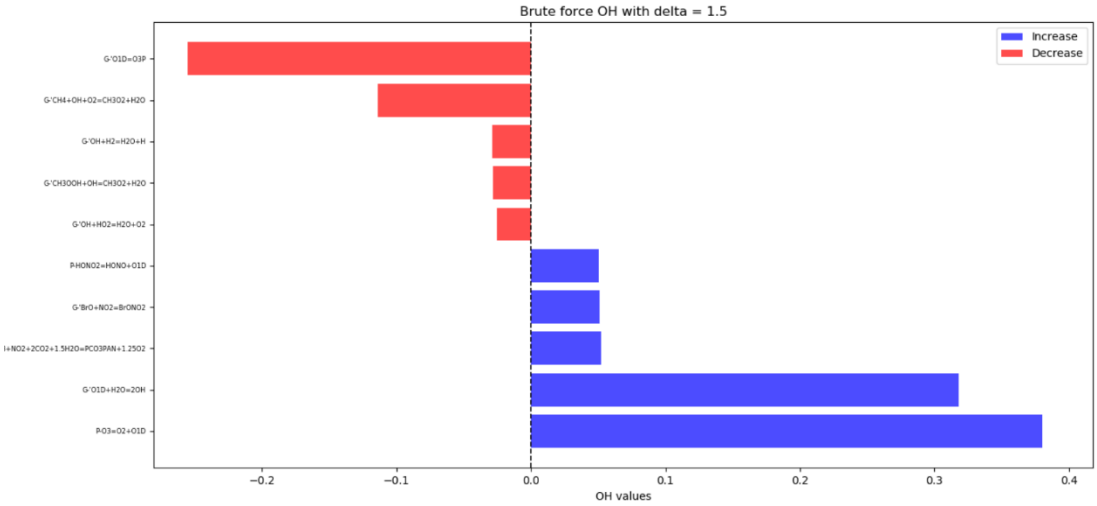

Figure 3.1.2.14: Brute force analysis of OH

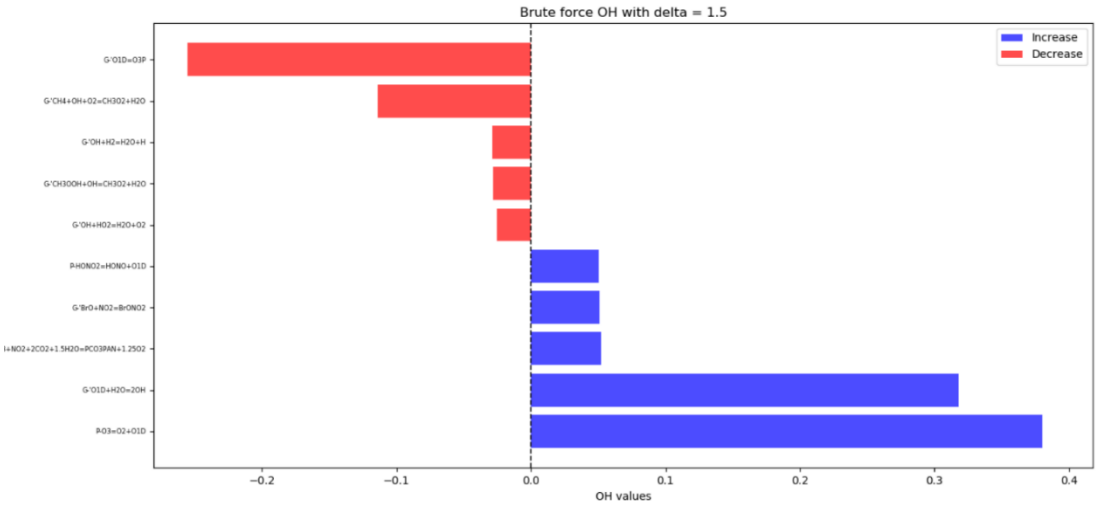

Figure 3.1.2.15: Brute force analysis of HO_2

The brute force analysis for the LMDz simulation is quite similar to that performed for GFDL. Once again, the most influential species affecting both OH and HO_2 is O^1D; its quenching to O^3P via N_2 represents by far the dominant pathway for reducing OH and HO_2 levels. Conversely, the photodissociation of O_3 is the most important source of singlet oxygen and plays a key role in the formation of OH and HO_2.

3.1.2.5. Impact of H_2 increase on atmospheric reactivity

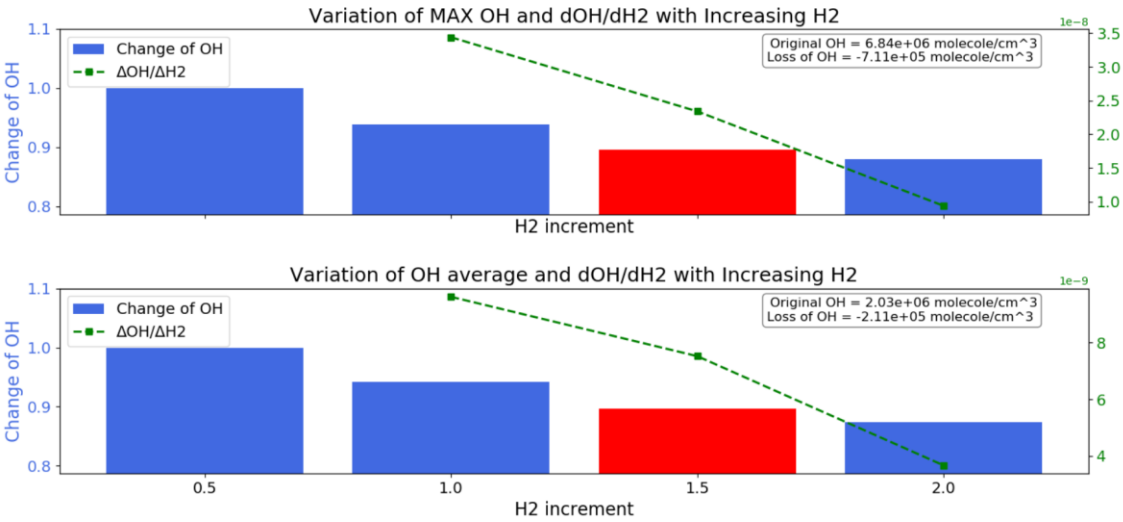

Figure 3.1.2.16: Effect of increasing H_2 on both the maximum and the average OH with LMDz chemical scheme. The total loss of OH is between the initial value and the one with 1.5ppm of hydrogen in atmosphere.

The effect of the hydrogen increase shown in Figure 3.1.2.16 confirms that its impact on OH levels in the tropospheric marine environment is not negligible. At 1:00 p.m. (the peak level), the total OH loss with a tripled atmospheric H_2 concentration is estimated to be around 7.11×10^5 molecules cm^{-3}, while the average values decrease by approximately 2.11×10^5 molecules cm^{-3}.

The results are in complete agreement with the those obtained from the simulations with the GFDL model but again show a larger effect than those reported by Warwick, for the same reason discussed in the 3.1.1.5 paragraph.

Nevertheless, the effect of the hydrogen accumulation in troposphere and in marine environments are confirmed with the one reported in literature.

	Loss of OH [molecules/cm^3]	new CH_4 [molecules/cm^3]	dOH/dH_2	a	GWP [100]
Max OH	7.11E+5	2183	2.89E-8	0.260	67.47
Average OH	2.11E+5	2183	8.57E-9	0.077	19.98

Table 3-2: parameters for the evaluation of the GWP of H_2 derived from both maximum and average value of OH.

The GWP [100] reported in the table 3-2 are almost the same as those obtained with the GFDL mechanism.

3.2. Tropospheric Urban environment

The following results refer to simulations conducted in an urban environment within the tropospheric layer. Compared to the marine environment, the urban atmosphere is characterized by significantly higher levels of pollution, particularly nitrogen oxides (NO and NO_2) and their derivatives. These compounds play a central role in the formation and depletion mechanisms of OH and HO_2 radicals. The literature reports a wide range of possible results in term of concentration and the ratio between the OH and HO_2, due to the difficulty on the description of the polluted condition (Dusanter, Vimal, & Stevens, 2010). High concentrations of NO in atmosphere also lead to an underestimation of HO_2/OH ratio (Dusanter, Vimal, & Stevens, 2010).

Another source of uncertainty are the reactions with VOCs and the primary organic aerosol (POA), which can lead to the formation of semi-volatile hydrocarbons in the urban environment (Sheehy, Volkamer, Molina, & Molina, 2010). These components are not included in our simulation both in GFDL and in LMDz.

All those uncertainties in the description of the urban environment lead to difficulties in the evaluation of the simulation based on the literature reports. The two studies used as a benchmark for the simulations are (Dusanter, Vimal, & Stevens, 2010) and (Sheehy, Volkamer, Molina, & Molina, 2010), which report a wide range of concentration profiles for both OH and HO_2; even between the same study, based on the day of the simulation. The ratios between the two components also differ significantly, ranging from 50 to over 100.

The complexity of the simulated environment does not allow for a complete characterization of the atmospheric conditions over a 24-hour period. Therefore, all simulations in the urban environment were extended to one month (30 days) or more. The number of days required for the system to reach stabilization varies between different configurations. The difficulty in achieving a stable simulation during the initial days is likely due to the presence of multiple steady states.

3.2.1. GFDL chemical scheme

The GFDL model is the same used for the marine environment (Horowitz, Naik, & Paulot, 2020), except for the marine reactions, that are removed from the simulation. No other reactions are added for the representation of the urban environment. The new conditions of the simulation are reported in the table 2-7.

3.2.1.1. Photochemical data from IUPAC

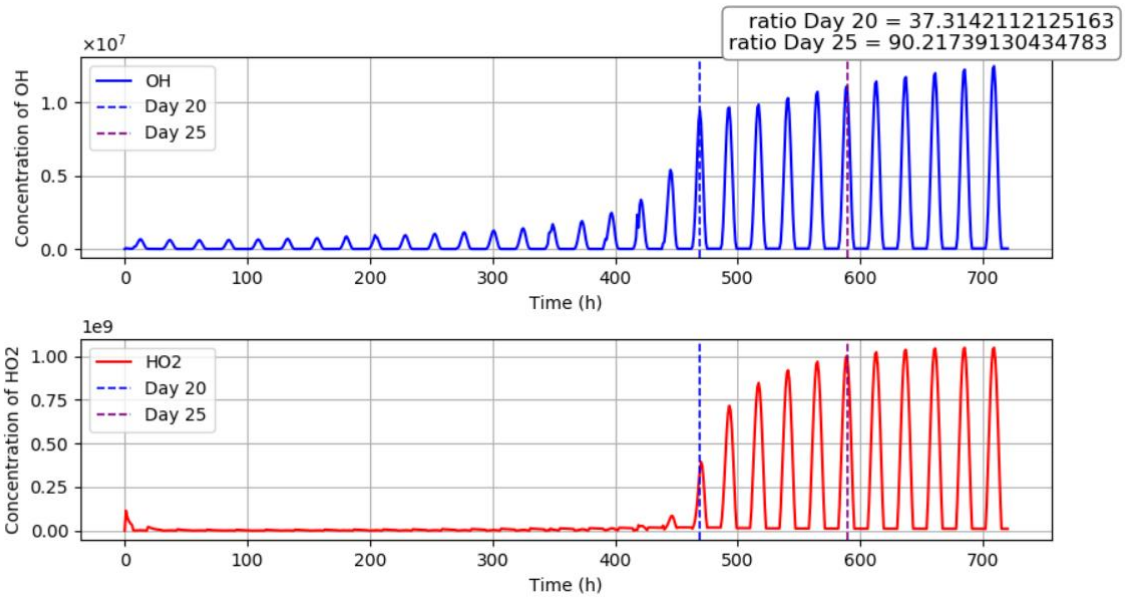

Figure 3.2.1.1: OH and HO_2 profile in urban environment with GFDL chemical model and photochemical data taken from IUPAC

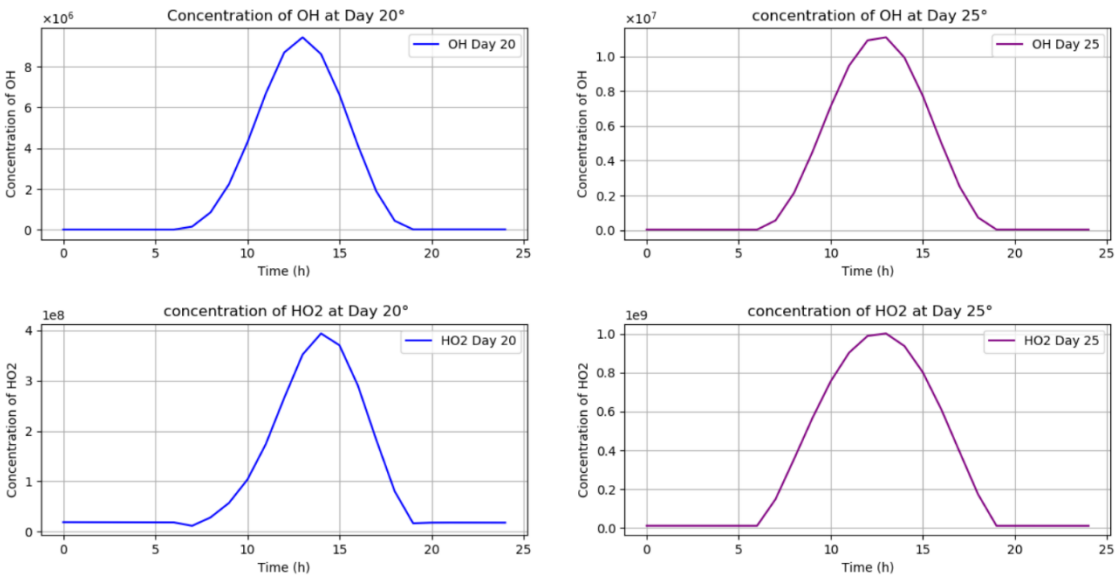

Figure 3.2.1.2: OH and HO_2 concentrations in the two days analyzed with photochemical data taken from IUPAC

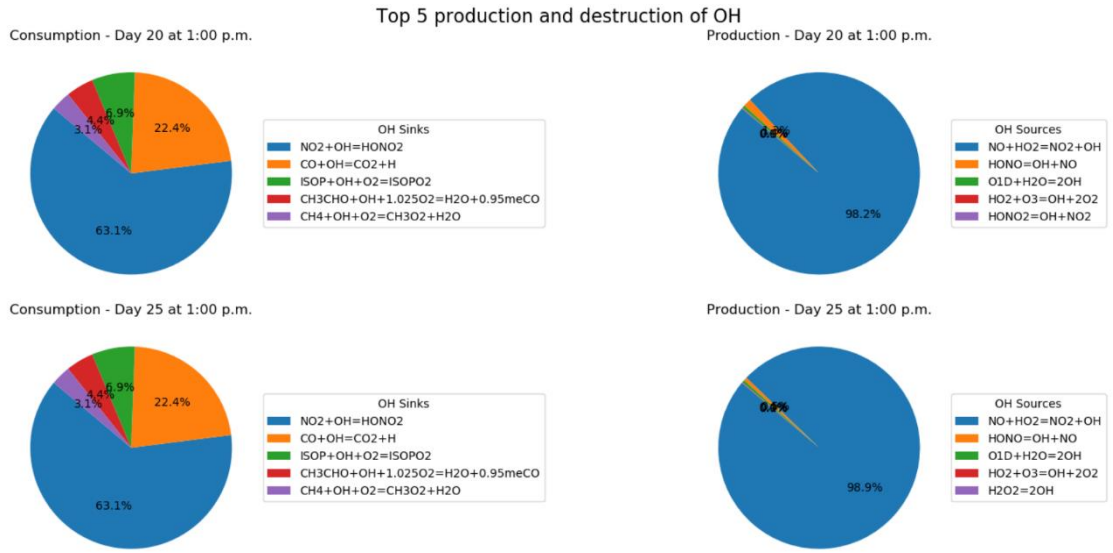

Figure 3.2.1.3: OH production and destruction rates for the two days considered with photochemical data taken from IUPAC

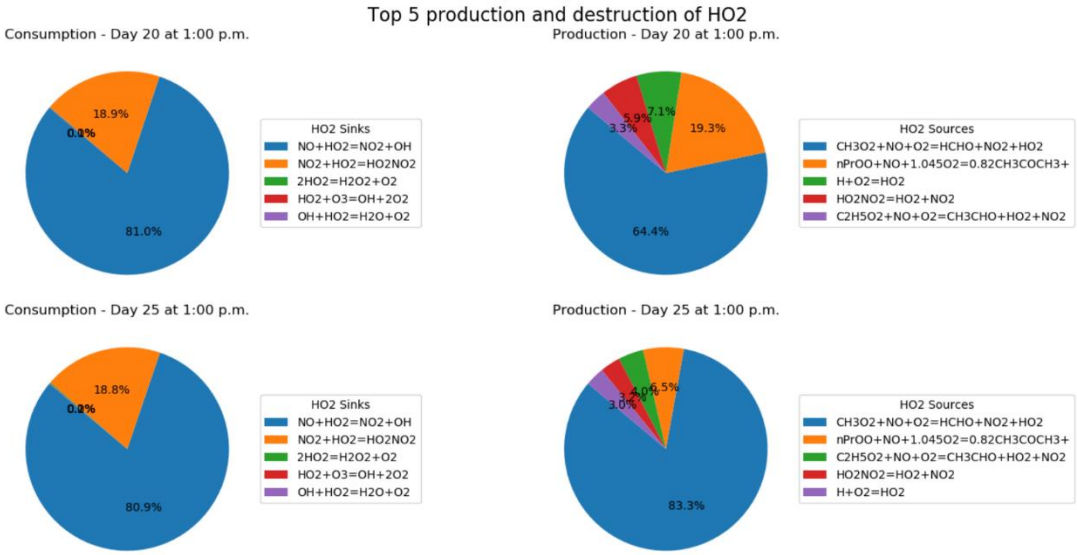

Figure 3.2.1.4: HO_2 production and consumption rates in the two days considered with photochemical data taken from IUPAC

The first results reported are obtained using the IUPAC photochemical data. The OH and the HO_2 concentrations are reported alongside their ratios on two different days chosen arbitrarily. The simulation required 20 days to stabilize and give a more constant profile.

As shown in Figure 3.2.1.4, the simulation maintains nearly constant values even when extended beyond 30 days.

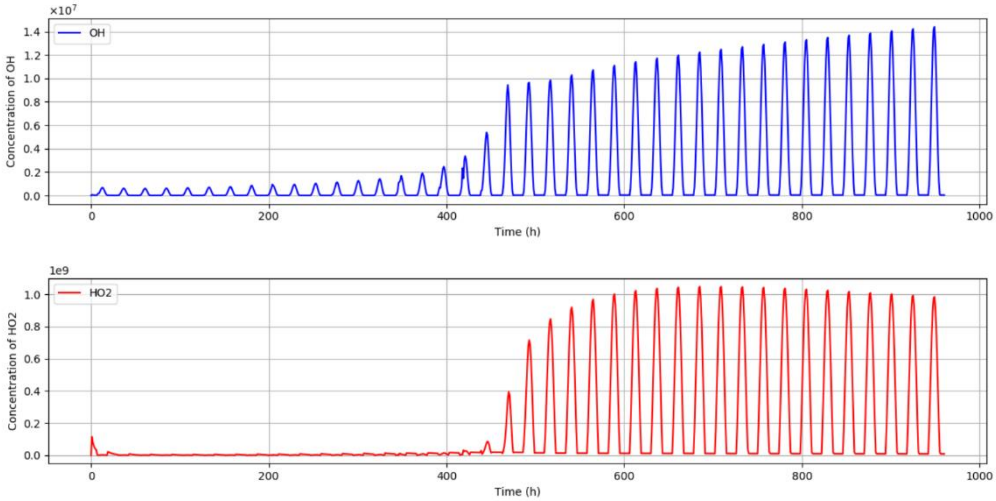

Figure 3.2.1.5: OH and HO_2 profile in urban environment with GFDL model and photochemical data taken from IUPAC in 40 days

The OH and HO_2 maximum concentrations are higher than those reported for the marine environment in the same configuration, especially in the case of HO_2, this is probably due to the much higher concentrations of NO and NO_2 in the polluted atmosphere.

The HO_2/OH ratio starts at 30 and reach a stable value around 90. This value is higher than the one reported by (Dusanter, Vimal, & Stevens, 2010), but in agreement with the one shown by (Sheehy, Volkamer, Molina, & Molina, 2010).

From the aerograms, it is easy to see that the reactions involving NO and NO_2 are the most important one in term of generation and destruction of both OH and HO_2. In fact, the reaction between NO and HO_2 is the only responsible for the generation of OH, and its destruction occurs via NO_2 for more than 60%; the reaction with CO (the Main sink factor in the marine environment) is now the second term, and weights for a third of the first one.

The same goes for HO_2: the reactions between CH_3O_2 and $C_3H_7O_2$ with NO are responsible for more than 80% of its formation, and the consumption is completely fulfil by NO and NO_2, that together remove 100% of the HO_2.

The data reported above clearly indicate that, with atmospheric concentrations of approximately 16 ppb for NO and 28 ppb for NO_2, the levels of both OH and HO_2 are strongly influenced by the presence of nitrogen oxides.

3.2.1.2. Photochemical data from MCM

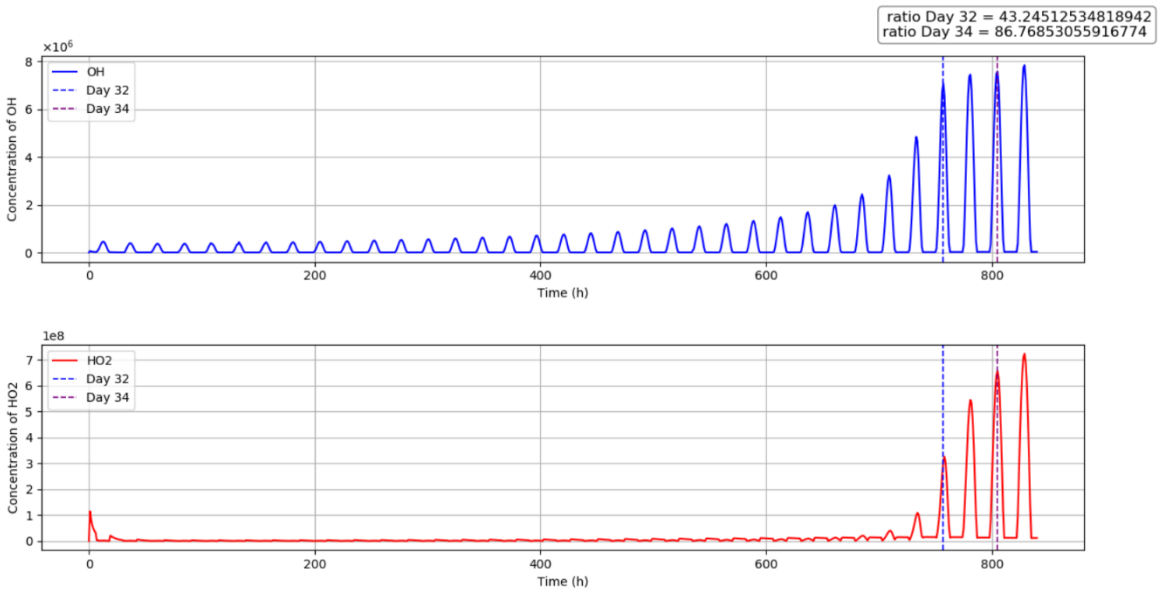

Figure 3.2.1.6: OH and HO_2 concentration profile in urban environment with GFDL model and photochemical rate constants taken from MCM

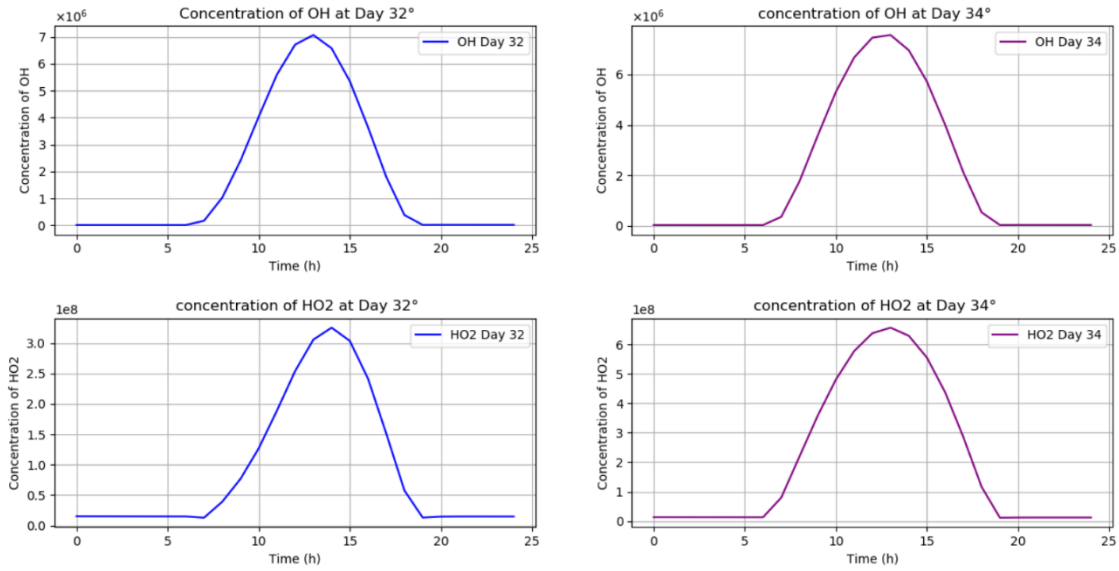

Figure 3.2.1.7: OH and HO_2 concentrations in the two days analyzed with photochemical data taken from MCM

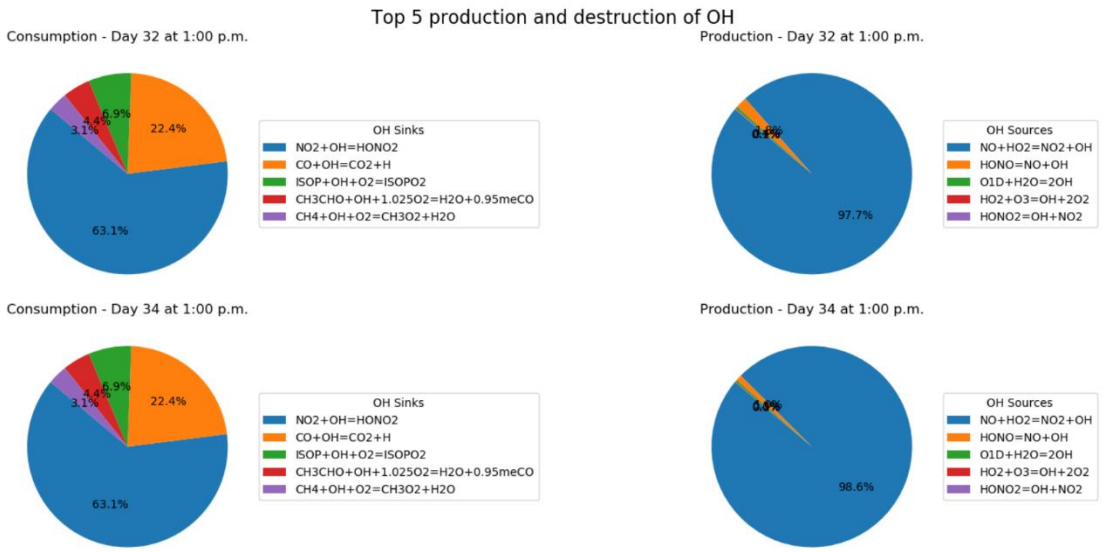

Figure 3.2.1.8: OH production and destruction rates for the two days considered with photochemical data taken from MCM

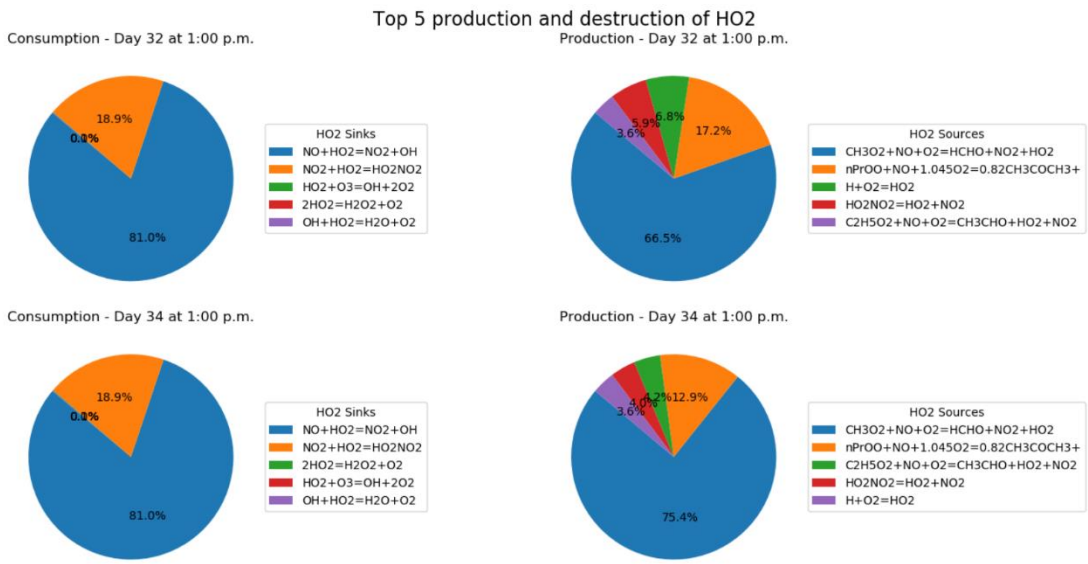

Figure 3.2.1.9: HO_2 production and consumption rates in the two days considered with photochemical data taken from MCM

In the second configuration, the OH and HO_2 concentrations are now slightly lower from the first one, this is probably due to the different values of the rate constants proposed by the MCM website. The ratio remains almost constant (decreasing slightly from 90 to 85), but the simulation requires more days to perform a stable result.

The most important reactions and their different contributes remain the same from the first configuration to the second.

3.2.1.3. Photochemical data from MCM with added reactions

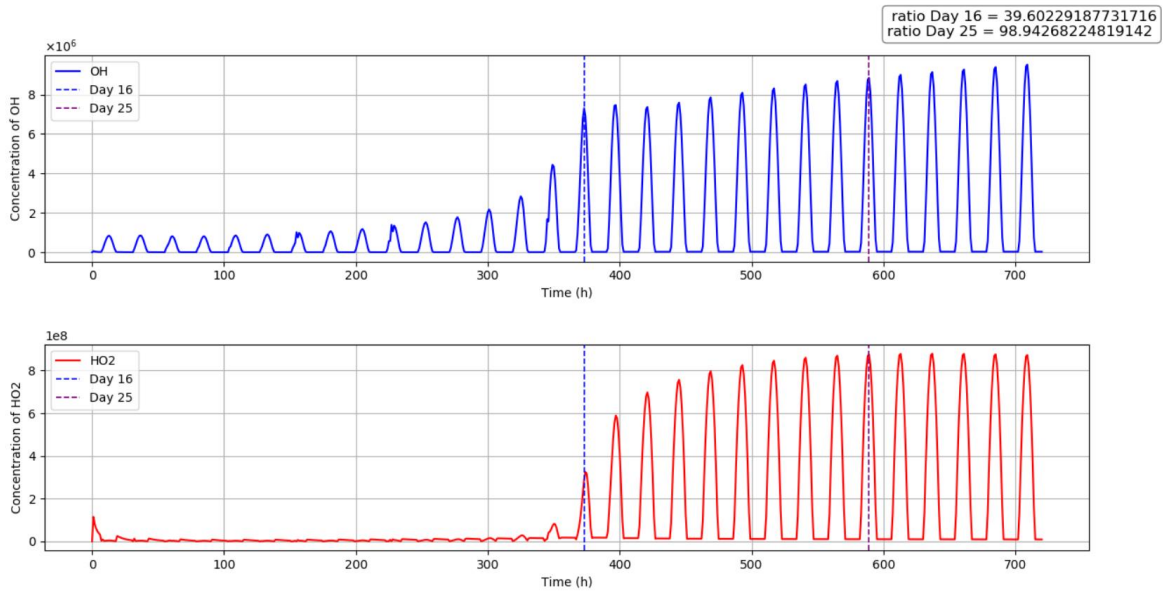

Figure 3.2.1.10: OH and HO_2 concentration profile in urban environment with GFDL model and photochemical data taken from MCM with added reactions

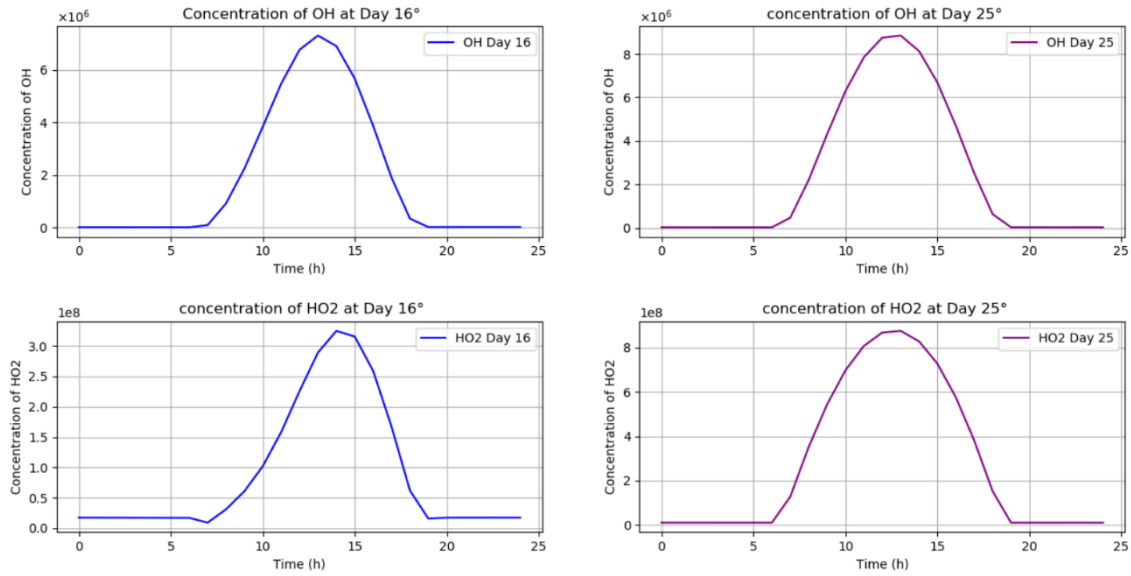

Figure 3.2.1.11: OH and HO_2 concentrations in the two days analyzed with photochemical data taken from MCM with added reactions

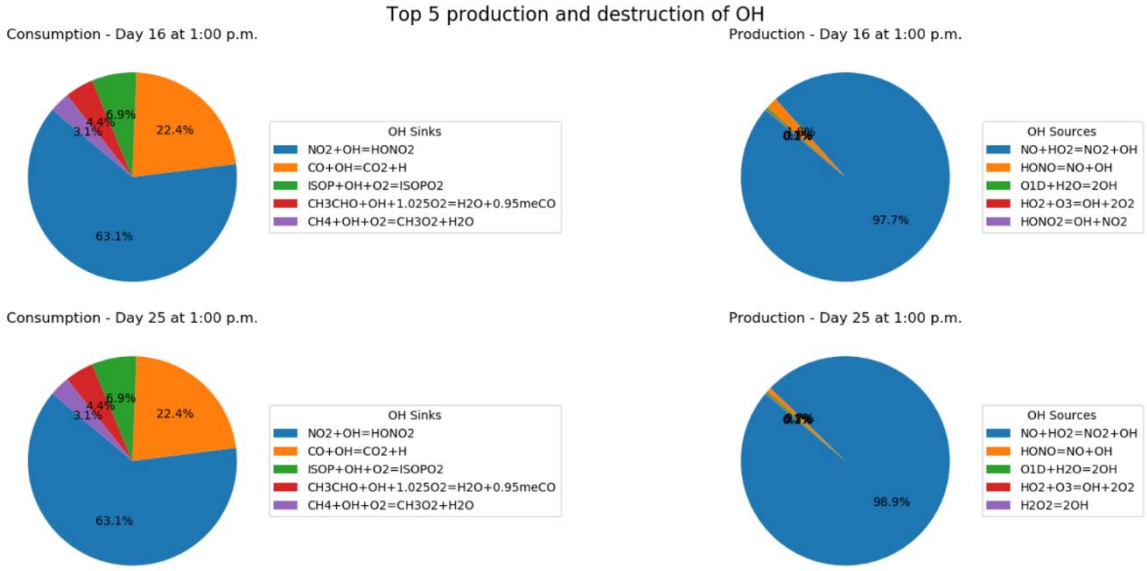

Figure 3.2.1.12: OH production and destruction rates for the two days considered with photochemical data taken from MCM with added reactions

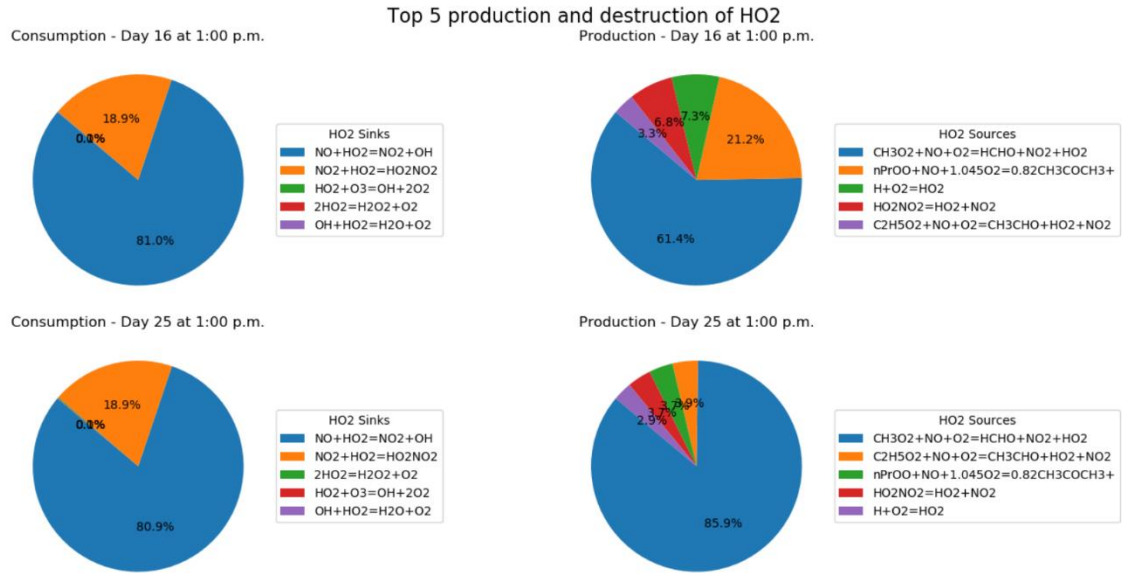

Figure 3.2.1.13: HO_2 production and consumption rates in the two days considered with photochemical data taken from MCM with added reactions

The third and final simulation can obtain a stable solution much more rapidly than the two previously reported.. The maximum levels of OH and HO_2 are similar to those shown in the second configuration but with a ratio between the two gases around 95.

The aerograms show that even in the last configuration, the main contribution for the atmospheric composition in the urban environment are the nitrogen oxides (NO and

NO_2); together are responsible for almost all the formation and destruction of the two gases considered. The main reactions and their impacts on the total production and consumption of OH and HO_2 remain the same across all the three different simulations.

Given the wide range of concentration profiles reported by (Dusanter, Vimal, & Stevens, 2010) for both OH and HO_2, it is not straightforward to identify the most appropriate profile for simulating urban environments. The last configuration is chosen, in continuity with the marine simulation, to perform the evaluation of the impact of the NO_X over the ratio between OH and HO_2 and the impact of the hydrogen incrementation.

3.2.1.4. Simulation with different values of NOx with GFDL mechanism

For this evaluation the simulation is performed at different concentrations (expressed as ppb) of NO and NO_2; the second one is fixed with the same ratio used in the standard conditions, so is always 70% higher than NO.

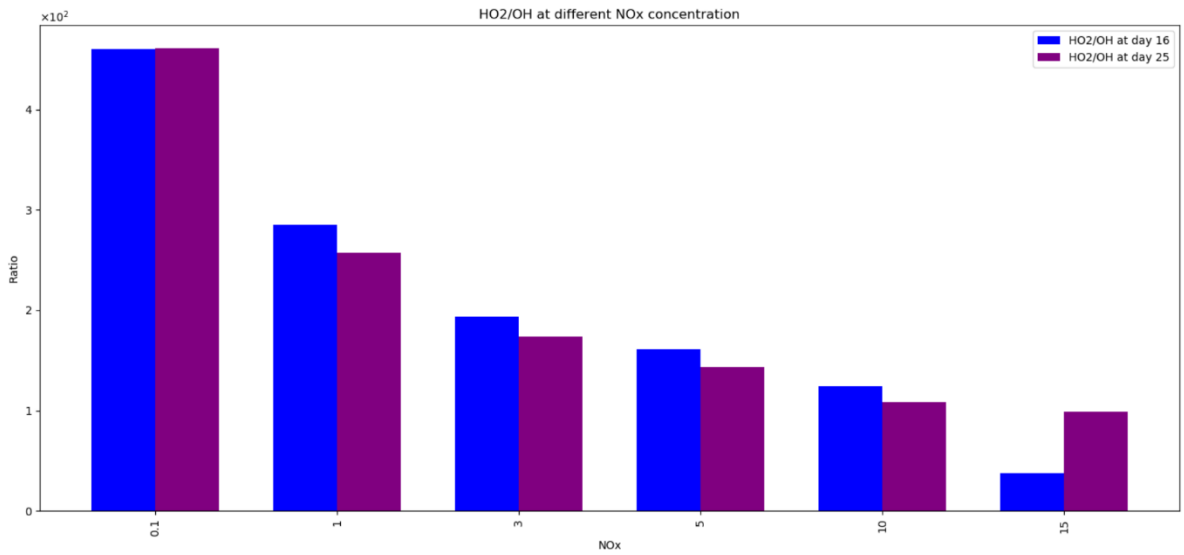

Figure 3.2.1.14: effect of the NOx concentration on the system stabilization and the HO_2/OH ratio

In the graph above, are reported the different ratios for the two days considered in the last simulation with different values of NO and NO_2 in urban environment. As reported by (Sheehy, Volkamer, Molina, & Molina, 2010), the ratio between the two molecules is much higher when the fraction of NOx is smaller and decreases with the increasing of it.

This effect is due to the NO + HO_2 reaction, which accounts for almost all the OH generated in the urban environment. When the NOx is low, the transformation from HO_2 to OH is reduced, this leads to a higher value of their ratio.

It can also be observed that at lower NOx levels, the system reaches stability much more quickly. As shown in Figure 3.2.1.14, when NOx fraction does not exceed 10 ppb, the HO_2/OH ratios on the two selected days are comparable; however, when it reaches 15 ppb, the ratio on the first day is lower than on the second, because the system has not yet stabilized. This is an extra confirm of the difficulty of the simulation of polluted atmosphere, where reactions that are almost negligible in the marine environment become central to the system characterization. The main molecules involved in the formation and destruction cycles of OH and HO_2 in the marine environment are O^1D, CO, and RO_2. In contrast, in urban environments, the lifetimes of OH and HO_2 are almost entirely governed by nitrogen oxides.

3.2.1.5. Impact of H_2 increase on atmospheric reactivity

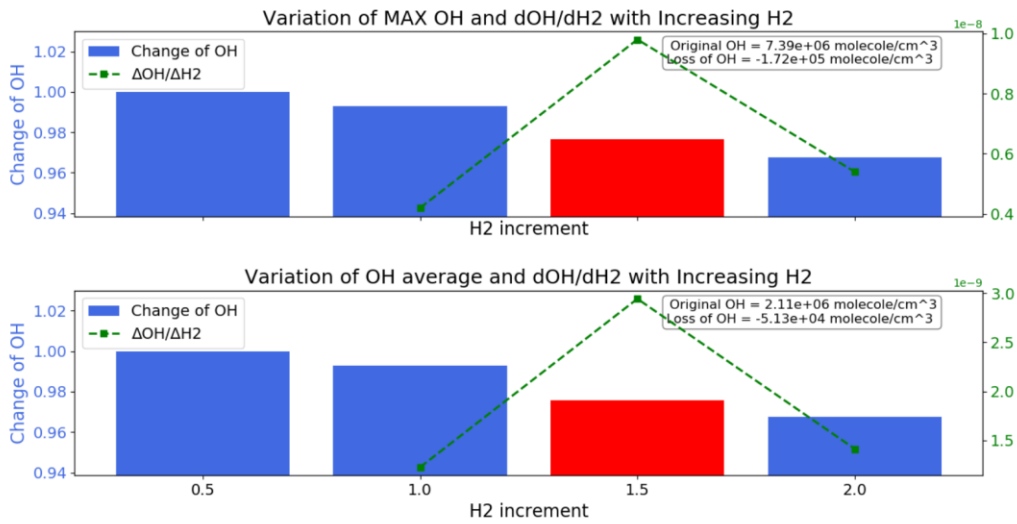

Figure 3.2.1.15: Effect of increasing H_2 on both the maximum and the average OH with GFDL chemical scheme. The total loss of OH is between the initial value and the one with 1.5ppm of hydrogen in atmosphere.

The variation of OH due to the increase of H_2 in the atmosphere is shown in graph 3.2.1.15. The loss of OH is smaller than that reported in the marine environment, with a loss around 1.72 x 10^5 molecules/cm^3 for the maximum value, and 5.13 x 10^4 molecules/cm^3 for the average value. These results here are much closer to those

reported by (Warwick & Griffiths, 2022), that report a loss of OH at 1.5 ppb of H_2 around 0.9 x 10^5 molecules/cm^3.

The lower OH losses observed in the urban environment compared to the marine environment are likely due to the smaller contribution of the CH_4 + OH reaction to the overall OH consumption. As shown in Figure 3.2.1.12, this reaction accounts for approximately 3.4% of the total OH destruction in the urban environment, whereas in the marine environment it contributes more than 22%.

	Loss of OH [molecules/cm^3]	new CH_4 [molecules/cm^3]	dOH/dH_2	a	GWP [100]
Max OH	1.72E+5	2757.3	1.86E-8	0.211	54.75
Average OH	5.13E+4	2757.3	5.22E-9	0.0592	15.39

Table 3-3: parameters for the evaluation of the GWP of H_2 derived from both maximum and average value of OH.

Table 3-3 show that the GWP of H_2 in the urban environment is significantly lower than that observed in the marine environment. The limited contribution of the H_2 + OH reaction, much lower compared to the reaction between OH and NO_x, reduces the impact of increased atmospheric hydrogen. Nonetheless, it is important to note that the urban environment is almost negligible in terms of the total atmospheric gas mass on Earth.

3.2.2. LMDz chemical scheme

The LMDz model is the same used for the marine environment (Folberth, Hauglustaine, Lathière, & Brocheton, 2006), except for the marine reactions, that are removed from the simulation. No other reactions are added for the representation of the urban environment. The simulation conditions are reported in the table 2-7.

3.2.2.1. Photochemical from IUPAC

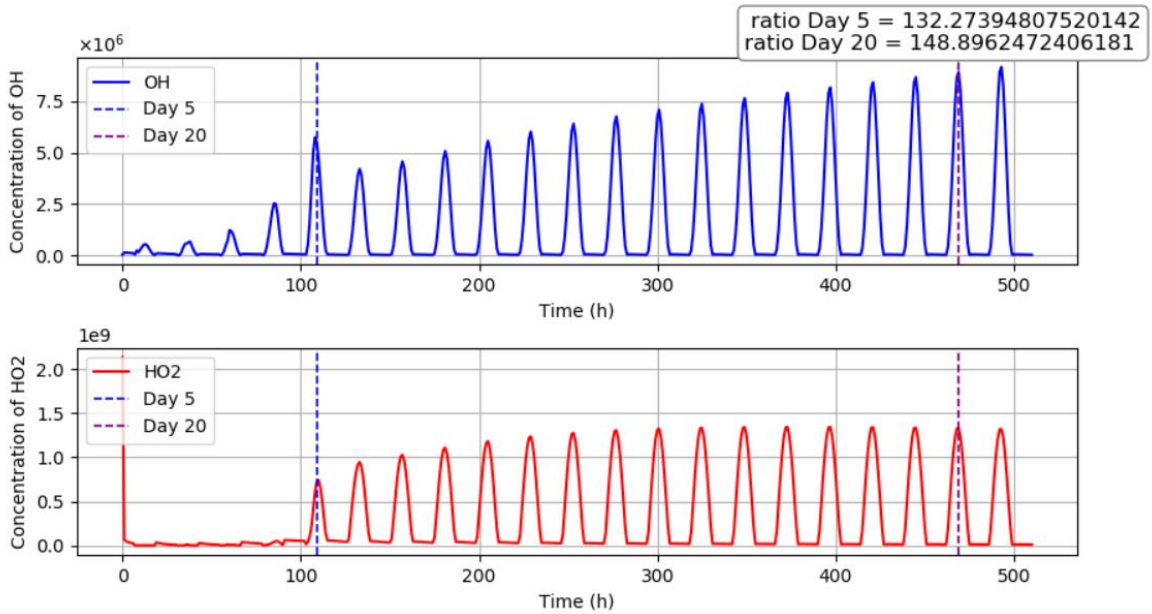

Figure 3.2.2.1: OH and HO_2 concentration profile in urban environment with LMDz model and photochemical data taken from IUPAC

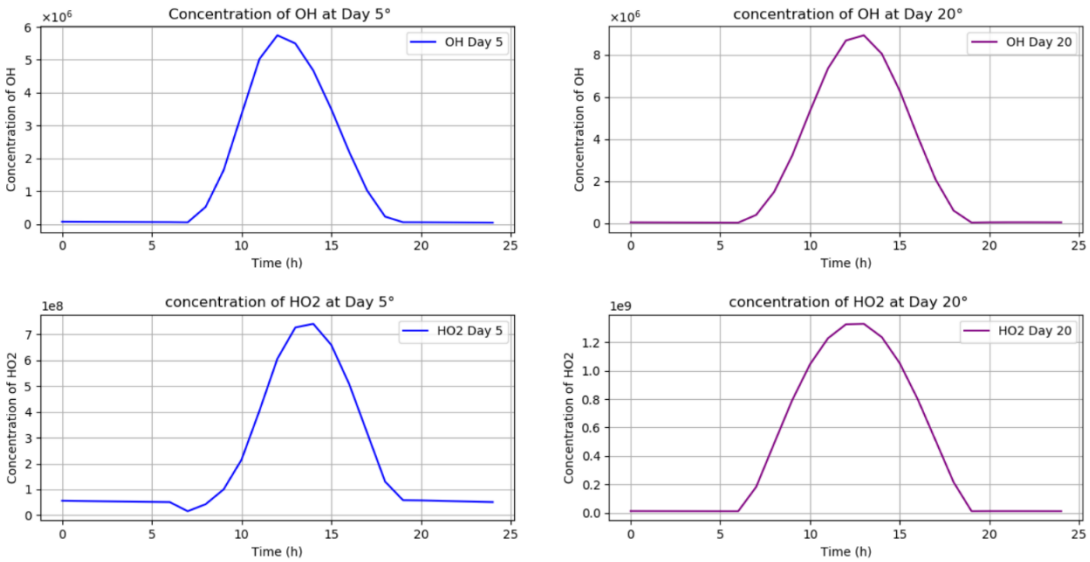

Figure 3.2.2.2: OH and HO_2 concentrations in the two days analyzed with photochemical data taken from IUPAC

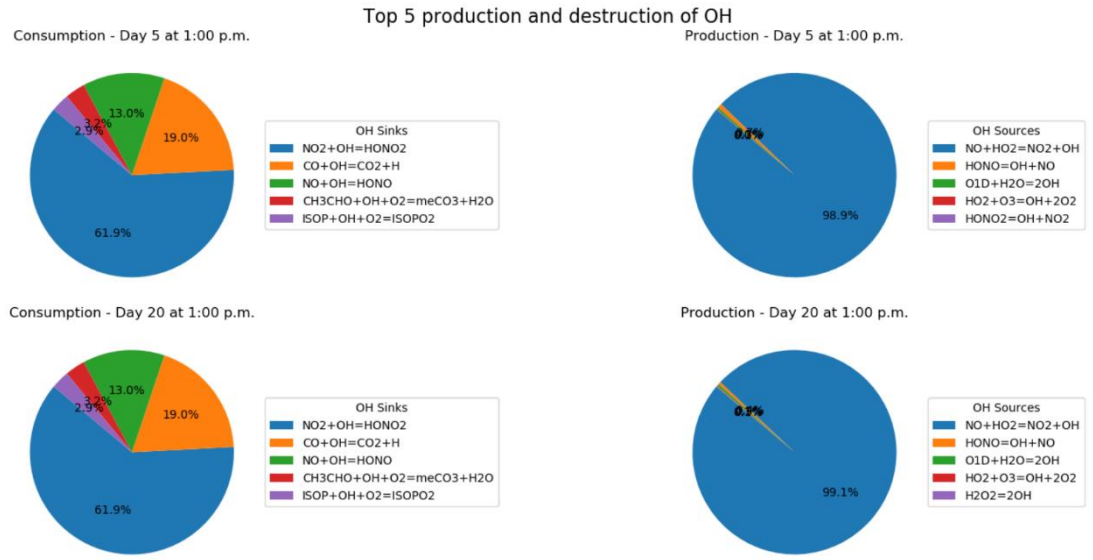

Figure 3.2.2.3: OH production and destruction rates for the two days considered with photochemical data taken from IUPAC

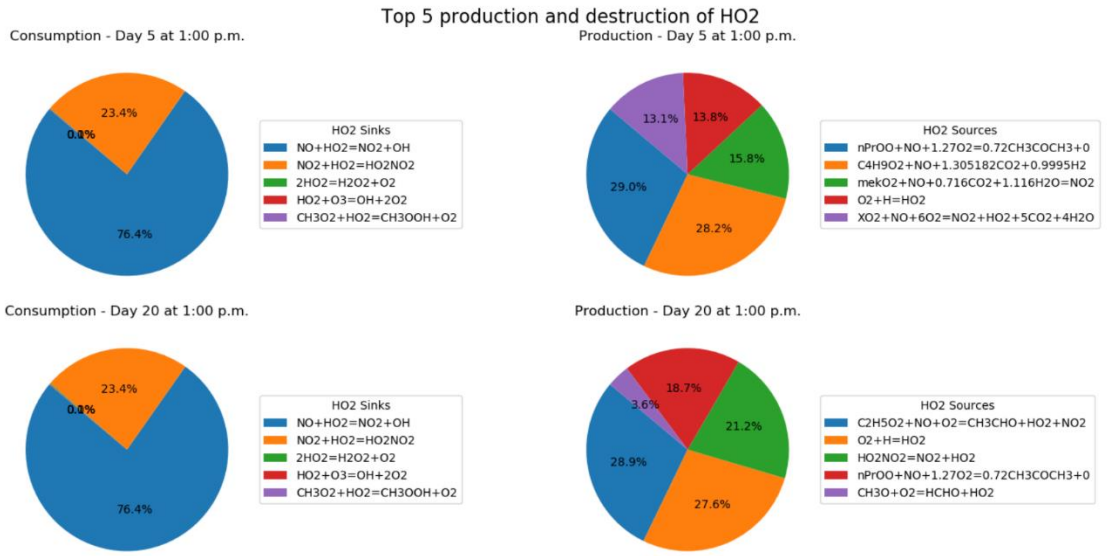

Figure 3.2.2.4: HO_2 production and destruction rates for the two days considered with photochemical data taken from IUPAC

The results obtained from the first simulation performed with the LMDz chemical scheme in urban environments are reported in this section. Also in the case of the urban environment, the HO_2 values are slightly higher than the one obtained with the GFDL chemical scheme in the same configuration. The reason is probably again the

difference contribution of the CO + OH and the HO_2 + HO_2 reactions, as already expressed in the marine scenario.

The consequence of those different kinetic structures is the higher HO_2/OH ratio, which is significantly higher than the one reported in the marine simulation by more than 40%.

The simulation now requires less time to reach a stable profile; only a few days are needed.

The reactions that play a critical role in the formation and destruction of OH are the same in the urban and in the marine environment. The reaction between the HO_2 and NO is by far the main source OH. The same goes for the consumption OH; more than 60% of it is eliminated by NO_2.

The consumption of HO_2 is again completely characterized by NO and NO_2, instead is formation consider a different pathway that involve heavier fraction of peroxide radical, like the one derived from propane and butane.

3.2.2.2. Photochemical data from MCM

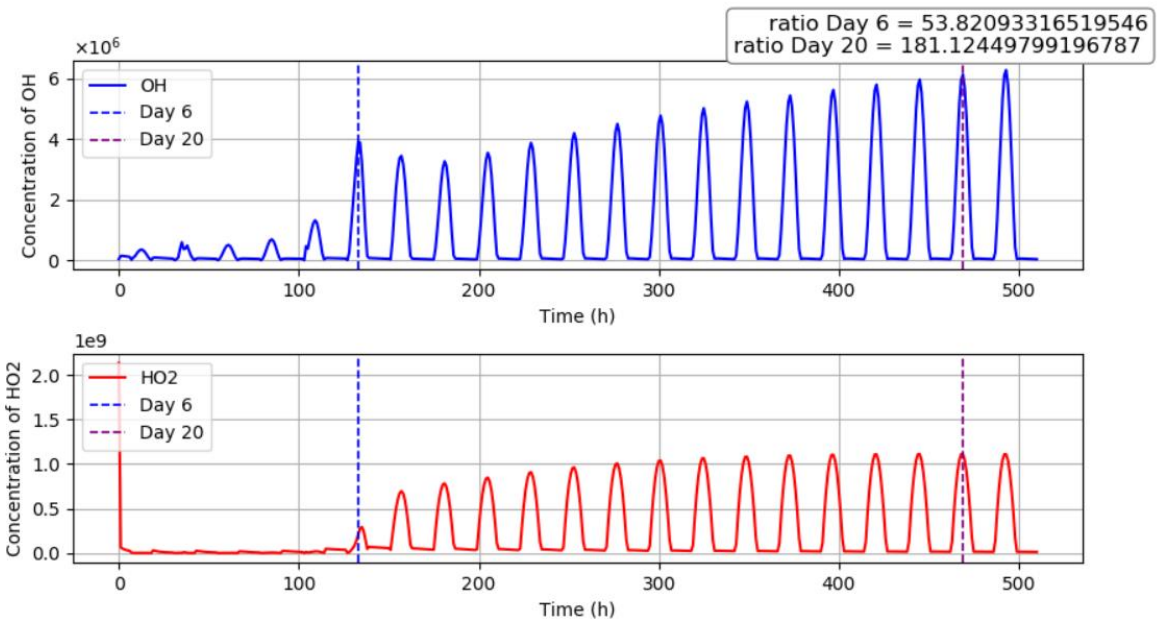

Figure 3.2.2.5: OH and HO_2 concentration profile in urban environment with LMDz model and photochemical data taken from MCM

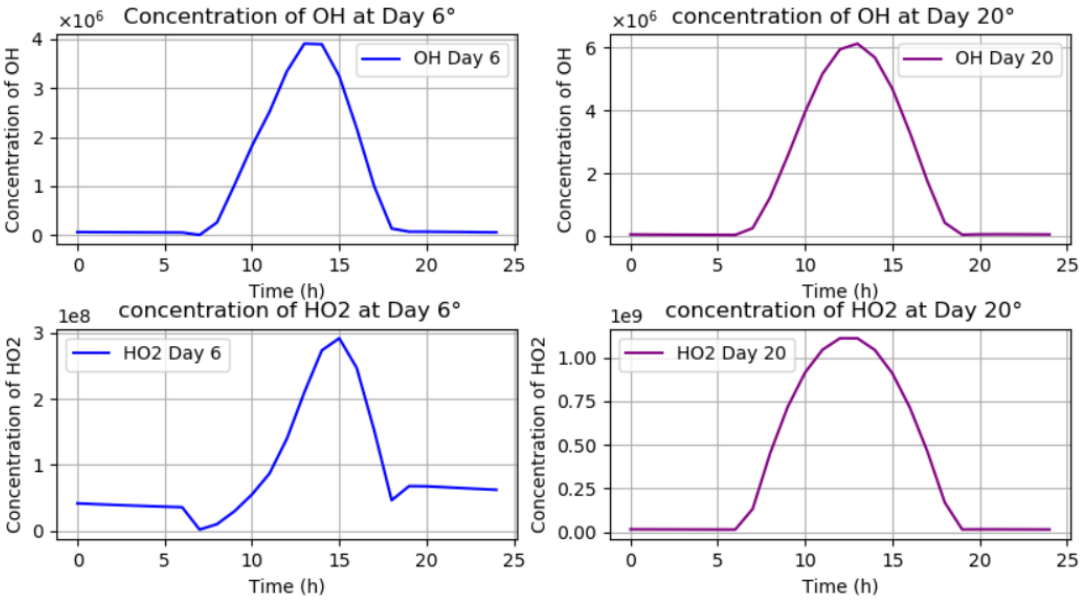

Figure 3.2.2.6: OH and HO_2 concentrations in the two days analyzed with photochemical data taken from MCM with added reactions.

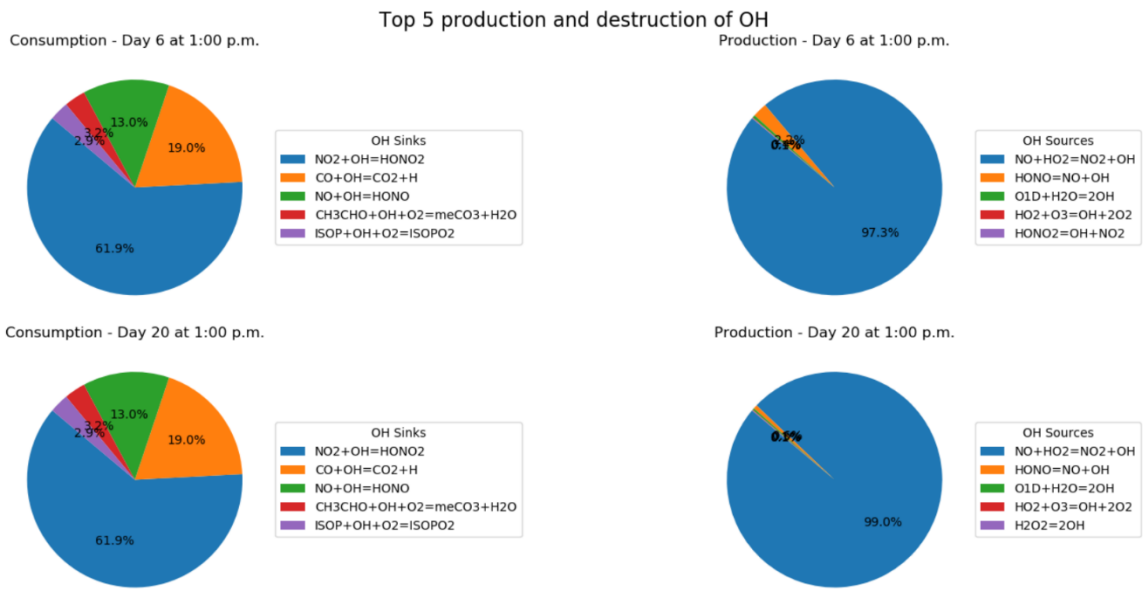

Figure 3.2.2.7: OH production and destruction rates for the two days considered with photochemical data taken from MCM

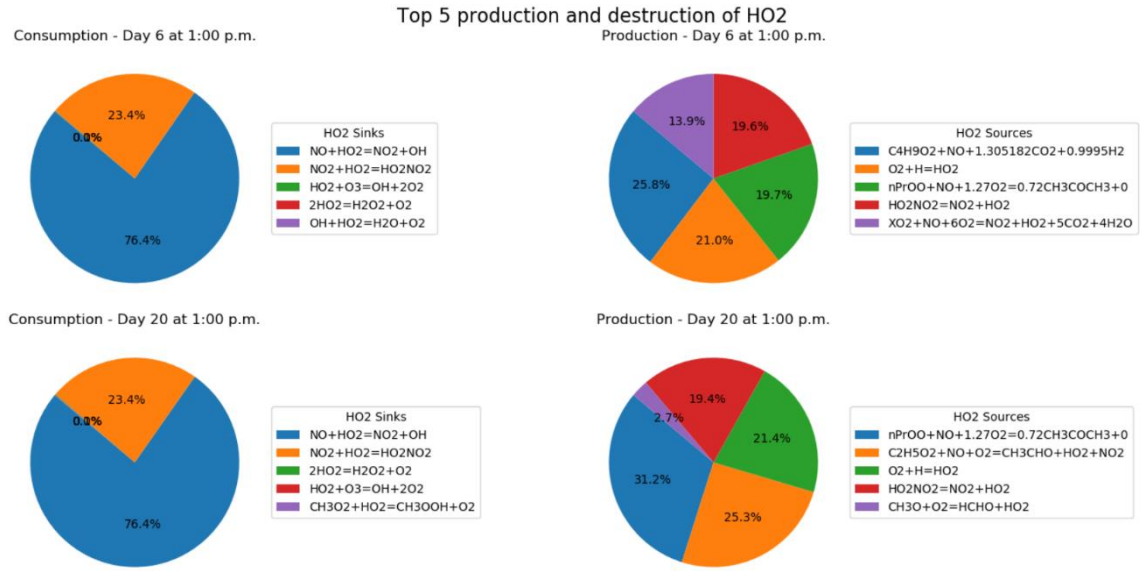

Figure 3.2.2.8: HO_2 production and destruction rates for the two days considered with photochemical data taken from MCM with added reactions

The second configuration used led to a simulation in which both OH and HO_2 are diminished. As for the GFDL urban simulation, this effect is due to the lower value of the rate constants of the photochemical reactions obtained from the MCM website. Between the two molecules OH is the one that diminishes the most, and so, the ratio in this second configuration is higher respect to the one shown in the first one. The number of days necessary to obtain a stable simulation has not changed.

The contributions of the reactions to the production and consumption of both OH and HO_2 has not changed either; NO and NO_2 remain the most important species in the lifecycle of the two target molecules.

3.2.2.3. Photochemical data from MCM with added reactions

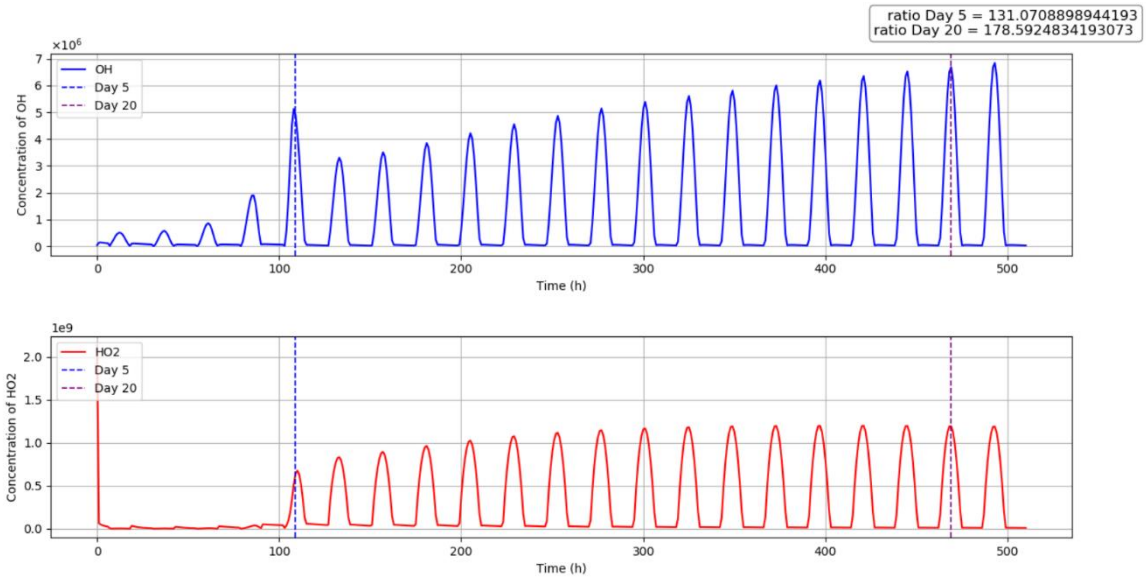

Figure 3.2.2.9: OH and HO_2 concentration profile in urban environment with LMDz model and photochemical data taken from MCM with added reactions

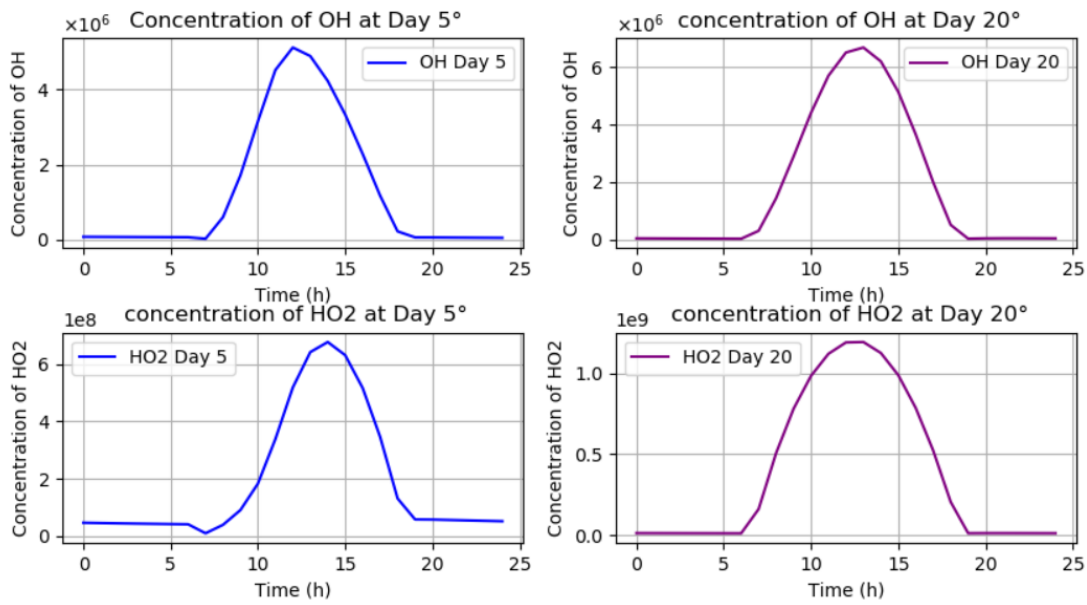

Figure 3.2.2.10: OH and HO_2 concentrations in the two days analyzed with photochemical data taken from MCM with added reactions.

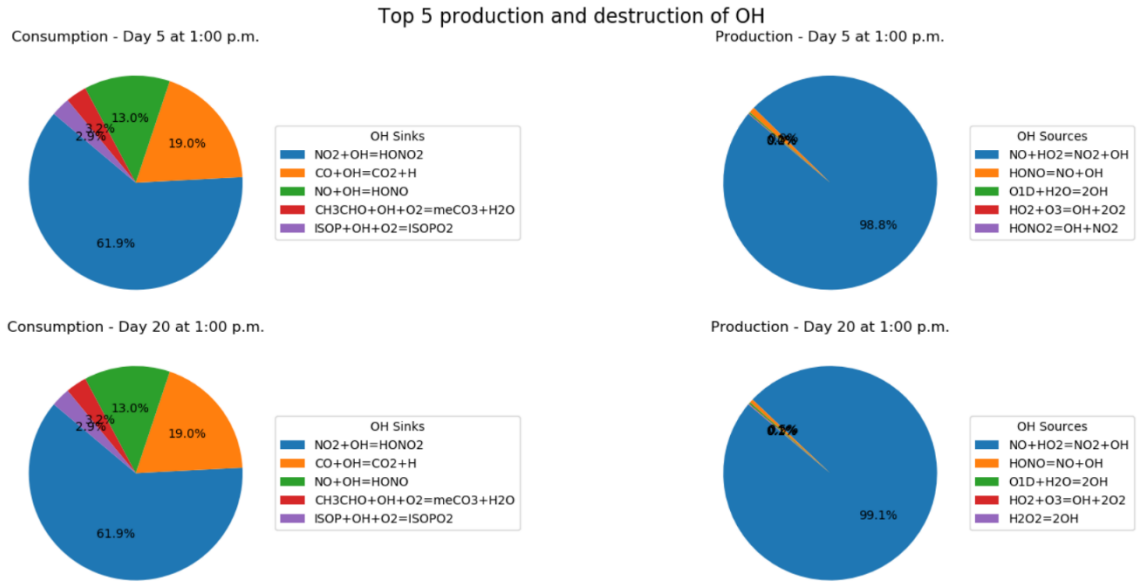

Figure 3.2.2.11: OH production and destruction rates for the two days considered with photochemical data taken from MCM with added reactions

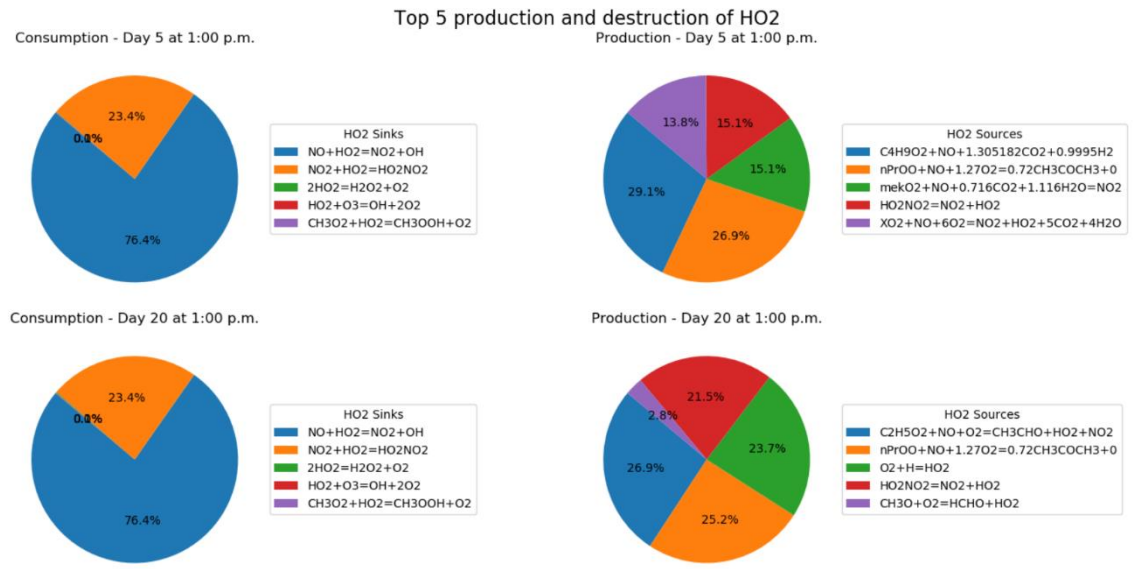

Figure 3.2.2.12: HO_2 production and destruction rates for the two days considered with photochemical data taken from MCM with added reactions

The new results obtained in this simulation are like those in the previous configuration. The HO_2/OH ratio is again higher than the one presented in paragraph 3.2.2.1 and in the GFDL chemical scheme.

The difference between the two models is probably due to the difficulty of characterizing of the chemistry among all the compounds present in a polluted

atmosphere such as the urban one. Each model decides which reaction to include and which to exclude from the simulation, this leads to a huge range of possible results.

Even so, each simulation confirms the major role played by nitrogen oxide in the polluted environment.

3.2.2.4. Simulation with different values of NOx with LMDz mechanism

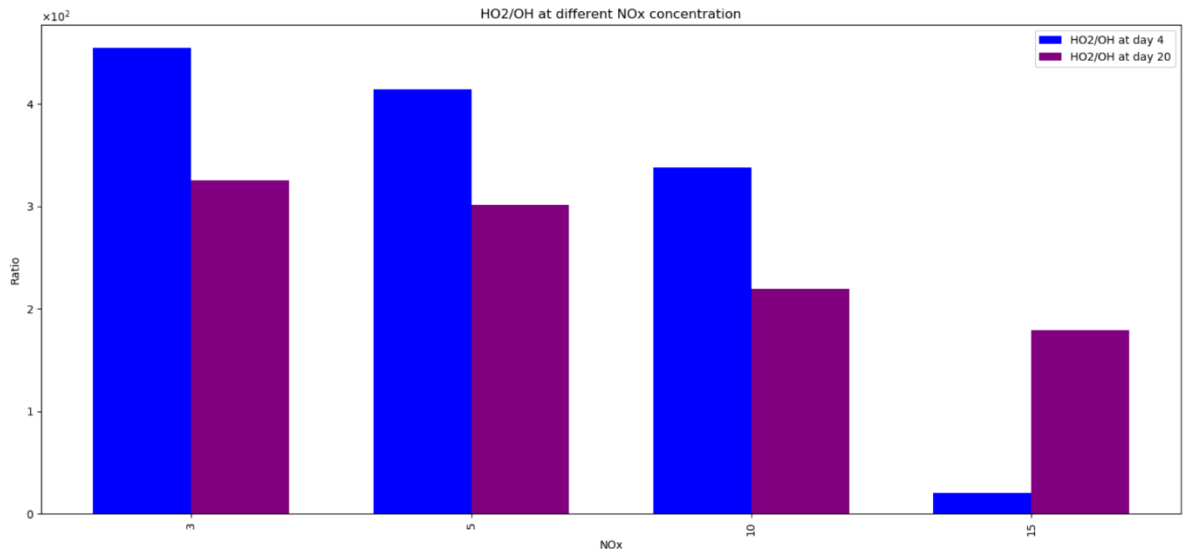

Figure 3.2.2.13: effect of the NOx concentration on the system stabilization and the HO_2/OH ratio

For this evaluation the simulation is performed at different concentrations (expressed in ppb) of NO and NO_2; the second one is fixed at the same ratio used in the standard conditions, so it is always 70% higher than NO.

The results are consistent with those reported using the GFDL chemical scheme. The HO_2/OH ratio increases with higher concentrations of NO and NO_2. Moreover, the simulation reaches stability more quickly at low NO_x levels: by day 4, the HO_2 concentration becomes comparable to that of the following days. In contrast, high NO_x concentrations result in unrealistic values and delayed stabilization.

3.2.2.5. Impact of H_2 increase on atmospheric reactivity

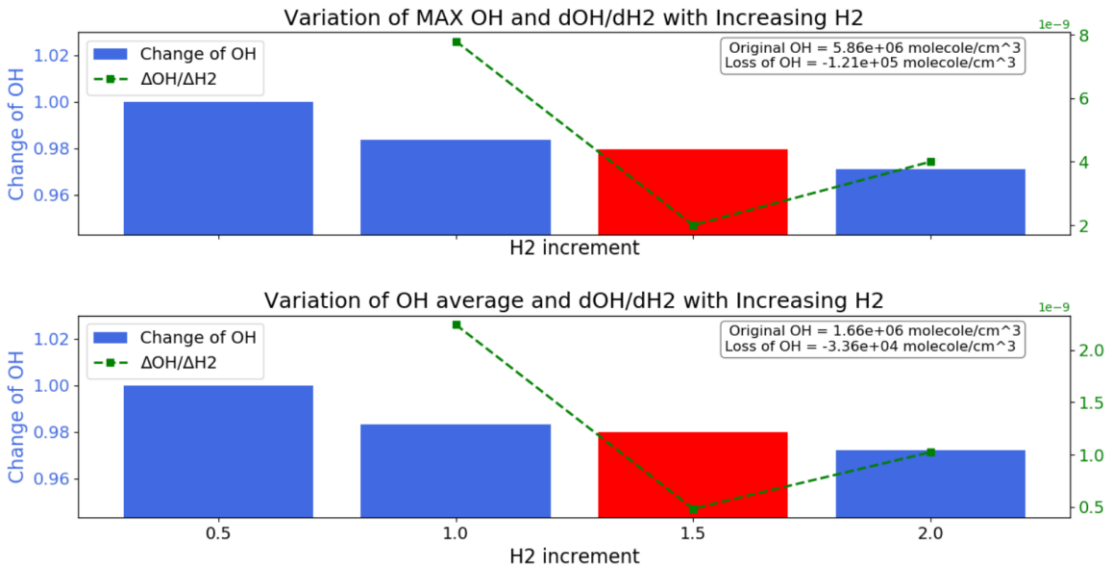

Figure 3.2.2.14: Effect of increasing H_2 on both the maximum and the average OH with LMDz chemical scheme. The total loss of OH is between the initial value and the one with 1.5 ppm of hydrogen in atmosphere.

The results obtained by incrementing the hydrogen concentration are shown in graphs 3.2.2.14, both for the maximum and average levels of OH. The pattern is the same as that obtained with the previous model and environment: the OH decrease with the increase of H_2 in the atmosphere. With a H_2 fraction of approximately 1.5 ppb (three times the standard level), the maximum OH concentration decreases by 1.21×10^5 molecules/cm³, while the average concentration decreases by 3.36×10^4 molecules/cm³.

	Loss of OH [molecules/cm³]	new CH_4 [molecules/cm³]	dOH/dH_2	a	GWP [100]
Max OH	1.21E+4	2757.3	9.30E-9	0.105	27.24
Average OH	3.36E+4	2757.3	2.61E-9	0.0296	7.68

Table 3-4: parameters for the evaluation of the GWP of H_2 derived from both maximum and average value of OH.

The table 3-4 confirms that in the urban environment the destruction of OH via H_2 is significantly lower than the ore reported in marine environment.

3.3. Stratospheric Environment

The last group of simulations proposed aims to characterize the influence of hydrogen in the stratospheric layer of the atmosphere. The three altitudes considered are at 15, 25 and 40 kilometres. The first one is chosen to emulate the lowest layer of the stratosphere, where the temperature is at its minimum value; the second one is an intermediate layer in which the ozone concentration is at its maximum level, and the last one emulates the top layer of the stratosphere. The initial conditions and the operative conditions are reported in 2.1 and 2.2 paragraphs.

The stratospheric simulation is performed only for the GFDL chemical scheme, since its set of reactions can simulate both the tropospheric and stratospheric environment, the LMDz chemical scheme, instead, requires a different range of reactions for different layers of the atmosphere. The kinetic parameters used for the simulation are the one obtained by MCM with the added reactions described in paragraph 2.1.5.1.

The data used as a benchmark for the simulations are taken by (Penn state university, s.d.), (Chance, Stachnik, & Salawitch, 1996) and from (Jucks, Margitan, & Sasano, 1998), the last one is more focused on the higher layer of the stratosphere.

3.3.1. Stratospheric atmosphere at 15 Kilometres.

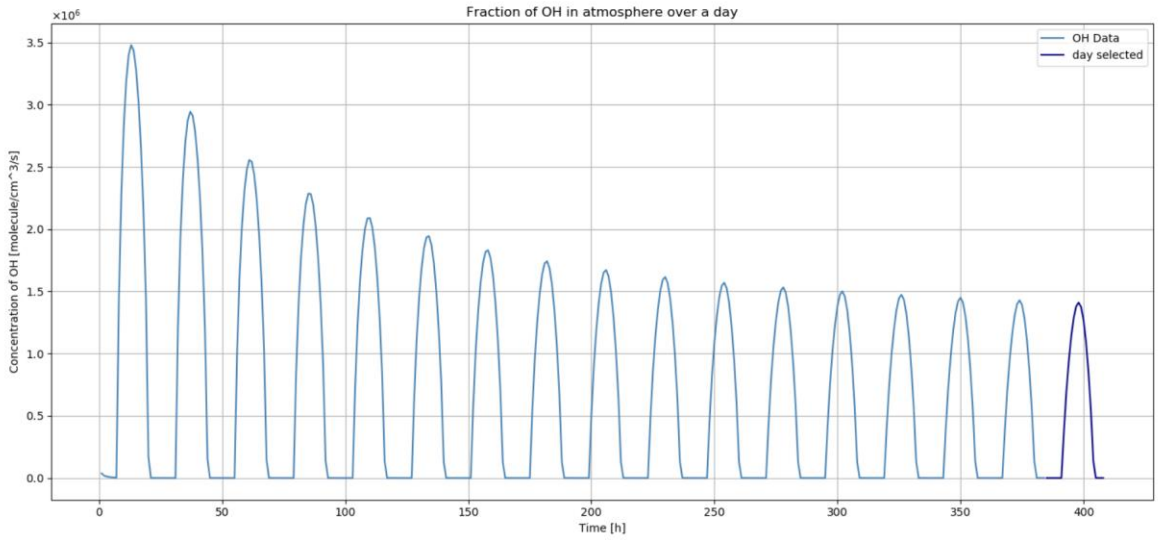

Figure 3.3.1.1: OH profile with GFDL chemical scheme at 15 kilometers.

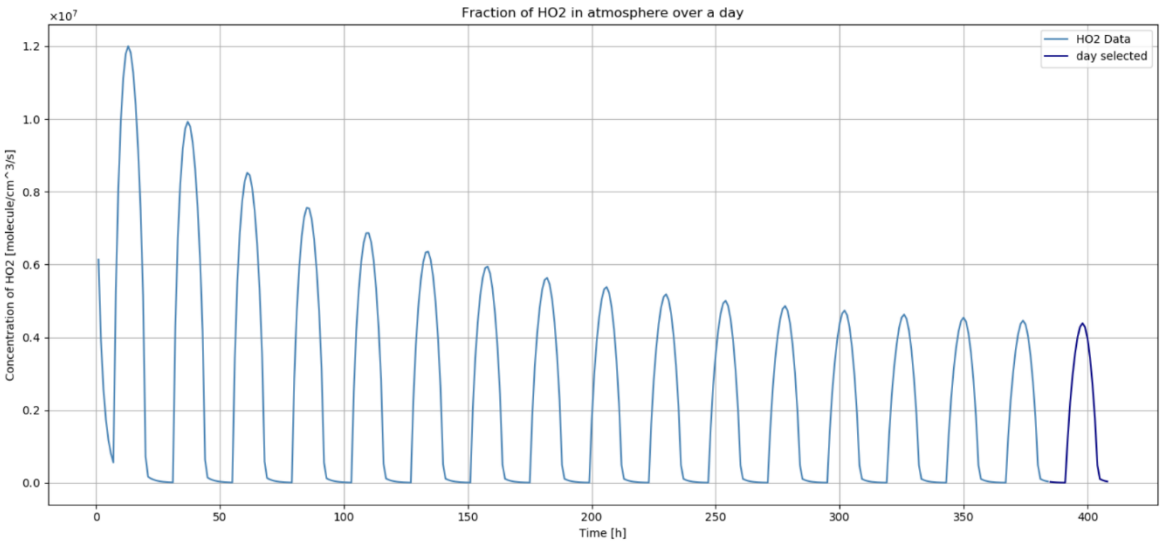

Figure 3.3.1.2: HO_2 profile with GFDL chemical scheme at 15 kilometers

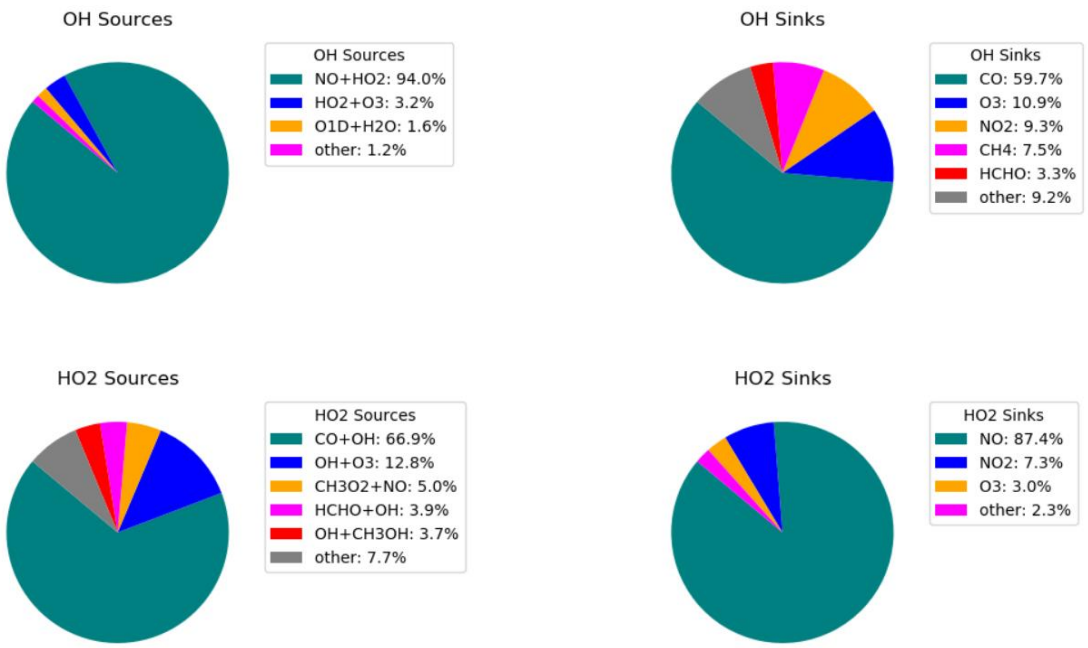

Figure 3.3.1.3: aerograms of the most important reaction contribution for the formation and destruction of OH and HO_2 at 1:00 p.m. with the GFDL chemical scheme at 15 kilometers

As in the case of the urban simulation, the system require several days to reach a stable solution. During the first five days, the concentrations of OH and HO_2 decrease rapidly and then remain nearly constant. This behaviour is due to the presence of multiple stationary states: until the system settles into a more stable steady state, the values vary

significantly from one day to the next. The last day is highlighted in a different colour because it was selected for the evaluation of the rates shown in Figure 3.3.1.3 and for the assessment of the impact of H_2 increase in the stratosphere, presented in Figure 3.3.1.4.

The OH concentration profile shown in the graph does not differ too much compared to the one reported at ground level. The concentration is diminished, but the fraction of OH in the atmosphere is slightly increased, since the molecular density decreases from the ground level (around 4.036×10^{-5} molecules/cm^3) to 15 kilometres (6.624×10^{-6} molecules/cm^3)

In contrast, the HO_2 profile is significantly reduced, as both its concentration and its atmospheric fraction are lower than those observed at ground level. This is due to the more pronounced effect that NO_x has in the stratosphere compared to the troposphere, at least in marine environments (used for comparison since it is the most relevant in terms of mass).

By knowing the concentrations of both OH and HO_2, as well as the molecular density in the troposphere and stratosphere, it is possible to calculate the atmospheric fraction of these gases. As shown in Table 3-6, the fraction at 15 kilometres is higher than at ground level.

NO and NO_2 play again a huge role in the lifetime of the two species, but not as much as in the urban environment. The reaction between NO_2 and HO_2 is the major source of generation of OH and the biggest sink for HO_2. OH is consumed by CO and O_3 for almost 70%, which are again the biggest sources of HO_2.

It is already possible to see the increased contribution of O_3 in the lower level of the stratosphere.

3.3.1.1. Impact of H_2 increase on atmospheric reactivity at 15 Km

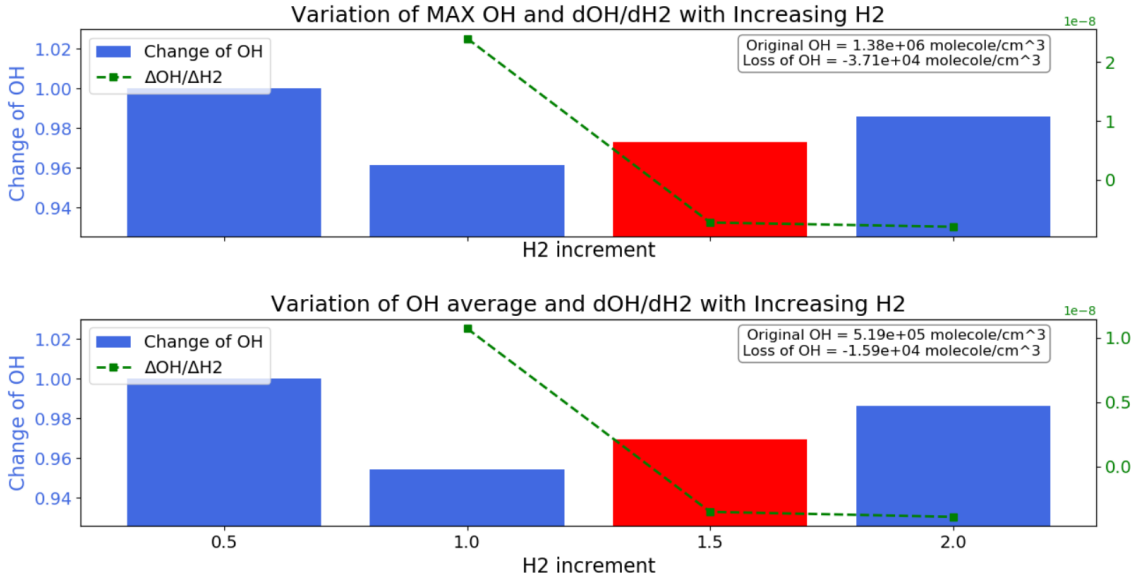

Figure 3.3.1.4: Effect of increasing H_2 on both the maximum and the average OH at 15 Km. The total loss of OH is between the initial value and the one with 1.5ppm of hydrogen in atmosphere.

In the figure 3.3.1.4 are reported the results of the effect of hydrogen incrementation in the first layer of the stratosphere analyzed. At this altitude, the increase of H_2 still reduces the concentration of OH, but its impact is inferior respect to those seen in the troposphere. This effect is probably due to the minor relevance of the H_2 + OH reaction. In the table 3-5 is shown the amount of OH that is eliminate from an atmosphere enrich with H_2. Respect to the maximum value reported in the figure 3.3.1.1 in the last day is clear that OH losses about 5% of its value.

The effect of increasing H_2 at 15 km altitude is no longer a linear decrease, as observed at ground level. This behaviour is further explained in paragraph 3.3.2.1. Nevertheless, it remains clear that a tripling of atmospheric H_2 still leads to a decrease in OH concentration.

	Loss of OH [molecules/cm³]	new CH_4 [molecules/cm³]	dOH/dH_2	a	GWP [100]
Max OH	2.29E+5	2062	1.71E-8	0.1453	37.70
Average OH	9.81E+4	2062	7.68E-9	0.0651	16.89

Table 3-5: parameters for the evaluation of the GWP of H_2 derived from both maximum and average value of OH in an atmosphere with 1.5 ppm of H_2.

3.3.2. Stratospheric atmosphere at 25 Km.

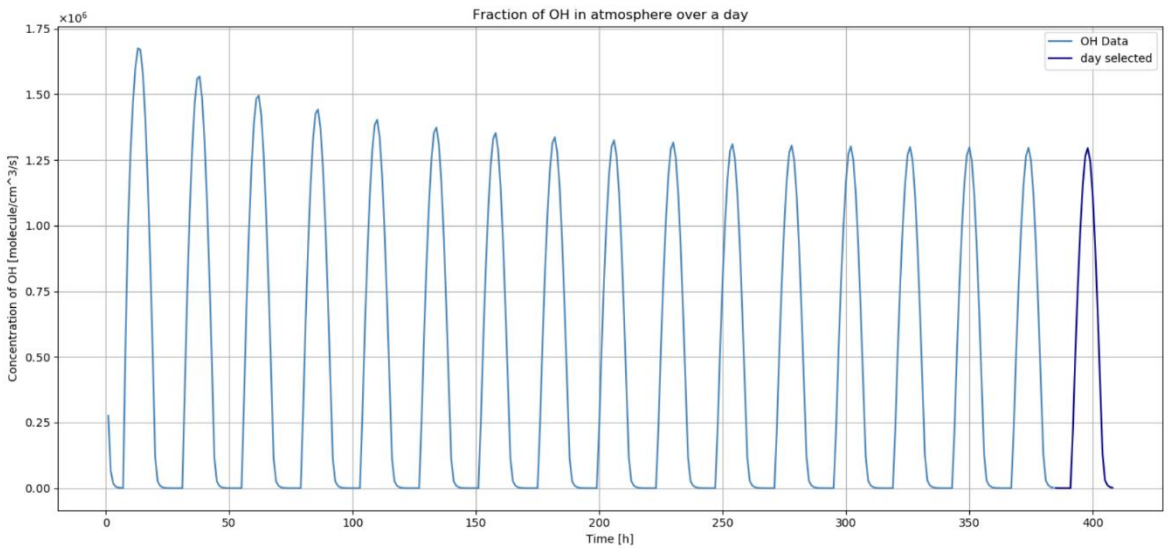

Figure 3.3.2.1: OH profile with GFDL chemical scheme at 25 kilometers.

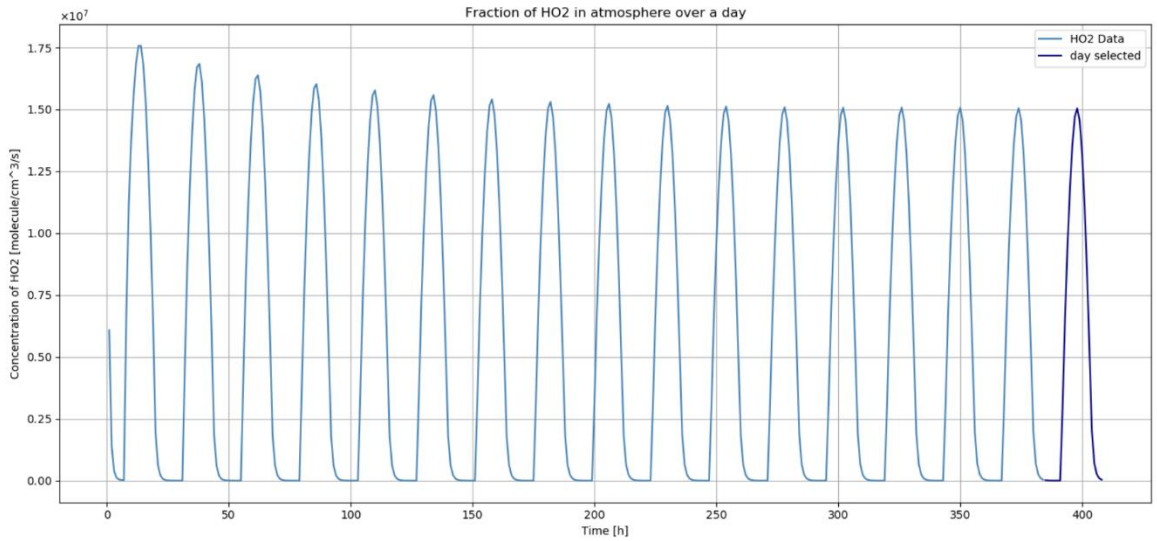

Figure 3.3.2.2: HO_2 profile with GFDL chemical scheme at 25 kilometers.

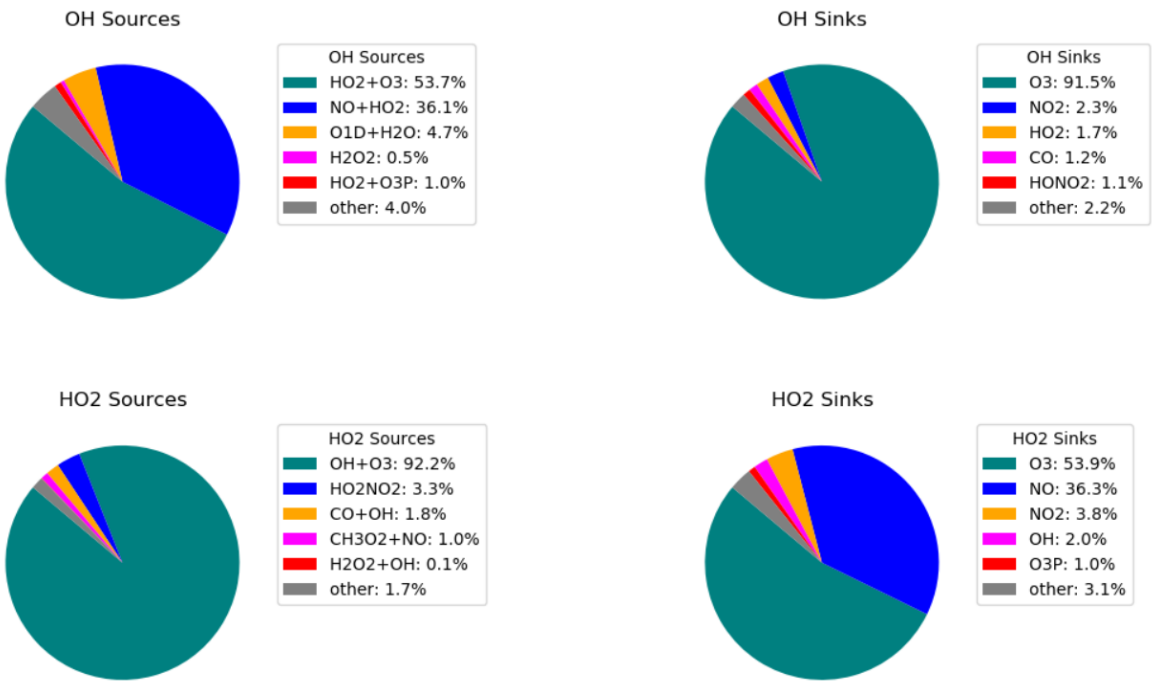

Figure 3.3.2.3: aerograms of the most important reaction contribution for the formation and destruction of OH and HO_2 at 1:00 p.m. with the GFDL chemical scheme at 25 kilometers

Also in this simulation few days are necessary to obtain a more stable solution.
The reactivity of the stratosphere changes significantly at an altitude of 25 kilometres. The concentrations of both OH and HO_2 increase at this altitude, and their atmospheric fractions rise considerably, as shown in Table 3-9.
The main component in the lifecycle of the two gases is now the ozone (O_3), since the ozone layers increase his thickness around 20 kilometres (Jucks, Margitan, & Sasano, 1998). O_3 is for more the 50% responsible to produce OH with its reaction with HO_2, and the reactions that convolve the oxygen atoms (O^1D and O^3P) formed by the photodissociation of the ozone, plays a role in the OH formation.
The OH destruction is almost fully due to the reaction OH + O_3, that is also responsible for 92% of the formation of HO_2.
The NO still has an impact on the destruction of HO_2 and in the formation of OH with the reaction NO + HO_2 -> NO_2 + OH, but now far less relevant than before.

3.3.2.1. Impact of H_2 increase on atmospheric reactivity at 25 Km

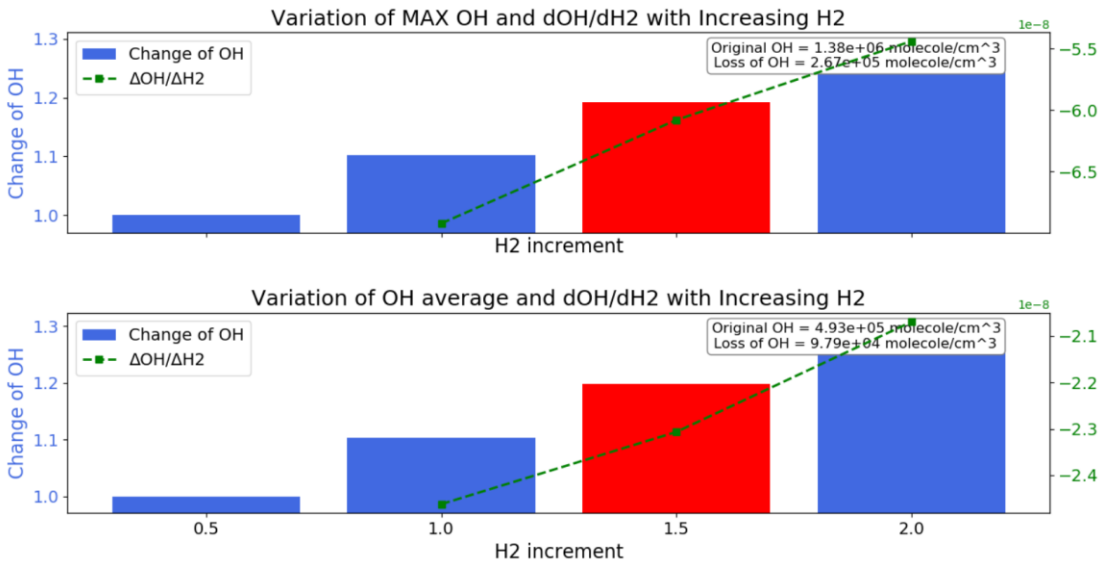

Figure 3.3.2.4: Effect of increasing H_2 on both the maximum and the average OH at 25 Km. The total loss of OH is between the initial value and the one with 1.5 ppm of hydrogen in atmosphere.

At this higher stratospheric level, the effect of increased hydrogen concentration changes: the amount of OH increases with H_2 instead of decreasing. As shown in Figure 3.3.2.3, the contribution of H_2 to OH reduction is already below 1%. The GFDL mechanism includes two reactions that consume H_2:

$$H_2 + OH \rightarrow H_2O + HO_2$$

$$H_2 + O^1D + O_2 \rightarrow HO_2 + OH$$

In the marine environment and in the lower stratosphere, this second reaction is almost negligible. However, at higher altitudes, where ozone levels are greater and its subsequent breakdown produces atomic oxygen, hydrogen begins to have a positive effect on OH concentrations due to this reaction.

The maximum value of OH in an atmosphere with 1.5 ppm of H_2 increase of 7.3E+4 molecules/cm^3, so a 5% increment.

Tables 3-8, 3-9 and 3-10 report the reaction rates for processes involving OH and H_2 at various altitudes. At ground level, the reaction between H_2 and O^1D is nearly

negligible, contributing only about 0.008% compared to the much faster H_2 + OH reaction. However, as altitude increases, the relative importance of the H_2 + O^1D pathway grows.

At 25 km, the rates of the two reactions become comparable, making H_2 + O^1D not only a significant direct source of OH, but also an indirect one. The HO_2 produced by this reaction can further react with ozone, regenerating OH and thus mitigating the OH depletion caused by the H_2 + OH reaction. Since the HO_2 + O_3 reaction represents the main source of OH (contributing over 50% of its production), any enhancement in this pathway has a considerable effect. As shown in Table 3-9, an increase in atmospheric H_2 from 0.5 to 1.5 ppm leads to a 17% rise in the HO_2 + O_3 reaction rate.

3.3.3. Stratospheric atmosphere at 40 Km.

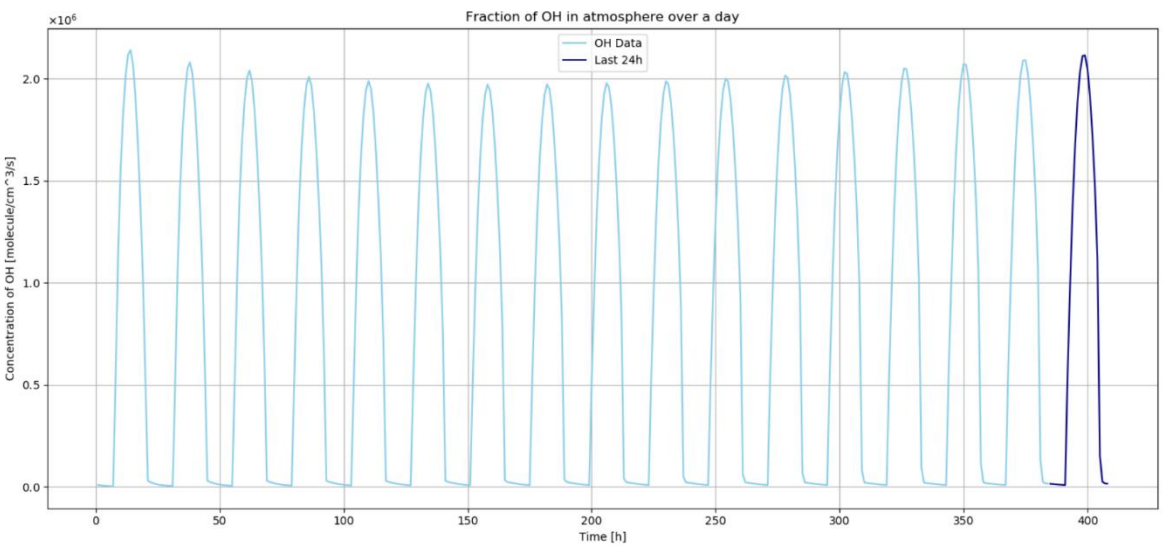

Figure 3.3.3.1: OH profile with GFDL chemical scheme at 40 kilometers.

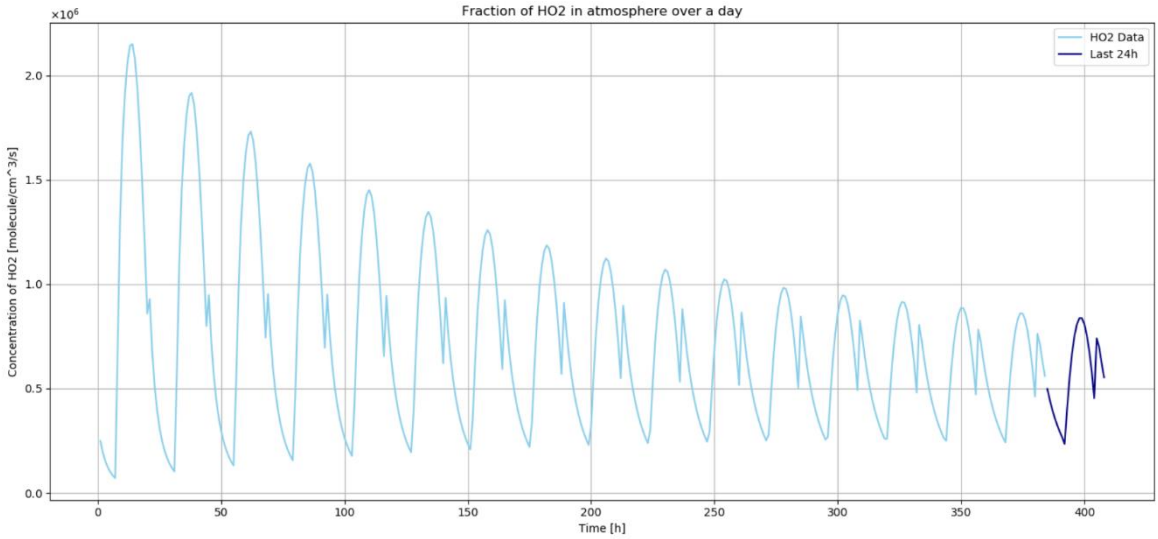

Figure 3.3.3.2: HO_2 profile with GFDL chemical scheme at 40 kilometers.

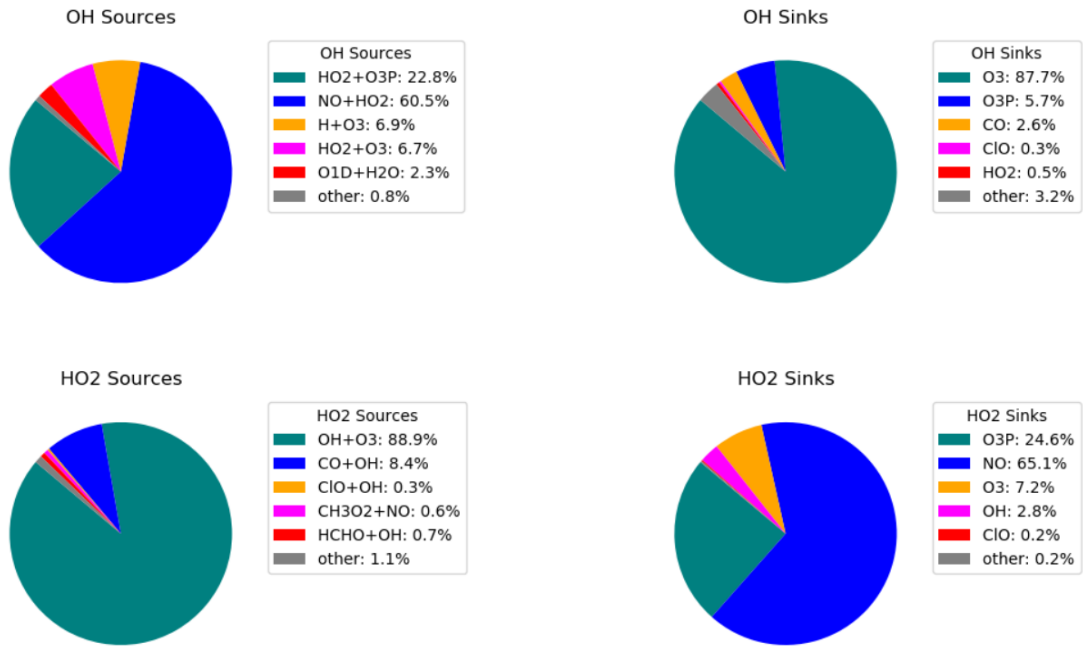

Figure 3.3.3.3 : aerograms of the most important reaction contribution for the formation and destruction of OH and HO_2 at 1:00 p.m. with the GFDL chemical scheme at 40 kilometers

The final simulation is performed at 40 kilometres. The OH level is increased from the one obtained at 25 kilometres in both concentration and atmospheric fraction, as reported in the table 3-9.

At this altitude,HO_2 concentration is inferior to OH, as reported by (Penn state university, s.d.). Is clear that in the upper levels of the stratosphere OH is dominant respect to HO_2 in term of atmospheric characterization.

The relevant reactions in the lifecycle of both the gases are changed again. O_3 maintain its centrality, and now the O^3P, produced by the photodissociation of the ozone, is the main source of OH, thanks to the reaction with HO_2.

This result also shows that at higher altitudes, the most important product of the photodissociation of the ozone for OH and HO_2 is the O^3P, and not anymore the O^1D.

The NOx components loses again their relevance respect to the lower layers of the atmosphere, and at this altitude the contribution of more complex component, and in general most of the carbon-based molecules (except CO) is almost negligible.

	marine troposphere			stratosphere 15 Km		
	Conc	M	fraction	Conc	M	fraction
OH	7.10E+06	4.04E-05	2.92E-13	1.50E+06	6.62E-06	3.76E-13
HO_2	4.00E+08	4.04E-05	1.65E-11	4.20E+06	6.62E-06	1.05E-12

Table 3-6: concentration and fraction of OH and HO_2 in troposphere and lower level of stratosphere. The Concentration and M are both in molecules/cm^3

	stratosphere 25 Km			stratosphere 40 Km		
	Conc	M	fraction	Conc	M	fraction
OH	1.25E+06	1.31E-06	1.52E-12	2.20E+06	1.34E-07	2.71E-11
HO_2	1.50E+07	1.31E-06	1.83E-11	8.00E+04	1.34E-07	9.86E-13

Table 3-7: concentration and fraction of OH and HO_2 in middle and high levels of stratosphere. The Concentration and M are both in molecules/cm^3

In the tables 3-6 and 3-7 are reported the concentrations and the fractions of both OH and HO_2 in the three different altitudes simulated.

3.3.3.1. Impact of H_2 increase on atmospheric reactivity at 40 Km

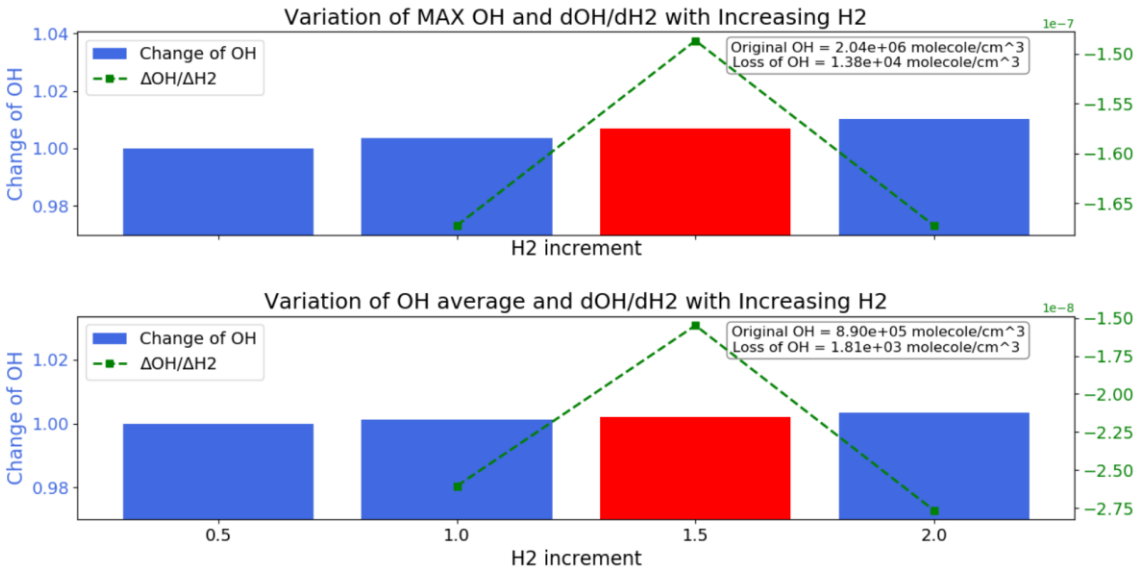

Figure 3.3.3.4: Effect of increasing H_2 on both the maximum and the average OH at 40 Km. The total loss of OH is between the initial value and the one with 1.5 ppm of hydrogen in atmosphere.

The results obtained at the highest stratospheric level confirm those observed at the intermediate level. The graph in figures 3.3.3.4 shows that when ozone levels are sufficiently high, the influence of hydrogen on OH concentrations becomes positive. In fact, the maximum of OH increase by 1.78×10^4 molecules/cm³, which corresponds to less than 1%.

Altitudes	H_2 ppm	OH Fraction	$H_2+O^1D+O_2 \rightarrow HO_2+OH$	$H_2+OH \rightarrow H_2O+HO_2$
0 Km	0.5	2.95E-13	4.420E+01	6.020E+05
0 Km	1.5	2.60E-13	1.320E+02	1.590E+06
15 Km	0.5	3.395E-13	2.190E+01	2.210E+03
15 Km	1.5	3.391E-13	5.950E+01	5.870E+03

Table 3-8: Reaction rates for OH formation and destruction involving H_2 at ground level and at 15 km altitude. The reaction rates are reported in [molecules/cm³/s]

Altitudes	H_2 ppm	OH Fraction	$H_2+O^1D+O_2 \rightarrow HO_2+OH$	$H_2+OH \rightarrow H_2O+HO_2$	$HO_2+O_3 \rightarrow OH+2O_2$
25 Km	0.5	1.534E-12	2.479E+02	4.446E+02	7.68E+04
25 Km	1.5	1.613E-12	7.425E+02	1.401E+03	9.01E+04

Table 3-9: Reaction rates for OH formation and destruction involving H_2 at 25 Km. The reaction rates are reported in [molecules/cm^3/s]

Altitudes	H_2 ppm	OH Fraction	$H_2+O^1D+O_2 \rightarrow HO_2+OH$	$H_2+OH \rightarrow H_2O+HO_2$
40 Km	0.5	2.51E-11	4.868E+00	1.806E+02
40 Km	1.5	2.53E-11	1.353E+01	5.054E+02

Table 3-10: Reaction rates for OH formation and destruction involving H_2 at 40 Km. The reaction rates are reported in [molecules/cm3/s]

Compared to the effect observed at 25 km, the positive impact of increased H_2 on OH levels is less pronounced at 40 km, as reported in table 3-10. This is primarily due to the significantly lower concentration of HO_2 at this altitude compared to the lower layers of the stratosphere, which limits the extent to which the HO_2 reactions with O^3P and NO can regenerate OH. Consequently, the indirect contribution of H_2 to OH production becomes less effective in the upper stratosphere.

4 Conclusions

The results presented in this work demonstrate the feasibility of performing atmospheric simulations using two different chemical models proposed in the literature. Although the simulations required a non-negligible computational effort, the box model approach can reproduce the experimental data with good accuracy.

The different configurations proposed in this work highlight the huge contribution that different photochemical data can have on the profiles of both OH and HO_2, key molecules that play a crucial role in shaping atmospheric composition.

The simulations performed confirm the substantial differences in terms of reactions and chemical composition between the two studied environments and the atmospheric layers.

1. The marine atmosphere is completely dominated by the photodissociation of the oxygen molecules and the oxidation of the carbon species with low carbon number. Simulations reach stability more quickly compared to other environments, as the smaller number of relevant molecules and their lower concentrations result in more stable and easily manageable simulations.

2. The urban simulation is fully characterized by the huge presence of nitrogen oxides, molecules that are located almost only in cities. This highlights the significant impact that human activity can have, fundamentally altering the composition of the atmosphere that surrounds us. The difficult in the simulation in this complex environment though does not consent an easy description of the urban atmosphere; the simulations required numerous days to achieve a stability. Nevertheless, the composition of the urban atmosphere is far more relevant in the context of the human health than to its effect on global atmosphere, as urban areas are extremely small compared to the marine environment.

3. In the upper layer of the atmosphere analysed, from 15 to 40 km, ozone (O_3) emerges as the key molecule influencing OH and HO_2. The ozone layer drastically alters the main pathways for the formation and destruction of both OH and HO_2, both directly and indirectly, as its photolysis products also have a significant impact on stratospheric composition. As in the case of urban simulations, several days are required for the stratospheric simulations to reach a stable solution.

The final part of the investigation focused on the analysis of the effect of hydrogen increment in each simulation. The results reported in the literature are confirmed by this work: the increment in the atmosphere of H_2 can subtract OH from the atmosphere, partially neglecting its capacity to oxidise other component like methane (CH_4). This effect is observed in both the troposphere and the lower stratosphere. However, it does not hold true for the upper stratosphere, where interactions between hydrogen, ozone and single oxygen atoms can actually lead to an increase in OH levels.

The GWP [100] obtained in this thesis was derived under conditions in which the effect of H_2 on OH is close to its maximum. The high average temperatures of the days selected for the simulations, along with the assumptions made about the atmosphere (clear skies and perfectly mixed air), lead to a GWP that is considerably higher than that averaged over an entire year. The GWP reported in the marine environment is significantly higher than that obtained in urban environment, this effect is due to the minor relevance that H_2 has in a polluted atmosphere, where the reactivity is almost fully characterized by NOx.

All things considered, the effect of hydrogen as a co-greenhouse gas, although not negligible, does not outweigh its advantages in the contrast of the climate change and its potential as a green fuel. It is also important to note, however, that the main drawback of hydrogen as a fuel does not lie in its impact as greenhouse gas, but rather in the challenges associated with its production and storage.

Future studies in this field will undoubtedly investigate the detailed contribution of the hydrogen soil sink, as it represents the main source of uncertainty in term of quantification of the total increase of atmospheric H_2 in a hydrogen-cantered economy. Additionally, a deeper understanding of the chemical reactions occurring in urban environments is crucial to improve the accuracy and stability of future simulations.

Bibliography

[1]. Chance, K., Stachnik, R., & Salawitch, R. (1996). Simultaneous measurements of stratospheric HOx, NOx, and Clx: Comparison with a photochemical model. *JOURNAL OF GEOPHYSICAL RESEARCH*, 9031-9043.

[2]. Dusanter, S., Vimal, D., & Stevens, P. S. (2010). Measurements of OH and HO2 concentrations during the MCMA-2006 field campaign – Part 2: Model comparison and radical budget. *Atmospheric Chemistry and Physics*, 1555-1576.

[3]. EPA. (2025, January). *Understanding Global Warming Potentials*. Retrieved from https://www.epa.gov/ghgemissions/understanding-global-warming-potentials

[4]. ESA. (2019, 03 12). *Nitrogen dioxide pollution mapped*. Retrieved from https://www.esa.int/Applications/Observing_the_Earth/Copernicus/Sentinel-5P/Nitrogen_dioxide_pollution_mapped

[5]. Folberth, G. A., Hauglustaine, D. A., Lathière, J., & Brocheton, F. (2006). Interactive chemistry in the Laboratoire de Météorologie Dynamique general circulation model: model description and impact analysis of biogenic hydrocarbons on tropospheric chemistry. *European Geosciences Union*.

[6]. Gershenzo, Y. M., Zvenigorodskii, S. G., & Rozenshtein, V. B. (1990). The chemistry of OH and HO2 radicals in the earth's atmosphere. *Russian Chemical Reviews*.

[7]. He, J., Naik, V., & Horowitz, L. W. (2021). Hydroxyl Radical (OH) Response to Meteorological Forcing and Implication for the Methane Budget. *Advancing earth and space sciences*.

[8]. Horowitz, L. W., Naik, V., & Paulot, F. (2020). The GFDL Global Atmospheric Chemistry-Climate. *Journal of advances in modeling earth system*.

[9]. IPCC. (2021). *Intergovernmental Panel on Climate Change.* IPCC, Switzerland.

[10]. IUPAC. (n.d.). *Evaluated kinetic data*. Retrieved from https://iupac.aeris-data.fr/

[11]. Jucks, K. W., Margitan, J. J., & Sasano, Y. (1998). Observations of OH, HO2, H2O, and O3 in the upper stratosphere: implications for HOx photochemistry. *Geophysical Research Letters*, 3935-3938.

[12]. McCabe, D., TomaszGierczak, Talukdar, R., & Ravishank, A. R. (2001). Kinetics of the reaction OH + CO under atmosphericcondition. *GEOPHYSICAL RESEARCH LETTERS*, 3135-3138.

[13]. MCM. (n.d.). *photolysis Parameters*. Retrieved from https://mcm.york.ac.uk/MCM/rates/photolysis

[14]. Meda, U. S., Bhat, N., & Pandey, A. (2023). Challenges associated with hydrogen storage systems due to the hydrogen embrittlement of high strength steels. *International Journal of Hydrogen Energy*, 17894-17913.

[15]. NASA. (1962). *U.S. standard atmosphere* . Washington, D.C.

[16]. NASA. (n.d.). *Carbon Dioxide*. Retrieved from Nasa Climate: https://climate.nasa.gov/vital-signs/carbon-dioxide/?intent=121

[17]. NASA. (n.d.). *Earth observatory*. Retrieved from global worming: https://earthobservatory.nasa.gov/features/GlobalWarming/page2.php

[18]. Nguyen, D.-H., Lin, C., & Vu, C.-T. (2022). Tropospheric ozone and NO. *Environmental Technology & Innovation*.

[19]. NIST. (2025). *NIST chemical kinetics database*. Retrieved from https://kinetics.nist.gov/kinetics/

[20]. *NOAA solar calculation*. (2025). Retrieved from Global monitoring laboratory: https://gml.noaa.gov/grad/solcalc/index.html

[21]. *Penn state university*. (n.d.). Retrieved from stratospheric chemistry: https://personal.ems.psu.edu/~brune/m532/meteo532_ch7_stratospheric_chemistry.htm

[22]. Reichle, D. E. (2023). *The Global Carbon Cycle and Climate Change.* Elsevier.

[23]. Sand, M., Skeie, R. B., & Sandstad, M. (2023). A multi-model assessment of the Global Warming. *earth and environment* .

[24]. Sheehy, P. M., Volkamer, R., Molina, L. T., & Molina, M. J. (2010). Oxidative capacity of the Mexico City atmosphere. *Atmospheric Chemistry and physics*, 6993-7008.

[25]. Sobrino, F. H., Monroy, C. R., & Pérez, J. L. (2010). Critical analysis on hydrogen as an alternative to fossil fuels and biofuels for vehicles in Europe. *Renewable and Sustainable Energy Reviews*, 772-780.

[26]. Solomon, S. (1999). *Review of geophysics.* Boulder: AGU.

[27]. stockwell, W. R. (1995). on the HO2+HO2 reaction: its misapplication in atmospheric chemistry model. *journal of geophysical research*, 11695-11698.

[28]. Stone, D., Whalleya, L. K., & Heard, D. E. (2012). Tropospheric OH and HO2 radicals: field measurements and model comparisons. *Chemical Society Reviews*.

[29]. TRENBERTH, K. N., FASULLO, J. N., & L, J. K. (2009). EARTH'S GLOBAL. *American Meteorological Society*, 314.

[30]. *U.S. Standard Atmosphere.* (1976). Washington D.C.

[31]. Wang, Y., Ming, T., & Li, W. (2022). Atmospheric removal of methane by enhancing the natural hydroxyl radical sink. *SCI*.

[32]. Warwick, N., & Griffiths, P. (2022). Atmospheric implications of Increased Hydrogen used.

[33]. Whalley, L. K., & Furneaux, K. L. (2010). The chemistry of OH and HO2 radicals in the boundary layer. *Atmospheric Chemistry and physics* , 1555-1557.

[34]. Zhang, T., Wang, R., & Wang, W. (2014). Water effect on the formation of 3O2 from the self-reaction of two HO2 radicals in tropospheric conditions. In T. Mineva, & J. Li, *Computational and Theoretical Chemistry* (pp. 134-144).

B Equations for the evaluation of the SZA

The equations used to compute the Solar Zenith Angle (SZA) are presented below, as derived from the (NOAA solar calculation, 2025). This set of equations enables verification of SZA values with precision down to the hour.

The days used in the equations are reported using the Julian Calendar (JDC), to represent the time in a continuous way. The starting day is the first January of the year 1900. Before the evaluation of the SZA, some preliminary equations are needed:

$$Day_{converted} = (Year - 1900) * 365.25 + Day$$

$$Hour(JDC) = \frac{hour}{24}$$

$$Day_j = Day_{converted} + 2415018.5 + Hour_{converted} - \frac{Time_{zone}}{24}$$

The number 2415018.5 correspond to the first January 1900 at 0:00 UT, the hour is divided by 24 to consider it in the day value.

$$Century_j = T_j = \frac{(day_j - 2451545.0)}{36525.0}$$

The number 2451545.0 correspond to January first of the 2000 at 12:00 UT, and 36525.2 represent the numbers of days in a year in the Julian calendar.

- Evaluation of the mean obliquity of the elliptic:

$$\varepsilon_{mean} = 23° + \frac{26'}{60} + (21.448'' - \frac{T_j\left(46.815'' + T_j(0.00059'' - T * 0.001816'')\right)}{3600}$$

The term in second and arcsecond are converted in degrees.

- Correct obliquity equation:

$$\varepsilon = \varepsilon_{mean} + 0.00256° * \cos(rad(125.04 - 1934.136 * T_j))$$

This equation accounting the nutation of the axis rotation and the cousin argument consider the longitude of the ascending node.

- Evaluation of the Geometric Mean Anomaly of the Sun:

$$M_j = 357.52911° + T_j * \left(35999.05029° - 0.0001537° * T_j\right)$$

- Evaluationo of the position of the centre of the Sun:

$$C_j = \sin(M_j) * \left(1.914602 - T_j * \left(0.004817 + 0.000014 * T_j\right)\right) + \sin(2M_j) * \left(0.019993 - 0.000101 * T_j\right) + \sin(3M_j) * 0.000289$$

- Sun's geometric Mean Longitude evaluation:

$$L_{0_j} = 280.46646° + T_j * \left(36000.76983° + 0.0003032° * T_j\right)$$

- Evaluation of the Sun true longitude:

$$L_j = L_{oj} + C_j$$

- Sun apparent Longitude equation:

$$L_{aj} = L_j - 0.00559° - 0.00478° * \sin(rad(125.04 - 1934.136 * T_j))$$

- Eccentricity of Earth's orbit evaluation:

$$e_j = 0.016708634 - T_j * (0.000042037 + 0.0000001267 * T_j)$$

- Variation of y:

$$var_y = \tan(rad\left(\frac{\varepsilon}{2}\right)) + \tan(rad\left(\frac{\varepsilon}{2}\right))$$

- Equation of Time:

$$\begin{aligned}\Delta t_{ey} = 4 * rad(var_y \\ * \sin\left(2 * rad(L_{0j})\right) - 2 * e_j \\ * \sin\left(rad(M_j)\right) + 4 * e_j * var_j \\ * \sin\left(rad(M_j)\right) * \cos\left(2 * rad(L_{oj})\right) - 0.5 * var_y * var_y \\ * \sin\left(4 * rad(L_{oj})\right) - 1.25 * e_j * e_j * \sin\left(2 * rad(M_j)\right)\end{aligned}$$

This equation consents the evaluation of the discrepancy between the apparent solar time and the mean solar time. The value is in minute.

Now is possible to evaluate the Solar Zenith Angle knowing the true solar time, the sun decline and the hour angle.

$$S_{time} = Hour\ (JCD) * 1440 + \Delta t_{ey} + 4 * LON - 60 * Time_{zone} \qquad in\ minute\ [0, 1440]$$

$$Sun_{dec} = rad\ (\sin^{-1}(\sin(rad(\varepsilon)) * \sin\left(rad(L_{aj})\right))$$

The hour angle can have two values:

$$\frac{S_{time}}{4} < 0 \qquad Hour_{angle} = \frac{S_{time}}{4} + 180$$

$$\frac{S_{time}}{4} > 0 \qquad Hour_{angle} = \frac{S_{time}}{4} - 180$$

Finally, the Solar Zenith Angle is obtained

$$SZA = rad\left(\cos^{-1}(\sin\left(rad(LAT)\right) * \sin\left(rad(SUN_{decl})\right) + \cos\left(rad(LAT)\right) * \cos\left(rad(SUN_{decl})\right) * \cos\left(rad\left(Hour_{angle}\right)\right)\right))$$

List of Figures

Figure 1.1.1.1: Impact of different molecules on the greenhouse effect. (IPCC, 2021) .. 2

Figure 1.1.1.2: greenhouse effect with each effect displayed as Wm^{-2}. (TRENBERTH, FASULLO, & L, 2009) 3

Figure 1.1.2.1: Ozone layer profile in the troposphere and the stratosphere (Jucks, Margitan, & Sasano, 1998) 5

Figure 1.1.2.2: Temperature, pressure, speed of sound and density in different layers of the atmosphere (NASA, U.S. standard atmosphere , 1962) 6

Figure 1.1.2.3: Nitrogen dioxide worldwide. Is easy to see that the NO_2 is high in concentration in the urban environment, and decrease in the see, especially in the artic and Antarctic regions (ESA, 2019) 7

Figure 1.1.3.1: The image shows the HO_2 cycle in the atmosphere. The solid lines represent reactions relevant in the marine environment, where human pollution is low, while the dashed lines indicate reactions occurring at high NO_x levels, which are much more common in urban environments 10

Figure 1.1.3.1: Hydrogen permeation in film and substrate mechanism (Meda, Bhat, & Pandey, 2023) 11

Figure 1.2.2.1: H_2 concentration in the atmosphere as a function of emissions: the black line corresponds to a fixed soil sink flux; the red one represents a flux that increases with the H_2 level (Warwick & Griffiths, 2022) 14

Figure 2.1.1.1: Climatological annual means tropospheric OH average globally and regionally compared with other chemical schemes (Horowitz, Naik, & Paulot, 2020). 20

Figure 2.1.4.1: rate constant for the $2HO_2 \rightarrow H_2O_2 + O_2$. The water in the lower layers of the atmosphere impact for more than 50% (stockwell, 1995). 22

Figure 2.1.4.2: Plot of the rate constant K (in units of 10^{-13} cm^3 $molecule^{-1}$ s^{-1}) as a function of M (in units of 10^{-19} cm^{-3}) at different atmospheric temperatures (McCabe, TomaszGierczak, Talukdar, & Ravishank, 2001). 24

Figure 2.2.1.1: air box represented as a reactor 32

Figure 3.1.1.1: OH concentration profile obtained from GFDL chemical scheme in marine environment with IUPAC photochemical data. 41

Figure 3.1.1.2: HO_2 concentration profile obtained from GFDL chemical scheme in marine environment with IUPAC photochemical data. 42

Figure 3.1.1.3: Comparison of the highest reaction rates for the formation and removal of OH and HO_2 with the benchmark from the GFDL chemical scheme, under marine conditions and based on IUPAC photochemical data. 42

Figure 3.1.1.4: aerograms of the most important reactions contribution for the formation and destruction of OH and HO_2 at 1:00 p.m. with the GFDL chemical scheme, under marine conditions and based on IUPAC photochemical data. 43

Figure 3.1.1.5: OH concentration profile obtained from GFDL chemical scheme in marine environment with MCM photochemical data 44

Figure 3.1.1.6: HO_2 concentration profile obtained from GFDL chemical scheme in marine environment with IUPAC photochemical data. 45

Figure 3.1.1.7: Comparison of the highest reaction rates for the formation and removal of OH and HO_2 with the benchmark from the GFDL chemical scheme, under marine conditions and based on MCM photochemical data. 45

Figure 3.1.1.8: aerograms of the most important reactions contributions for the formation and destruction of OH and HO_2 at 1:00 p.m. with the GFDL chemical scheme, under marine conditions and based on MCM photochemical data. 46

Figure 3.1.1.9: OH concentration profile obtained from GFDL chemical scheme in marine environment with MCM photochemical data and the added reactions 47

Figure 3.1.1.10: HO_2 concentration profile obtained from GFDL chemical scheme in marine environment with MCM photochemical data and the added reactions 47

Figure 3.1.1.11: Comparison of the highest reaction rates for the formation and removal of OH and HO_2 with the benchmark from the GFDL chemical scheme, under marine conditions, based on MCM photochemical data and the added reactions 48

Figure 3.1.1.12: aerograms of the most important reaction contribution for the formation and destruction of OH and HO_2 at 1:00 p.m. with the GFDL chemical scheme, under marine conditions, based on MCM photochemical data and the added reactions 48

Figure 3.1.1.13: Brute force analysis of OH with GFDL chemical scheme in marine environment 50

Figure 3.1.1.14: Brute force analysis of HO_2 with GFDL chemical scheme in marine environment 50

Figure 3.1.1.15: Effect of increasing H_2 on both the maximum and the average OH with GFDL chemical scheme. The total loss of OH is calculated between the initial value and the one with 1.5ppm of hydrogen in atmosphere. 51

Figure 3.1.2.1: OH concentration profile obtained from LMDz chemical scheme in marine environment with IUPAC photochemical data. 53

Figure 3.1.2.2: HO_2 concentration profile obtained from LMDz chemical scheme in marine environment with IUPAC photochemical data. 54

Figure 3.1.2.3: Comparison of the highest reaction rates for the formation and removal of OH and HO_2 with the benchmark from the LMDz chemical scheme, under marine conditions, based on IUPAC photochemical data. 54

Figure 3.1.2.4: aerograms of the most important reaction contribution for the formation and destruction of OH and HO_2 at 1:00 p.m. with the LMDz chemical scheme, under marine conditions, based on IUPAC photochemical data. 55

Figure 3.1.2.5: contribution in the elimination of H 56

Figure 3.1.2.6: OH concentration profile obtained from LMDz chemical scheme in marine environment with MCM photochemical data. 56

Figure 3.1.2.7: HO_2 concentration profile obtained from LMDz chemical scheme in marine environment with MCM photochemical data. 57

Figure 3.1.2.8: Comparison of the highest reaction rates for the formation and removal of OH and HO_2 with the benchmark from the LMDz chemical scheme, under marine conditions, based on MCM photochemical. 57

Figure 3.1.2.9: aerograms of the most important reaction contribution for the formation and destruction of OH and HO_2 at 1:00 p.m. with the LMDz chemical scheme, under marine conditions, based on MCM photochemical data. 58

Figure 3.1.2.10: OH concentration profile obtained from LMDz chemical scheme in marine environment with MCM photochemical data and added reactions 59

Figure 3.1.2.11: HO_2 concentration profile obtained from LMDz chemical scheme in marine environment with MCM photochemical data and added reactions 59

Figure 3.1.2.12: Comparison of the highest reaction rates for the formation and removal of OH and HO_2 with the benchmark from the LMDz chemical scheme, under marine conditions, based on MCM photochemical and added reactions 60

Figure 3.1.2.13: Comparison of the highest reaction rates for the formation and removal of OH and HO_2 with the benchmark from the LMDz chemical scheme, under marine conditions, based on MCM photochemical and added reactions. 60

Figure 3.1.2.14: Brute force analysis of OH 61

Figure 3.1.2.15: Brute force analysis of HO_2 61

Figure 3.1.2.16: Effect of increasing H_2 on both the maximum and the average OH with LMDz chemical scheme. The total loss of OH is between the initial value and the one with 1.5ppm of hydrogen in atmosphere. 62

Figure 3.2.1.1: OH and HO_2 profile in urban environment with GFDL chemical model and photochemical data taken from IUPAC 65

Figure 3.2.1.2: OH and HO_2 concentrations in the two days analyzed with photochemical data taken from IUPAC 65

Figure 3.2.1.3: OH production and destruction rates for the two days considered with photochemical data taken from IUPAC 66

Figure 3.2.1.4: HO_2 production and consumption rates in the two days considered with photochemical data taken from IUPAC 66

Figure 3.2.1.5: OH and HO_2 profile in urban environment with GFDL model and photochemical data taken from IUPAC in 40 days 67

Figure 3.2.1.6: OH and HO_2 concentration profile in urban environment with GFDL model and photochemical rate constants taken from MCM 68

Figure 3.2.1.7: OH and HO_2 concentrations in the two days analyzed with photochemical data taken from MCM 68

Figure 3.2.1.8: OH production and destruction rates for the two days considered with photochemical data taken from MCM 69

Figure 3.2.1.9: HO_2 production and consumption rates in the two days considered with photochemical data taken from MCM 69

Figure 3.2.1.10: OH and HO_2 concentration profile in urban environment with GFDL model and photochemical data taken from MCM with added reactions 70

Figure 3.2.1.11: OH and HO_2 concentrations in the two days analyzed with photochemical data taken from MCM with added reactions 70

Figure 3.2.1.12: OH production and destruction rates for the two days considered with photochemical data taken from MCM with added reactions 71

Figure 3.2.1.13: HO_2 production and consumption rates in the two days considered with photochemical data taken from MCM with added reactions 71

Figure 3.2.1.14: effect of the NOx concentration on the system stabilization and the HO_2/OH ratio 72

Figure 3.2.1.15: Effect of increasing H_2 on both the maximum and the average OH with GFDL chemical scheme. The total loss of OH is between the initial value and the one with 1.5ppm of hydrogen in atmosphere. 73

Figure 3.2.2.1: OH and HO_2 concentration profile in urban environment with LMDz model and photochemical data taken from IUPAC 75

Figure 3.2.2.2: OH and HO_2 concentrations in the two days analyzed with photochemical data taken from IUPAC 75

Figure 3.2.2.3: OH production and destruction rates for the two days considered with photochemical data taken from IUPAC 76

Figure 3.2.2.4: HO_2 production and destruction rates for the two days considered with photochemical data taken from IUPAC 76

Figure 3.2.2.5: OH and HO_2 concentration profile in urban environment with LMDz model and photochemical data taken from MCM 77

Figure 3.2.2.6: OH and HO_2 concentrations in the two days analyzed with photochemical data taken from MCM with added reactions. 78

Figure 3.2.2.7: OH production and destruction rates for the two days considered with photochemical data taken from MCM 78

Figure 3.2.2.8: HO_2 production and destruction rates for the two days considered with photochemical data taken from MCM with added reactions 79

Figure 3.2.2.9: OH and HO_2 concentration profile in urban environment with LMDz model and photochemical data taken from MCM with added reactions 80

Figure 3.2.2.10: OH and HO_2 concentrations in the two days analyzed with photochemical data taken from MCM with added reactions. 80

Figure 3.2.2.11: OH production and destruction rates for the two days considered with photochemical data taken from MCM with added reactions 81

Figure 3.2.2.12: HO_2 production and destruction rates for the two days considered with photochemical data taken from MCM with added reactions 81

Figure 3.2.2.13: effect of the NOx concentration on the system stabilization and the HO_2/OH ratio 82

Figure 3.2.2.14: Effect of increasing H_2 on both the maximum and the average OH with LMDz chemical scheme. The total loss of OH is between the initial value and the one with 1.5 ppm of hydrogen in atmosphere. 83

Figure 3.3.1.1: OH profile with GFDL chemical scheme at 15 kilometers. 84

Figure 3.3.1.2: HO_2 profile with GFDL chemical scheme at 15 kilometers 85

Figure 3.3.1.3: aerograms of the most important reaction contribution for the formation and destruction of OH and HO_2 at 1:00 p.m. with the GFDL chemical scheme at 15 kilometers 85

Figure 3.3.1.4: Effect of increasing H_2 on both the maximum and the average OH at 15 Km. The total loss of OH is between the initial value and the one with 1.5ppm of hydrogen in atmosphere. 87

Figure 3.3.2.1: OH profile with GFDL chemical scheme at 25 kilometers. 88

Figure 3.3.2.2: HO_2 profile with GFDL chemical scheme at 25 kilometers. 88

Figure 3.3.2.3: aerograms of the most important reaction contribution for the formation and destruction of OH and HO_2 at 1:00 p.m. with the GFDL chemical scheme at 25 kilometers 89

Figure 3.3.2.4: Effect of increasing H_2 on both the maximum and the average OH at 25 Km. The total loss of OH is between the initial value and the one with 1.5 ppm of hydrogen in atmosphere. 90

Figure 3.3.3.1: OH profile with GFDL chemical scheme at 40 kilometers. 91

Figure 3.3.3.2: HO_2 profile with GFDL chemical scheme at 40 kilometers. 92

Figure 3.3.3.3 : aerograms of the most important reaction contribution for the formation and destruction of OH and HO_2 at 1:00 p.m. with the GFDL chemical scheme at 40 kilometers 92

Figure 3.3.3.4: Effect of increasing H_2 on both the maximum and the average OH at 40 Km. The total loss of OH is between the initial value and the one with 1.5 ppm of hydrogen in atmosphere. 94

List if Tables

Table 1-1: Emission of greenhouse gases in a year and percentage removed by OH oxidation (Wang, Ming, & Li, 2022) 9

Table 1-2: percentage of H_2 leaking in a global hydrogen economy (Warwick & Griffiths, 2022) 13

Table 1-3: values for the evaluation of a obtained by the literature (Warwick & Griffiths, 2022) 16

Table 1-4: GWP of H_2 of different contributions using both the data from IPCC AR5 and AR6 in 20 and 100 years (Warwick & Griffiths, 2022). 17

Table 2-1: Marine reactions added to both GFDL and LMDz (Whalley & Furneaux, 2010) 27

Table 2-2: Photochemical marine reactions added to both GFDL and LMDz (Whalley & Furneaux, 2010) 27

Table 2-3: Added reactions for the simulation of HCO behavior in atmosphere 28

Table 2-4: photochemical reactions added from IUPAC and MCM database 29

Table 2-5: kinetic parameter reported by (Whalley & Furneaux, 2010) for the photolysis of ozone 29

Table 2-6: Operative conditions at different altitudes (U.S. Standard Atmosphere, 1976) 30

Table 2-7 : initial conditions in the tropospheric environment 31

Table 2-8: Initial concentrations in stratospheric environment 32

Table 3-1: parameters for the evaluation of the GWP of H_2 derived from both maximum and average value of OH. 52

Table 3-2: parameters for the evaluation of the GWP of H_2 derived from both maximum and average value of OH. 63

Table 3-3: parameters for the evaluation of the GWP of H_2 derived from both maximum and average value of OH. 74

Table 3-4: parameters for the evaluation of the GWP of H_2 derived from both maximum and average value of OH. 83

Table 3-5: parameters for the evaluation of the GWP of H_2 derived from both maximum and average value of OH in an atmosphere with 1.5 ppm of H_2. 87

Table 3-6: concentration and fraction of OH and HO_2 in troposphere and lower level of stratosphere. The Concentration and M are both in molecules/cm^3 93

Table 3-7: concentration and fraction of OH and HO_2 in middle and high levels of stratosphere. The Concentration and M are both in molecules/cm^3 93

Table 3-8: Reaction rates for OH formation and destruction involving H_2 at ground level and at 15 km altitude. The reaction rates are reported in [molecules/cm^3/s] 94

Table 3-9: Reaction rates for OH formation and destruction involving H_2 at 25 Km. The reaction rates are reported in [molecules/cm^3/s] 95

Table 3-10: Reaction rates for OH formation and destruction involving H_2 at 40 Km. The reaction rates are reported in [molecules/cm3/s] 95

List of symbols

Variable	Description	SI unit
α_{H2}	H_2 lifetime	yr
τ_{H2+OH}	Consumption of H_2 by OH	yr
τ_{H2soil}	Consumption of H_2 by the soil	yr
R	Radiative forcing scaling factor	$W/m^2/ppb$
a	Production rate of the species	$CH_4/yr/H_2$
α_R	Lifetime of species causing the radiative forcing	Yr
H	Time horizon considered	yr
C	Conversion facto	-
tp	Length of step emission	yr
A	Pre-exponential factor	-
E_{att}	Activation energy	Cal/mol
R	Gas constant	Cal/mol/K
$K0$	Low pressure limit constant	-
Ki	High pressure limit constant	-

Box Model Equations

F	Mass flow rate	g/s
w_i	Gas phase weight fraction	-
wi,s	Surface weight fraction	-
yi	Gas phase mole fraction	-
$y_{i,s}$	Surface mole fraction	-

th_{ji}	Adsorbed specie i on j type site	-
V_r	Reactor volume	cm^3
x	Dimensionless coordinates	-
S_{dep}	Deposition surface area	cm^2
Ω	Reactor free cross section	cm^2
W	Susceptor width	Cm
P	External cools perimeter	Cm
L	Overall reactor length	Cm
T_g, P	Reactor Temperature and Pressure	K, atm
T_s	Suspected temperature	K
T_c	External fluid temperature	L
S_v	Deposition surface	cm^{-1}
tg	Dimensionless gas temperature Tg/Tr	-
ts	Dimensionless substrate temperature Ts/Tr	-
tc	Dimensionless cooling fluid temperature Tc/Tr	-
τ	Average residence time (Ω*L*ϱ*Mt/F)	s
ρ	Gas phase molecular density (P/R/T)	Mol/cm3
Mi	Molecular weight	g/mol
Mt	Average molecular weight	g/mol
S_{ti}	Stanton number	-
K_{ci}	Mass transport coefficient	Cm/s
$B_{i,s}$	Surface Biot number	-
$B_{i,e}$	External Biot number	-

α_T	Thermal diffusion coefficient	-
h	Linear heat transfer coefficient	Cal/cm2/s/K
U	Overall heat transport coefficient	Cal/cm2/s/K
C_p	Mixture specific heat	Cal/g/K
NG_{ij}	Gas phase reaction's stochiometric coefficient	-
NS_{ij}	Surface reaction's stochiometric coefficient	-
RG_j	Gas phase jth reaction rate	Mol/cm3/s
RS_j	Surface jth reaction rate	Mol/cm2/s

SZA equations

Tj	Century in JCD	-
ε_{mean}	Mean obliquity elliptic	degrees
ε	Obliquity correction	degrees
M_j	Geometric mean anomaly of the sun	degrees
C_j	Centre of the sun	-
$L_{o,j}$	Mean geometric longitude of the sun	degrees
L_j	Sun true longitude	degrees
$L_{a,j}$	Sun apparent longitude	degrees
e_j	Eccentricity of earth's orbit	-
Δ_{tey}	Equation of time	Minutes
S_{time}	True solar time	Minutes
$Sun_{decline}$	Sun decline	-

Acknowledgments

In questa ultima pagina vorrei ringraziare chi mi è stato accanto durante il completamento di questa tesi e di tutto il mio percorso universitario. Ringrazio la mia famiglia, che ha saputo darmi un supporto costante anche nei momenti di maggiore difficoltà. Ringrazio i miei più cari amici, che sono stati fonte di inesauribile stimolo culturale e intellettuale; sostentamento della mia curiosità in ambito scientifico e artistico.

Una menzione speciale è dovuta anche a chi mi ha guidato più direttamente in questo e percorso di tesi: a Matteo, che mi ha assistito durante tutto il lungo svolgimento della tesi; e al professor Cavallotti, che ha saputo guidarmi tra i miei dubbi e mostrami un primo accenno del mondo della ricerca universitaria.
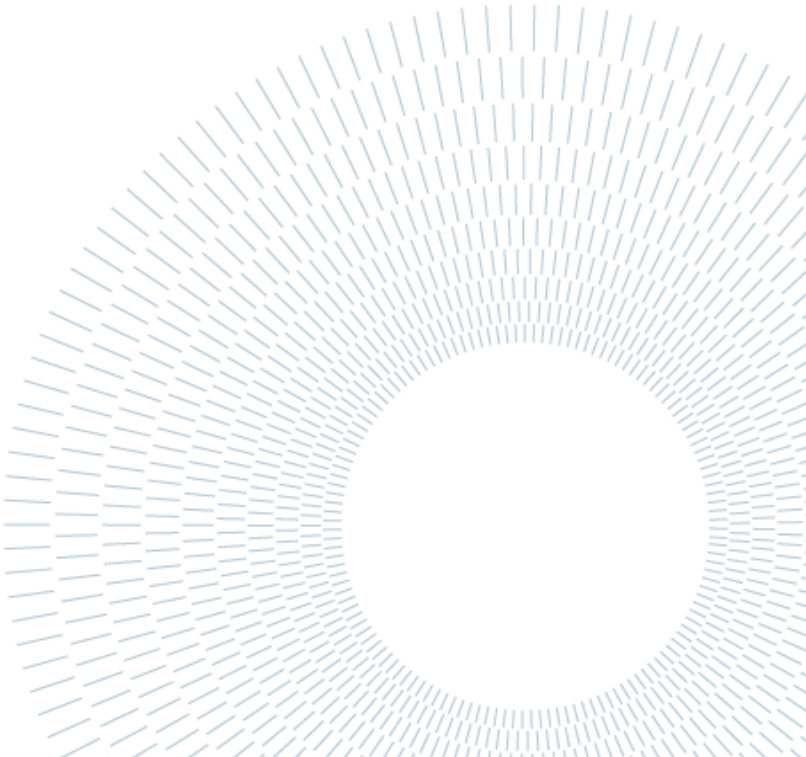
A tutte queste persone io rivolgo i miei più sentiti ringraziamenti.